ENERGETIC PROTONS IN THE MAGNETOSPHERE OF NEPTUNE

Thesis by

Mark Dixon Looper

In Partial Fulfillment of the Requirements
for the Degree of
Doctor of Philosophy

California Institute of Technology
Pasadena, California

1993

(Submitted January 8, 1993)

Dedication

qeSwI’wI’vaD paqvam vInob

qabtaHvIS tawIj mulajpu’ ’ej not SerwIj yapbe’mo’ mulajHa’pu’

lajvammo’ batlhwIJvaD mughajrupqa’moHpu’

not nobvam vIDIllaH

Acknowledgements

Not many professors can offer a grad student a berth as a 'midshipman aboard the *Santa Maria*; my adviser, Prof. Edward Stone, did just that by giving me a place in the Voyager mission, where I could participate in the exploration of new worlds (literally!). One customary phrase in thanking someone for help with a paper is to express gratitude for "many fruitful technical discussions"; this would be an incomplete statement here, as what I have learned from him about ways of assembling, organizing, and presenting information will prove valuable to me in many endeavors outside my profession, as well as in science. He has also been a lot more patient with the pace of my progress toward this thesis than I'd have had any right to ask!

Many people at the Space Radiation Laboratory have lent their knowledge, skills, and encouragement to me at various times during my association with the group. High on the list is Dr. Richard Selesnick; his invaluable contributions to my technical knowledge are reflected not only in the number of times his name appears in the reference list of this thesis, but also in the fact that he put me on the trail of a lot of the other references. And, of course, without his day-to-day advice, suggestions, and critiques, my penchant for stubbornly pursuing approaches that refuse to work would have kept me a grad student until the Voyagers crossed the heliopause! I hope, if a grad student is ever in a position to benefit from my advice, I will prove half as helpful to him as Richard has to me.

Dr. Alan Cummings and Dr. Tom Garrard have both allowed me to draw on their knowledge of space physics and experience with spacecraft instrumentation, gained through their long associations with the Space Radiation Laboratory and the Voyager Cosmic Ray Subsystem in particular. It really helps one understand the uses and capabilities of a piece of equipment when people who built and tested it are there to answer questions. In addition, Alan in particular has been a sounding-board for my results at the Voyager group meetings, and Tom allowed me to "jump ship" to Galileo on several occasions; it is said that you never really understand your own language until you study a different one, and what I learned about anomalous cosmic rays from Alan's discussion of his own work in the group meetings and about the design and calibration of the Galileo Heavy Ion Counter from Tom's "borrowing" of me have both given me a better perspective on my own particular project. And I can't think of one of the other members of SRL, including graduate students past and present, who hasn't helped me on several occasions, usually with the black boxes that computers still largely are to me. On that subject, I most often tapped my erstwhile officemates Chris Starr, Biff Heindl, Dr. Stinson Gibner, and Dr. David Palmer; everything I have produced, electronic or hardcopy, made use of their instruction.

I compared the Voyager project above to a seagoing voyage of discovery; like a ship, the Voyager mission has a crew who do everything from navigating to caulking the seams ("leaks" sprung and patched on Voyager 2 have included an arthritic scan platform and a tone-deaf radio receiver). They are all owed a debt of gratitude for making possible the "Grand Tour" of the giant planets, an expedition of unprecedented scope and range undertaken "in peace for all mankind"; and I certainly thank them for making possible my small part in it.

Finally, I would not have been able to work on this project without financial support from the California Institute of Technology and from the Jet Propulsion Laboratory under work order 60407 (NAS7-918). And I would not have turned my eyes to the skies at all without the backing in all forms that my parents have given me; I thank them for introducing me to the excitement of discovery in the first place, and for financial support when I've needed it and emotional support always. Oh yeah, and for the big Chevy too!

Abstract

The Cosmic Ray Subsystem aboard Voyager 2 measured large fluxes of trapped energetic protons and electrons in the inner magnetosphere of Neptune during the 1989 flyby; the protons above 1.9 MeV observed by the Low Energy Telescopes are analyzed in this thesis. Proton events are extracted from pulse-height distributions dominated by low-energy electron pileup noise, and fluxes are calculated with corrections for discriminator deadtime. Theoretical models for satellite absorption of charged particles are adapted to the large gyroradii of energetic protons, and model magnetospheres are constructed that involve diffusion of particles in the presence of this absorption; parameters of these model magnetospheres are adjusted to reproduce the observations. The inward-diffusing proton flux is limited by absorption due to the moon 1989N1 (Proteus), with absorption at high magnetic latitudes (whence high Ls) proving to be most important. The proton radial diffusion coefficient is an order of magnitude less than that inferred elsewhere for the electrons; this prevents protons from diffusing inward past 1989N1 before they are absorbed, and in fact the proton flux returns to background levels within a limit well outside the minimum L-shell of 1989N1, while electrons can diffuse past this satellite so that their flux recovers before they are absorbed by the other moons and rings closer to the planet. The rate of proton radial diffusion, in comparison with that for electrons, is consistent with the diffusion being driven by electric fields from wind fluctuations in the ionosphere of Neptune. Radial diffusion alone, however, produces too much pitch-angle anisotropy as particles with mild anisotropy in the outer magnetosphere are transported inward, and pitch-angle diffusion must be invoked to reduce the excess anisotropy and reproduce the observations. The pitch-angle distributions at different Ls are consistent with the diffusion coefficient for this process being comparable in magnitude to that for radial diffusion inside L of about 6.8, though still much less than the strong-diffusion limit, and negligible outside that L.

Table Of Contents

Chapter 1
Introduction

1.1. Planetary Magnetic Fields

The eight planets that have so far been observed at close range by spacecraft fall into two major groups, separated by the asteroid belt, when classified by a number of measures. Size and composition are the most obvious; in addition, we can draw several general distinctions between the magnetic fields of the terrestrial (inner) planets and the giant (outer) planets. As shown in table 1.1 below, of the four terrestrial planets only Earth has a substantial magnetic field, while all four giant planets possess huge magnetospheres, within which

Table 1.1 Planetary Magnetic Fields

(mostly after Lanzerotti and Krimigis (1985))

Planet	R_P (10^3 km)	k_0 (Gauss $\times R_P^3$)	angle between $\mathbf{k}_0$ and $\mathbf{\Omega}_P$	typ. magnetopause distance (R_P)
Mercury	2.42	$\approx 3 \times 10^{-4}$	$\approx 10^\circ$	1.1
Venus	6.10	$< 3 \times 10^{-4}$	--	1.1
Earth	6.37	0.31	11.5°	10
Mars	3.38	6.5×10^{-4} (?)	(?)	(?)
Jupiter	71.4	4.1	9.6°	60-100
Saturn	60.4	0.4	$< 1^\circ$	20-25
Uranus	25.6	0.23	60°	18
Neptune	24.8	0.13	45°	26

their magnetic fields largely shrug aside the solar wind. (Uranus data are from Ness *et al.* (1986), and Neptune data from Ness *et al.* (1989) and Ness (1990).) R_P is the planet's radius, $\mathbf{k}_0$ is the magnetic dipole moment, and $\mathbf{\Omega}_P$ is the planetary rotation vector; the sunward magnetopause distance varies with solar wind strength, but its typical size is a measure of the size of the planet's magnetosphere (in the case of Venus, the distance quoted is to the subsolar ionopause, as the solar wind interacts directly with the planet's ionosphere). Present and upcoming spacecraft visits to the giant planets are listed in table 1.2; Galileo will enter into orbit about Jupiter and drop a probe into its atmosphere, where all previous spacecraft have conducted flybys. This thesis makes use of observations from the 1989 Voyager 2 Neptune encounter.

Table 1.2 Exploration of the Outer Planets

Spacecraft	Planet	Launch	Arrival
Pioneer 10	Jupiter	2 Mar 72	3 Dec 73
Pioneer 11	Jupiter Saturn	5 Apr 73	2 Dec 74 1 Sep 79
Voyager 1	Jupiter Saturn	5 Sep 77	5 Mar 79 12 Nov 80
Voyager 2	Jupiter Saturn Uranus Neptune	20 Aug 77	9 Jul 79 26 Aug 81 24 Jan 86 25 Aug 89
Ulysses	Jupiter	6 Oct 90	8 Feb 92
Galileo	Jupiter	18 Oct 89	7 Dec 95

1.2. Satellites in the Magnetospheres of the Outer Planets

1.2.1. Moons as Charged Particle Sources

Besides their sheer size, the magnetospheres of the giant planets differ from that of Earth in that each of the four outer planets has rings and several satellites that orbit well within their magnetospheres; Earth's moon is sufficiently distant that it enters the magnetotail (the extension of the magnetosphere swept "downstream" by the solar wind) only briefly each month. These satellites have a large impact on the charged-particle populations of the magnetospheres, as both sources and sinks. Plasma in Earth's magnetosphere can come from the ionosphere or from the solar wind, and energetic particles can be generated from the plasma by various acceleration processes or injected directly through decay of neutrons spalled from the atmosphere by cosmic rays (CRAND, for Cosmic Ray Albedo Neutron Decay, protons from interactions with ring material were also observed by Pioneer 11 and Voyager 2 at Saturn (Schardt and McDonald 1983)); at the outer planets, where satellites are present within the magnetosphere, they can also become a source of charged particles (or of neutral atoms which can then become ionized by interaction with sunlight or with charged particles already present).

The moons Titan at Saturn and Triton at Neptune have atmospheres, in the case of Titan denser than Earth's at the surface. Neutral hydrogen from dissociation of methane in Titan's atmosphere maintains a hydrogen torus about the moon's orbit, which in turn supplies plasma to the magnetosphere (Broadfoot *et al.* 1981; Sandel *et al.* 1982), whence energetic protons can be accelerated (Vogt *et al.* 1981); Titan may also be a source of low-energy nitrogen ions (Bridge *et al.* 1981). Triton's atmosphere also puts hydrogen and nitrogen plasma into Neptune's magnetosphere (Richardson *et al.* 1991); nitrogen from this moon was also observed at higher energies (Mauk *et al.* 1991). Solid moons can also contribute plasma to their planets' magnetospheres; oxygen sputtered from the icy inner moons and rings of Saturn by energetic particles has been observed (Armstrong *et al.* 1983). The most dramatic case of a moon contributing matter to the magnetosphere, however, is that of the volcanic moon Io at Jupiter, which is the source of a plasma torus of sulfur, oxygen, and sodium (Broadfoot *et al.* 1979; Bridge *et al.* 1979); these ions are also observed at energies up to several MeV per nucleon (Krimigis *et al.* 1979; Vogt *et al.* 1979).

1.2.2. Moons as Charged Particle Sinks

Charged particles can depart a magnetosphere by striking the planet's atmosphere (or surface, in the case of Mercury) or by escaping to interplanetary space. In the case of the outer planets, where there are satellites and rings within the magnetosphere, these can also absorb particles. Because the position and size of such solid matter can (usually) be determined better than, *e.g.*, those of a plasma torus, the rate and distribution of charged particle losses to satellites and rings can be calculated more precisely; observations of the particle population in the magnetosphere can then be compared with models that incorporate satellite sweeping along with other aspects of magnetospheric dynamics in order to draw conclusions about those other aspects. For example, the location of a satellite "signature," a reduction of charged particle flux due to sweeping, can give new information about the shape of the magnetic field when it is noted that the position along the spacecraft's trajectory where the signature is observed (which position must be on a field line accessible to particles which have encountered and been depleted by the moon) differs from the location predicted from a model of the planetary magnetic field (Vogt *et al.* 1981; Selesnick 1992a). This process can be reversed: if an absorption signature is observed that cannot be accounted for by known satellite material, it can indicate the presence of unseen rings or moons (Simpson *et al.* 1980; Van Allen *et al.* 1980; Fillius *et al.* 1980; Chenette and Stone 1983; Cuzzi and Burns 1988).

Since moons and rings deplete the charged particle population in their vicinity, particles observed near them must be replenished by a local source, by diffusion from other parts of the magnetosphere, or by both. Given a calculation of the loss rate due to satellite sweeping, the replenishment rate from models of sources and diffusion can be compared with observations; this can be done on the basis of a single recent encounter of the moon with the particles being observed, yielding a "microsignature," or in a time-average over many encounters, resulting in a "macrosignature." This thesis presents analysis of the macrosignature in the few-MeV proton population due to the small inner moons and satellites of Neptune, in particular 1989N1 (Proteus). The magnetic fields of Uranus and Neptune, if approximated by a dipole field as in table 1.1, are substantially different from those of the other magnetized planets in that the tilt of the dipole moment relative to the rotation axis is much greater; in addition, the dipole centers are offset from the centers of the planets by .31 Uranus radii (Ness *et al.* 1986) and .55 Neptune radii (Ness *et al.* 1989; Ness 1990) respectively. These large tilts and offsets in the approximate dipole models are indicative of the complexity of the real fields, with higher-order magnetic moments making a large contribution to the field; in terms of the interaction of satellites with charged particles in the magnetosphere, the large tilt indicates that particles will be swept from populations that will be observed at distances from the planet much greater than that of the sweeping material, as will be shown in chapter 4, so that the macrosignature can be expected to be broad and it should be possible to probe diffusion with some sensitivity well away from the absorbing satellite. Indeed, as will be seen, the proton macrosignature is so broad that the flux of protons in the energy range studied drops below detectability well outside the region where the magnetic field lines intersect the moon's orbit near the magnetic equator, which is the only place where absorption occurs at all in a dipolar field concentric with the planet and aligned with its rotation axis. Diffusion can widen the macrosignature about this region in the simple field, but the tilt of the magnetic field of Neptune, combined with other effects peculiar to energetic ions with their large gyroradii, results in an extreme case where the rate of absorption away from this region can be larger than the rate of absorption in it. Thus the energetic proton population at Neptune is subject to effects absent at Jupiter and Saturn as well as at Earth (they are present at Uranus, but the higher proton fluxes there obscure them somewhat), and so we have another instance to contrast with previous experience, which is of course the whole point of comparative planetology and a large part of the reason for space exploration in general and the Voyager mission in particular.

Chapter 2

Instrumentation and Event Analysis

2.1. Instrument Description

2.1.1. The Cosmic Ray Subsystem

An overview of the Voyager Cosmic Ray Subsystem (CRS) appears in figure 2.1; the CRS is mounted near the root of the Science Boom (about 13 inches, or the approximate width of the CRS itself, from the lip of the High Gain Antenna, with the top of the electronics box about even with the lip) on each of the two Voyager spacecraft. HET 1 is on the side of the CRS closest to the antenna dish and HET 2 on the side farthest from it. Each Voyager's CRS consists of seven silicon solid-state particle telescopes: The Electron Telescope (TET) consisting of eight 3mm lithium-drifted detectors and six tungsten absorbers, optimized to measure electrons from approximately 5 to 110 MeV in interplanetary space, though special calibrations have been done to extend measuring capability below 1 MeV in a planetary magnetosphere (Selesnick & Stone 1991a); two double-ended High Energy Telescopes (HETs) consisting of two surface-barrier and nine lithium-drifted detectors of varying configurations, with some sensitivity to 3 to 10 MeV electrons but mostly observing ions from hydrogen to beyond iron from about 4 to 500 MeV/nucleon, using two gain modes; and four Low Energy Telescopes (LETs), described below. Some 101 single-detector and detector-coincidence rates are accumulated and read out; two parallel redundant blocks of six buffers (two event types for a pair of LETs, three for one HET, and one for TET, per block) accumulate pulse-height-analyzed particle events, with serial polling so that rare events in some buffers will not be overwhelmed by more common events in others. Details about the CRS are given by Stone *et al.* (1977) and Stilwell *et al.* (1979).

2.1.2. The Low Energy Telescopes

2.1.2.1. Shielding and Geometry

The LETs observe low-energy ions; for protons, the sensitivity is from approximately 1.9 to 8.4 MeV for particles depositing energy in at least the first two detectors, with protons down to approximately 500 keV able to trigger the first detector's discriminator (and increment its rate counter). A single LET is shown in figure 2.2; the diagram shows a typical longitudinal cross section, including most of the material that acts as shielding for the detectors. There are four silicon surface-barrier detectors in each LET; nominally, L1 and L2 are 35μm thick, and L3 and L4 are 450μm thick. The first three detectors are pulse-height analyzed, while L4 is normally used as an anticoincidence element to ensure that a particle entering through the front of the telescope actually stopped in the pulse-height-analyzed stack, and therefore that all of its energy has been measured and accounted for.

The minimum shielding around most of the LET is .020 inches (508μm) of aluminum, with a stopping power of several MeV for normally-incident protons (see, *e.g.*, Dearnaley & Northrop (1966)). The collimator at the front of the LET is made of Delrin with a minimum thickness of .020 inches (508μm), but particles passing through this thin section to strike the detectors would have to travel at an oblique angle and thus traverse a much longer distance in the Delrin, so stopping power is even greater. Thus for protons up to several MeV, it can be assumed that only those that enter through the 3μm aluminum window (stopping power $\approx$300 keV for normally-incident protons) attached to the collimator will be observed. This defines a geometry factor of $G \approx 4.5\ \mathrm{cm}^2\,\mathrm{sr}$ for particles striking the active area of L1; for particles that trigger both L1 and L2, and that are thus constrained to pass through the active areas of both, the geometry factor is $G \approx 0.44\ \mathrm{cm}^2\,\mathrm{sr}$ (see, *e.g.*, Sullivan (1971)). Particles that trigger L1, L2, and L3 will have the same geometry factor, as the 25° acceptance cone defined by the active areas of L1 and L2 imposes a tighter constraint than that imposed by the additional requirement that the particle pass through the active area of L3.

The CRS is covered by a multilayer blanket for thermal and micrometeoroid protection. The penetrating nature of electrons allows the TET to look out through this unimpeded;

Figure 2.1

The Voyager Cosmic Ray Subsystem (CRS) prototype (after Stilwell *et al.* (1979)); flight units on both Voyagers are similar, except for HET 2 pointing directions (Voyager 1's resembles this, Voyager 2 has HET 2 B-end pointing more to the left). The High Gain Antenna would be to the right, aimed upward, in this view of a mounted flight unit, and the Scan Platform would be to the left.

Figure 2.1

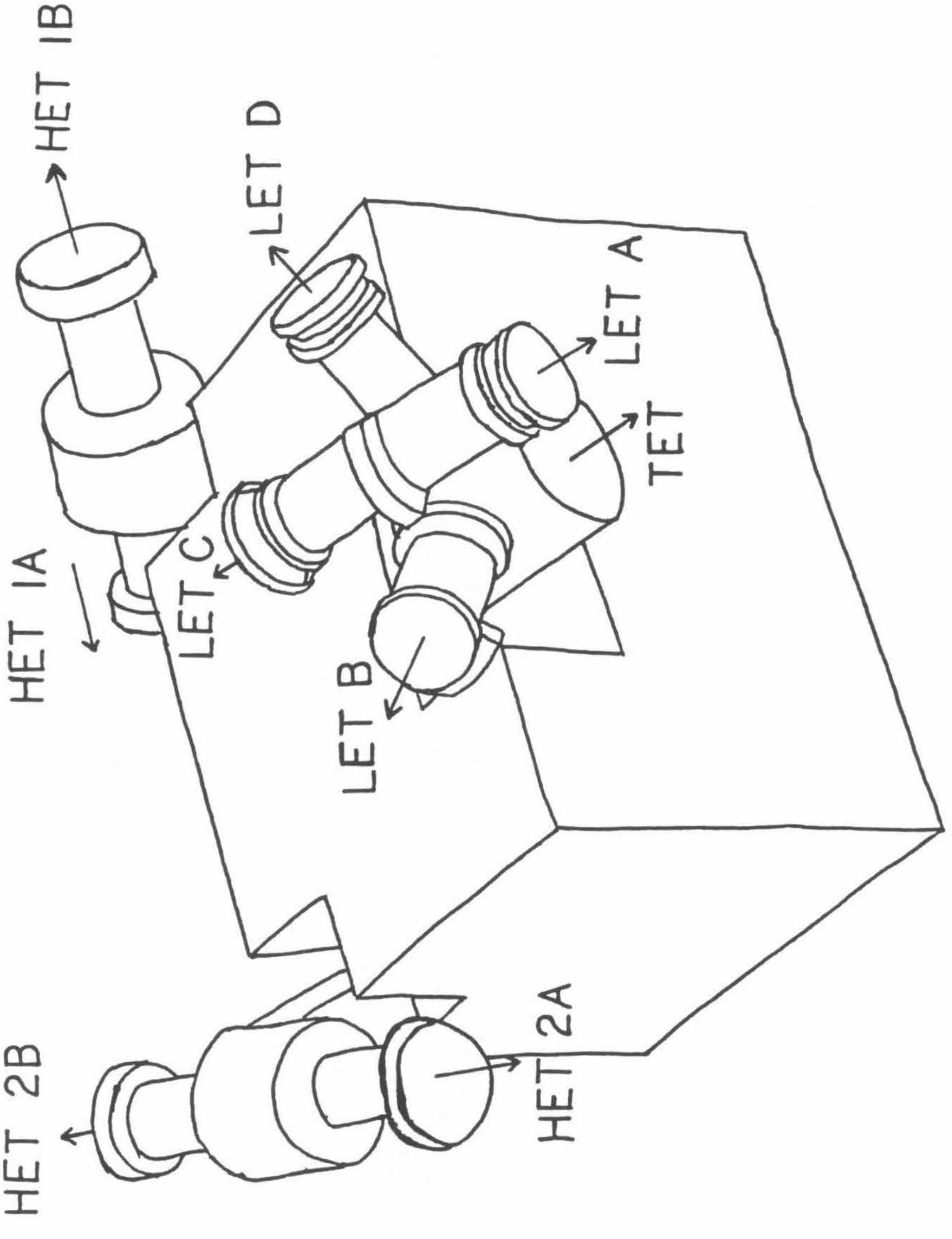

Figure 2.2

Typical longitudinal section of a CRS Low Energy Telescope (LET), showing detectors and bulk construction (electrical contacts, washers, shims, *etc.* are not shown). Detector active areas are indicated by heavy lines.

Figure 2.2

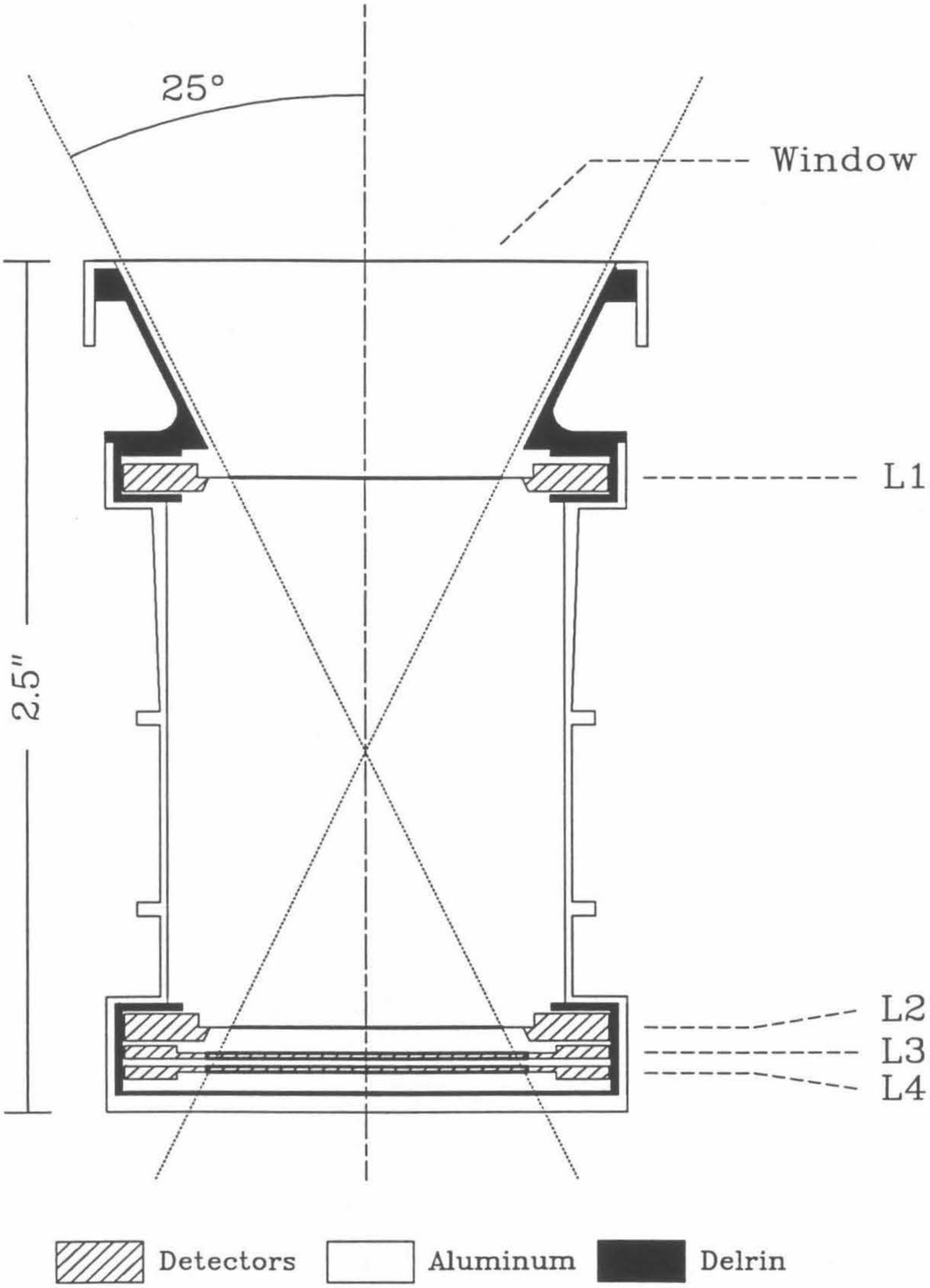

windows consisting of fewer layers are provided for each end of each HET, and the fronts of the LETs are outside the blanket altogether, so that only the 3μm (nominal) aluminum window shields the L1 detector in each LET.

2.1.2.2. Coincidence Logic and Operating Modes

The LET PHA's are triggered by detector coincidence states called LZ3 or LZ3*; the former is for ions heavier than helium, the latter for hydrogen and helium. The normal operating mode is for the LZ3 or LZ3* trigger to be tripped when L1, L2, and L3 are triggered and L4 is *not*. Nominal thresholds of the discriminators are 200 keV for L1 and L2, 1 MeV for L3, and 300 keV for L4. The status of the other detector discriminator levels is checked about 4 μsec after the L1 discriminator fires (Gehrels 1981), as is that of a discriminator fed a linear combination of signals in L1, L2, and L3, called the "slant" discriminator or SL ($SL = L1 + 0.42\,L2 + 0.20\,L3$, with a threshold of 9.6 MeV), which is used to identify particles heavier than helium ($Z \geq 3$). If L1, L2, and L3 discriminators have been triggered and L4 and SL have not, then the LZ3* rate counter is incremented and PHA "gates" are opened to measure the energy loss signal in L1, L2, and L3; if the above conditions are met except that SL *is* triggered, LZ3 is incremented and PHA gates again open. The coincidence logic is alterable by remote command to delete L2 and/or L3 terms from the PHA analysis conditions; thus pulse-height analysis (of all three detectors) can be triggered by L1 alone ("singles" mode) or by L1 and L2 only ("doubles" mode), in addition to the normal ("triples") mode. These are minimal triggering conditions, so an event triggering L1, L2, and L3 would be analyzed in all three modes, and an event triggering only L1 and L2 would be analyzed in singles as well as in doubles mode.

During the Uranus and Neptune encounters, the CRS basic time unit was 96 seconds long. A 4-bit subcommutator (in addition to the gain bits for the HETs) determines which of the 101 CRS rates is counted in and read out from each of the 29 accumulators; the basic unit of time resolution is the period it takes this to step through its 16 states. Also in this period, 400 pulse-height-analyzed events are read out from the PHA buffers (a "null" event is read out if all buffers in both blocks are empty when polled). The command system of the Voyager 2 spacecraft was set to instruct the CRS to change operating states every two subcomm cycles; of the four LETs, the mode changes affected only C and D, switching them (together) from doubles to triples mode and back. The ground data-processing time unit, the "volume", was set equal to one subcomm cycle for the Uranus and Neptune encounters; hereinafter the two terms "volume" and "subcommutator cycle" will be considered equivalent. The L1 detector of Voyager 2's LET B ("LB1," and similarly, hereinafter) was damaged by the high radiation dose absorbed during the spacecraft's 1979 flyby of Jupiter, and has become noisy; thus its preamplifier has been turned off permanently so it cannot generate false PHA triggers to use up the buffer space it shares with LET A, which was left in singles mode throughout these encounters. Because of the possibility of spurious coincidences in the high-count-rate environment of a planetary magnetosphere, LA4, LC4, and LD4 were turned off, so that real events would not be suppressed due to the L4 anticoincidence term in the LET analysis trigger equations; LB4 was left on. Thus the LET data from these encounters consists of continuous LET A singles, and LET C and D doubles and triples data alternating along a 15-step chain (each step is two volumes):

323232323232323 323232323232323 323232323232323 *etc.*

Note the adjacent triples modes occurring every 30 volumes (48 minutes).

2.2. Particle Identification

2.2.1. Energy

The information returned to Earth by the CRS consists of logarithmically-compressed rate counts (number of times during the accumulation period (one or more subcomm states) that a given detector or combination of detectors was triggered) and PHA event information (tags to identify which telescope the data was from and in some cases other information, and channel numbers from each PHA). The Space Radiation Laboratory receives this data, stripped out from the downlinked stream from the whole spacecraft, from the Deep Space Network and the Jet Propulsion Laboratory via Goddard Space Flight Center on an "encyclopedia tape" that also includes information on time intervals: for instance, if downlink noise obscures some of the PHA events in a 96-second volume, the amount of time that the data in that volume was intelligible is noted. For the LETs, nominal PHA channel widths are 75 keV for L1 and L2, and 500 keV for L3. The large width of the channels in L3 (resulting from the large energy range, 2.048 GeV full-scale, necessary to measure the ≈1.5 GeV that could be deposited in this thicker detector by an iron nucleus) limits the number of "bins" into which a proton spectrum can be divided, since a maximum of 7 to 8 MeV (depending on angle of incidence) will be deposited in L3. The procedure for dividing up particle events into energy spectra in this work largely followed that used at Uranus, with existing programs modified as described below.

Actual thicknesses of the LET detectors were measured before final assembly. Actual thresholds and PHA channel widths and offsets were also measured using an electronic pulser before launch, but these were correct only relative to an input capacitance (which converts deposited charge, proportional to energy loss in the detector, to a voltage signal); these normalizations were determined in flight by calculating energy deposits in each detector for particles of different energies and incidence angles, and adjusting these parameters to obtain the best match of theoretical energy deposits with the PHA channels observed for solar flare particles (Cook 1981). Flight calibrations were also done to determine the thickness of the dead layer burned into the front of each LET's L1 detector by the large dose of radiation absorbed during the Jupiter flyby. With this information, we can calculate from the PHA channel numbers the energy deposited in each detector, and we can then compare each pulse-height-analyzed event with the energy deposits expected for different ions at different energies to identify particle species and energy. The full Voyager cruise analysis programs employ a generalized six-parameter range-energy relation fitted to flight data by Cook (1981) to calculate an estimate of the ion nuclear charge Z from the energy deposited in the L1 and L2 (or L2+L3) detectors, and in the case of a triples event another estimate of Z from the energy deposited in L2 and L3. The two Z estimates for a triples event can be compared for consistency, and all Z estimates can be required to be within some small distance of a single whole number, in order for an event to be accepted. Application of this procedure to Neptune LET data resulted in perhaps two or three credible nitrogen and oxygen, and a few more helium, events; essentially all the nuclei the LETs observed were hydrogen. Since the

Figure 2.3

LET C doubles events observed in the inner magnetosphere of Neptune (from hour 20 of day 236 to hour 13 of day 237): crossplot of energy deposited in detectors LC1 and LC2 for particles not triggering LC3, as converted from PHA channel data with a uniformly-distributed random number between zero and one added to the channel number before energy calibration was applied. Solid tracks represent theoretical energy deposits for protons of different energies incident along the LET axis (lower curve) and at 25° to this axis (upper curve). Pairs of points on the two curves (connected and labeled) are for protons of the same energy when incident on the LET's window: (A) 1.9 MeV, (B) 2.1 MeV, (C) 2.4 MeV, and (D) 2.9 MeV. Tracks end at the point where protons would deposit 1 MeV in LC3, thus triggering it and being logged as triples events. A plot for LET D would look similar, but would have more events.

Figure 2.4

Crossplots of LET C triples events observed over the same time period as in figure 2.3, for (a) LC1 *vs.* LC3 and (b) LC2 *vs.* LC3. A random number is added to the PHA channel number as for doubles events, and the two solid curves are for the same incidence angles as in that figure. Labeled pairs of points are for incident energies of (A) 3.2 MeV, (B) 3.7 MeV, (C) 4.3 MeV, and (D) 5.0 MeV. A plot for LET D would look similar, but would have more events.

Figure 2.3

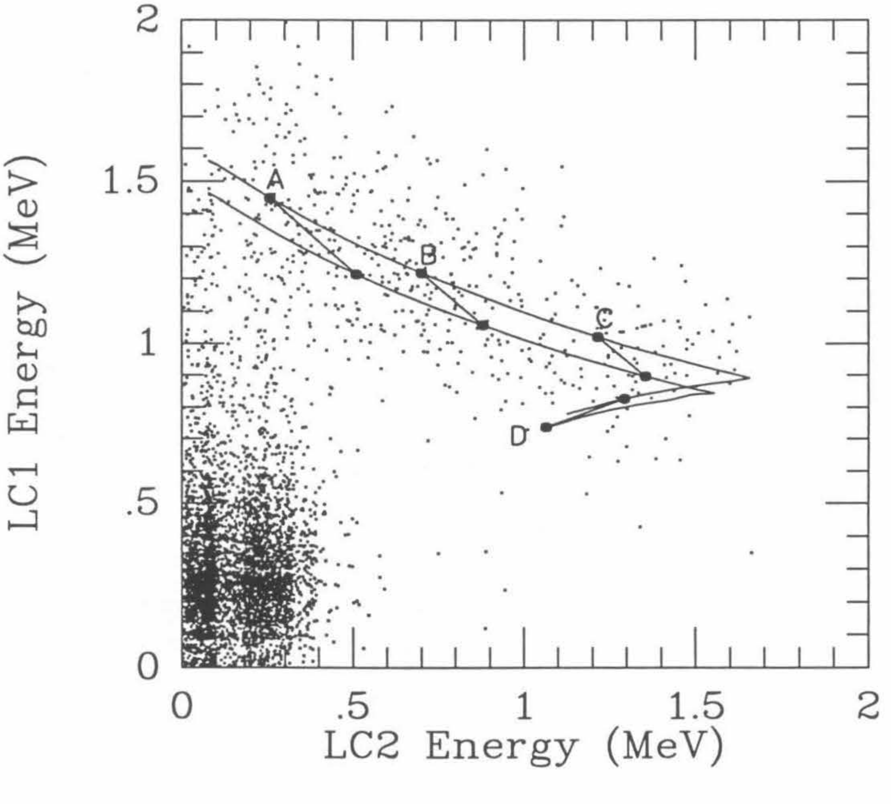

Figure 2.4

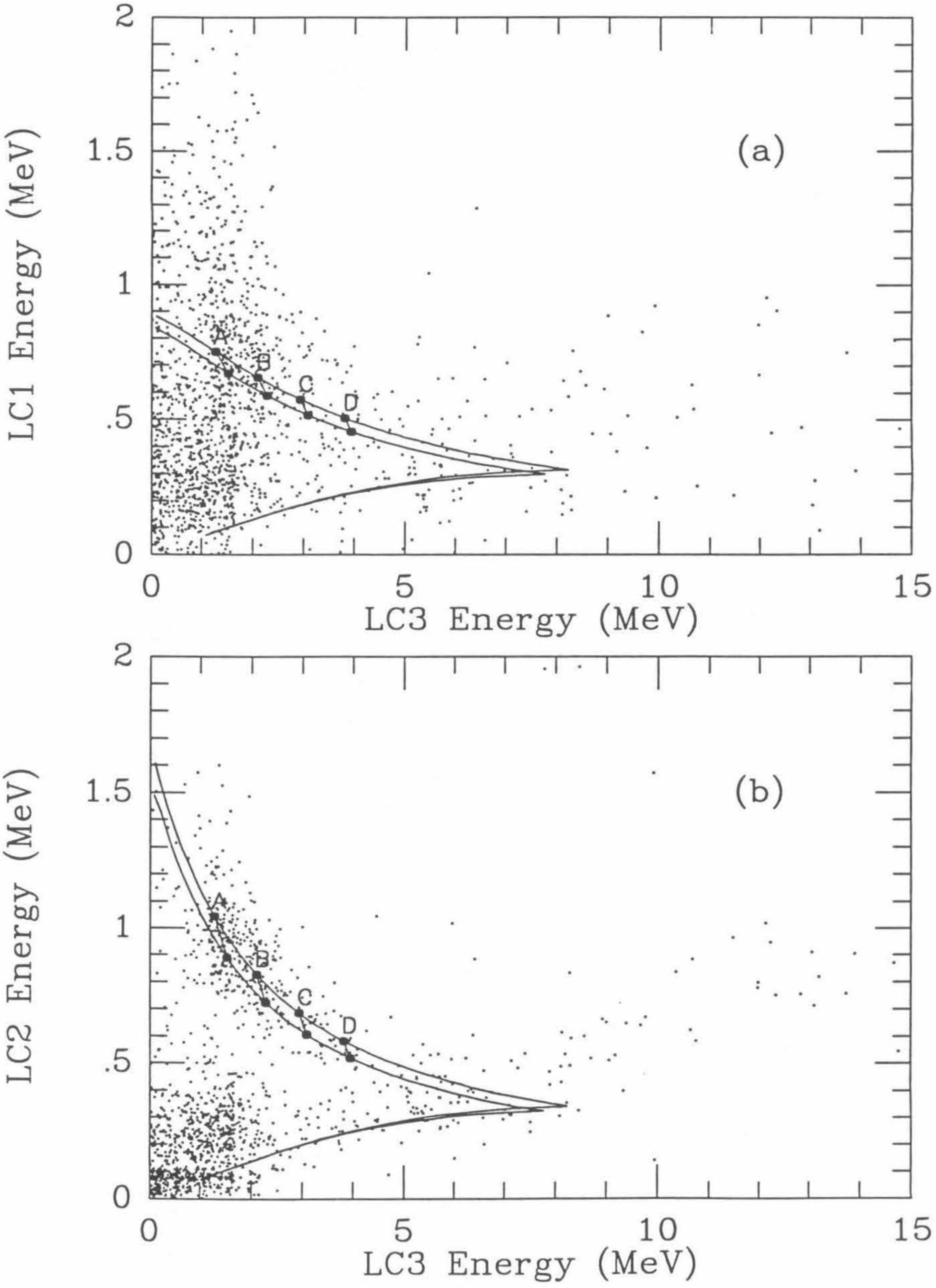
(a)
LC1 Energy (MeV)
LC3 Energy (MeV)
2
1.5
1
.5
0
0
5
10
15
A
B
C
D
(b)
LC2 Energy (MeV)
LC3 Energy (MeV)
2
1.5
1
.5
0
0
5
10
15
A
B
C
D

hydrogen and helium tracks calculated on a crossplot of energy deposits in two detectors are widely separated, even by comparison with the broadened observed proton track width shown hereinafter, we can just look at protons henceforth.

Figures 2.3 and 2.4 show the problem before us in identifying and sorting protons by energy: the data set is extremely noisy. The solid lines in these figures are nominal tracks calculated for protons incident normally and with maximum obliquity (25°) on the LET C front window, and in interplanetary space the observed proton energy deposits are not spread out much beyond this nominal band. However, in the high-count-rate environment of a planetary magnetosphere, particle incidence rates can overwhelm the operating timescales of an instrument optimized, as was the CRS, to measure rare events in interplanetary space. A clue to the nature of the smearing-out of the proton band is the dense patch of events at the lowest energies in each detector in each crossplot: if we ignore the events that lie near the nominal proton band, and are likely to be real protons, the remaining set of events is sharply peaked toward low energies (thresholds of detectors reduce, but do not eliminate, numbers of events recorded in the very lowest PHA channels). Moreover, many of these events involve energy deposit in L2 and L3 as well as L1, indicating that some of the causative particles are penetrating to these detectors, either through the detector(s) above or through the walls of the LET. These traits are consistent with the cause being a pileup of low-energy electrons: if, say, ten 20-keV electrons fall on the L1 detector within its ≈4 μsec shaping time, they will collectively look like a single pulse of up to 200 keV and can trigger the discriminator. Other possibilities considered include piled-up low-energy protons and the rare higher-energy electron that deposits all or most of its energy in one detector (an energetic electron will usually deposit very little energy in detectors as thin as L1 and L2, but electrons experience much more straggling in energy deposit than ions and also experience more deflection due to scattering, and a rare event could result in all the energy of, say, a 200-keV electron appearing in L1). However, simple models of pileup were applied, based on the low-energy electron and proton measurements from the Low Energy Charged Particle (LECP) experiment aboard Voyager 2 (Krimigis *et al.* 1989), and the results were compared to the CRS LAZ3* (shown in figure 2.8(b) later), LA1, LC1, and LD1 rates. Also, the detection efficiencies for electrons (with energies well above the most-probable energy deposit) of Lupton and Stone

(1972) were applied to the LECP observations of electrons in the vicinity of the L1 threshold energy, and the same comparison was made. Only the multiple pileup of low-energy (tens of keV) electrons could reproduce the count rates observed; the other two candidates were one to two orders of magnitude smaller.

If the L1 counting rates are dominated by electron pileup, then the pileup energy deposits will also be present when a real proton strikes the LET; due to the high rate of pileup events and the AC coupling of the preamplifiers to the measurement electronics, the baseline from which the PHA measures pulse heights will shift so that its value averaged over pileup events will be zero. Then the proton energy deposit will be measured relative to this average baseline, with fluctuations in the pileup resulting in deviations in reported energy deposit both above and below the real value. Thus the proton bands in figures 2.3 and 2.4 will be smeared out both above and below their nominal positions, as observed, even though the electron energy deposits are (of course) only positive. It is impossible to identify precisely the energy of a particular proton event, even in the absence of noise, because of the finite energy resolution of the PHA channels; in normal data processing (for observations in interplanetary space), a random number between zero and one is added to the (whole) number of each detector's PHA channel before energy calibration is applied, and then the set of proton events is divided up into energy bins in such a way that the input spectrum is not distorted, *i.e.*, if the finite energy resolution causes a proton from one bin to be erroneously assigned to another then on average a proton will also be misidentified in the other direction. In the noisy data set presented here, a different set of energy bin identifiers will need to be derived, and in order to test candidates it will be necessary to model the noise distribution.

Figures 2.5 show the PHA channel crossplots from LET A; these are approximately to the same energy scales as figures 2.3 and 2.4, but because of the vastly greater number of pulse-height-analyzed events in LET A compared to LET C (since all events triggering LET A's L1, not just those that also involve a triggering of L2 and/or L3, are candidates for analysis) the events are left in channels rather than being randomized and converted to energies as in those figures. Some trace of the proton tracks is evident in figures 2.5, but the vast majority of the events are low-energy noise that we have attributed to piled-up electrons, and the vast majority of *these* occur in channels 0 of LA2 and LA3. This is clearer in figures

2.6, wherein a spectrum of pulse heights in each LET A detector is plotted, summing over all pulse heights in the other two detectors. The falloff at the lowest channels of LA1 is due to the requirement that its discriminator be triggered, which is not required of LA2 or LA3 in singles mode. Even if we ignore the less-steep tail in higher channels of LA1, which may be attributable to real protons, it is clear that the LA1 noise distribution is much broader (measured in channels) than that in LA2 or LA3, and thus we assume that the dominant noise displacement of a proton event in any of the LETs is in the L1 energy. This is to be expected anyway if the main source of noise is piled-up electrons, as relatively few would penetrate L1 to reach L2 or L3 (and indeed, most of the events in figures 2.5 fall in channels 0 of LA2 and LA3, as noted above).

In interplanetary space, the proton band is not much broadened beyond the pair of nominal tracks shown, so we might split it into energy bins by cutting it along the labeled lines in figures 2.3 and 2.4, which are lines of constant incident proton energy at different incidence angles. In practice, it is assumed that energy losses in the window and the L1 dead layer are about the same for all incidence angles (relative to total proton energy), and therefore that the total energy deposited in the pulse-height-analyzed detectors plus this lost energy is the incident total energy. In effect, this assumes lines A, B, and C in figure 2.3 to be at 45°, which is not a bad approximation; the assumption that losses are the same over the acceptance cone is even better for triples events in figures 2.4, as the lost energy is a smaller fraction of the total energy. A correction needs to be applied to "foldback" events such as those at points D in figure 2.3, on the part of the track where L2 energy decreases with decreasing L1; these represent particles that penetrated L2 but did not deposit enough energy in L3 to trigger its discriminator and register as triples events. The foldback track in figures 2.4, representing particles that penetrate L3, would largely be eliminated by the L4 anticoincidence term in normal operations, as only about 300 keV would have to be left after penetration of L3 before L4 was triggered and the event was suppressed. At the Uranus and Neptune encounters LA4, LC4, and LD4 were turned off, so figure 2.4(b) in particular shows a strong foldback track; these tracks overlie one another for different elements, so it is not possible to differentiate protons from heavier species, and in fact the foldback (positive slope) part of the track extends to higher energies than protons can achieve, indicating the presence

Figure 2.5

Crossplots of LET A PHA events observed over the same time period as in figures 2.3 and 2.4, for (a) LA1 *vs.* LA2 and (b) LA1 *vs.* LA3. Scales approximately match in energy those of figures 2.3 and 2.4(a) respectively. Area of the circle at each point is proportional to the number of points in that pair of channels; channel pairs with more than 1000 events in them are plotted as open circles. The smallest points are a single PHA event in a channel pair, while there were 16,111 events in channel 7 of LA1 and channel 0 of LA3 over this time period.

Figure 2.6

Pulse-height distribution for each LET A detector, summed over all pulse-heights in the other two: (a) LA1, (b) LA2, and (c) LA3. Channel widths are approximately 75 keV for LA1 and LA2, 500 keV for LA3.

Figure 2.5

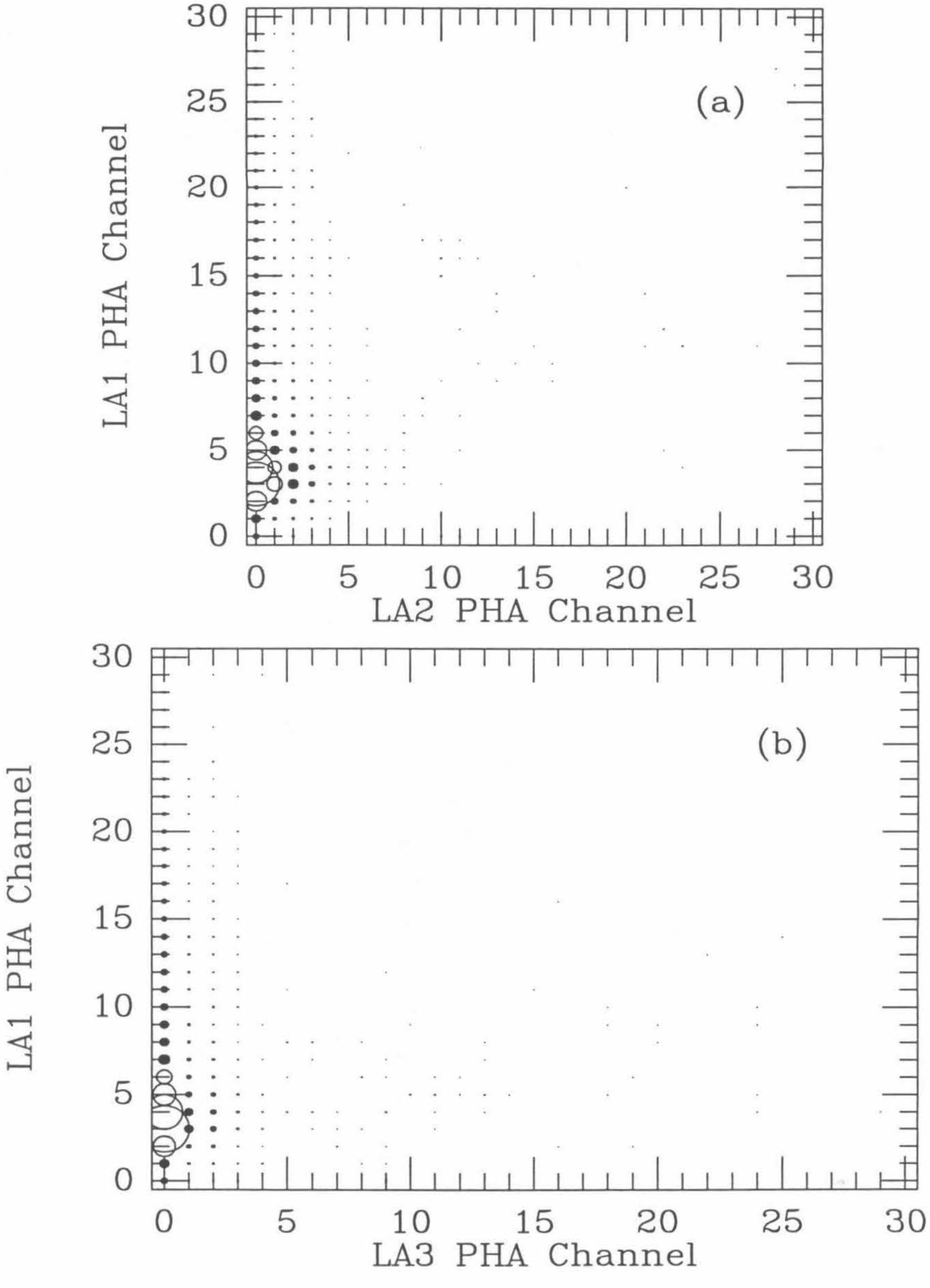
(a)
LA1 PHA Channel
LA2 PHA Channel
0
5
10
15
20
25
30
(b)
LA1 PHA Channel
LA3 PHA Channel

Figure 2.6

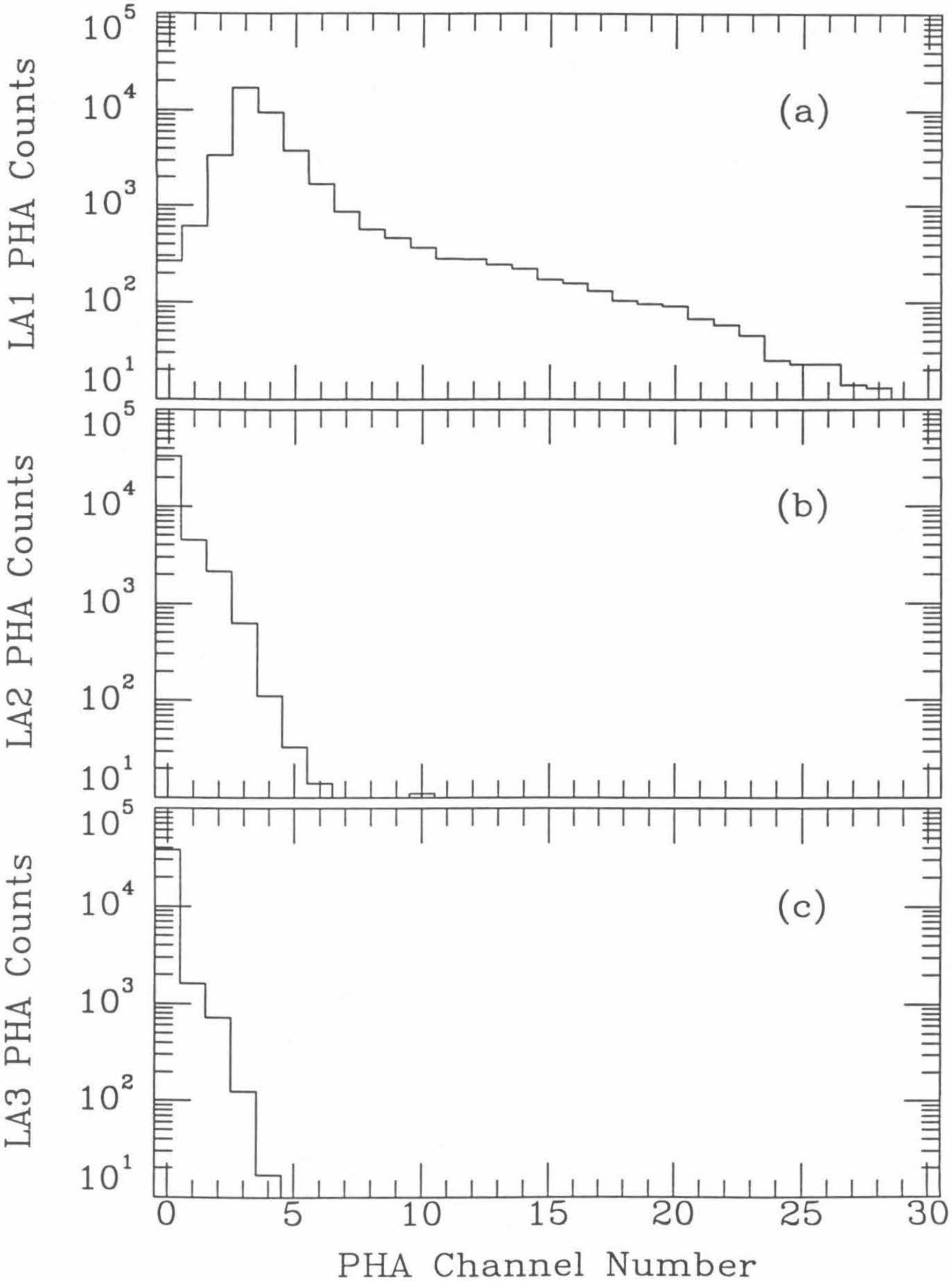
LA1 PHA Counts
LA2 PHA Counts
LA3 PHA Counts
10^1
10^2
10^3
10^4
10^5
(a)
(b)
(c)
0
5
10
15
20
25
30
PHA Channel Number

of these high-energy heavy cosmic ray nuclei.

This scheme for binning proton energies was tried on Monte Carlo data sets generated by assuming different incident energy spectra, generating events, and adding on varying amounts of Gaussian L1 noise (keeping the mean of the distribution at the "real" value of L1 energy for the event) and smaller amounts (about one energy channel width) of L2 and L3 noise before binning the particles. The dominant L1 noise systematically promoted low-energy events into higher-energy bins when the interplanetary energy-binning scheme was tried, distorting the flux-*vs.*-energy spectrum by up to several tens of percent. Other schemes were tried, and in the end it was found that the best way to reproduce an input spectrum for different energy slopes and amounts of noise was to ignore L1 energy altogether, once the identification of the event as part of the proton band had been made. For doubles events this meant making bin divisions based on the L2 energy calculated for some mean incidence angle (≈13°, the average for an isotropic incident proton distribution), and for triples it involved using L2 and L3 energies to calculate an expected L1 energy and reset the energy in L1 to this value before making the total energy cut. Energy bins were chosen from those used at Uranus, for more direct comparison with those observations (Stone *et al.* 1986). Because the width of the doubles track is such as to make the foldback portion indistinguishable from the direct part, all doubles protons with L2 energies higher than 2.1 MeV (points B in figure 2.3) were assigned to a single bin, so that we have two doubles bins: 1.9 to 2.1 MeV, and 2.1 to 2.9 MeV. Protons from 2.9 to 3.2 MeV, depending on incidence angle and thus energy deposit in L3, can register as doubles or triples events; an attempt to measure this energy bin with a reduced effective geometry factor was made at Uranus (Stone *et al.* 1986), but it is not included in this work. Triples protons were divided at Uranus into energy bins of roughly one or two L3 channel widths; the first three such bins are shown in figures 2.4, and these are all that will be used in this work, since beyond point D (5.0 MeV) the direct track runs into the foldback track in L2 *vs.* L3 (these two tracks and the low-energy noise are not readily separable anywhere in the L1 *vs.* L3 data set). Thus we have three triples bins to which we can assign protons: 3.2 to 3.7 MeV, 3.7 to 4.3 MeV, and 4.3 to 5.0 MeV. Programs to implement these cuts on the set of pulse-height-analyzed events were adapted from those used at Uranus; in addition, approximately a dozen events in the doubles data set and another dozen in the triples were removed by hand because they appeared to lie on or near the L4 foldback track but were accepted by the programs.

2.2.2. Fluxes

The methods discussed above allow us to construct a spectrum with the right shape, but some other information is needed to obtain the normalization, since the PHA polling system is not guaranteed to catch every proton passing through the telescope and satisfying the coincidence conditions (if the summed rates of *all* types of pulse-height-analyzed event exceed 400 per volume, then something will definitely be left out). The PHA triggering rates, LZ3*, should catch every such proton; however, these too will be less than the real rates of proton incidence because of discriminator deadtime. We calculate corrections in two stages: if N_{PHA} is the number of PHA events in the encyclopedia tape for one volume, N_{trig} is the number of PHA trigger-rate counts in the same volume, and T_{rec} is the livetime recorded on the encyclopedia tape for that volume (leaving out stretches of time during which downlink noise obscured data so as to reduce N_{trig}), then

$$T_{PHA} = T_{rec} \left[\frac{N_{PHA}}{N_{trig}} \right] = \frac{N_{PHA}}{r_{LZ3*}} \tag{2.1}$$

is the effective livetime for the PHA events being analyzed, assuming that the triggering rate has no deadtime. r_{LZ3*} is the observed rate of LZ3* events; if there is some deadtime, we need to calculate the true rate R_{LZ3*} and use that instead.

To correct for LZ3* rate deadtime, we employ LET A. The L1 rate in each LET is an order of magnitude or more larger than the rates of the other detectors entering into the LZ3* trigger condition throughout the planetary encounter; thus we expect LZ3* deadtime to be dominated by L1 discriminator deadtime, so we can write

$$R_{LZ3*} = \frac{r_{LZ3*}}{1 - r_{L1} \times \tau_{L1}} \equiv C \times r_{LZ3*}, \tag{2.2}$$

where r_{L1} is the observed L1 rate and τ_{L1} is some average deadtime that must pass before the L1 discriminator (and thus the PHA-gate strobe) can be retriggered after a previous trigger. τ_{L1} is an average over all events; it is observed that the retrigger time between pulses will depend on the heights of the two pulses. A matrix of these retrigger times has been measured by Gehrels (1981), so that if R_j and r_j are the real and observed rates respectively of events in PHA channel j, and τ_{ij} is the retrigger time that must pass after an event in PHA channel i before an event in channel j can fire the L1 discriminator, then

$$R_j = \frac{r_j}{1 - \sum_i r_i \times \tau_{ij}}. \tag{2.3}$$

With LET A in singles mode throughout the encounter, we have a pulse-height spectrum $\{r_j\}$ for LA1, and we can convolve it with the retrigger times to obtain

$$C = \frac{R_{LZ3*}}{r_{LZ3*}} \approx \frac{R_{L1}}{r_{L1}} = \frac{\sum_j R_j}{\sum_j r_j} \tag{2.4}$$

using equation 2.3 for R_j. We cannot perform this calculation directly for LETs C and D, because the set $\{r_j\}$ is incomplete due to the requirement that L2 or L2 and L3 be triggered before the PHA gates open, and most particles triggering L1 (and contributing to its deadtime) will not satisfy this requirement. However, we can plot C *vs.* the observed LAZ3* rate (which is, in effect, the LA1 rate sampled every 6 seconds rather than every 96 seconds), and to the extent that we can put a smooth curve through the points we can then read off C for LETs C and D *vs.* their L1 rates. Figure 2.7 shows this relation; the points are as calculated for LA1 PHA data using equations 2.3 and 2.4, during the volumes when LETs C and D were in triples mode. (Though LET A does not change state, it shares PHA's with HET 1, which is toggling between high and low gains when LETs C and D are in doubles and triples modes respectively. When HET 1 is in high gain mode, residual signals from its detectors can contaminate the measurement of LA1 charge deposit and distort this calculation, so only data taken with HET 1 in the low gain state is used to calculate C.) Several volumes had LC1 or LD1 rates higher than the highest LAZ3* rate in this set; the C-*vs.*-rate relation was extended up to $\approx 8.6\times 10^3\,\text{sec}^{-1}$ (for LET D around 06:30 on day 237) by using equation 2.2 with a constant value of $\tau_{L1} = 92\,\mu\text{sec}$. The results are plotted *vs.* time in figure 2.8, along with the LAZ3* rate (LC1 and LD1 profiles are similar); two TET electron rates are included for future reference. Then with the correct geometry factors G for LETs C and D (actual active areas and separations of detectors were measured before launch), the flux in an energy bin k of width ΔE_k is

$$j_k = C \frac{N_k}{T_{PHA} G \Delta E_k} \tag{2.5}$$

for N_k the number of counts out of the set of N_{PHA} pulse-height-analyzed events that are assigned to bin k.

2.2.3. Results

Figures 2.9, 2.10, 2.11, and 2.12 show the fluxes for LETs C and D derived from the above analysis, as a function of time through the encounter, for the five energy bins (two doubles, three triples) from which points will be selected for fitting to magnetospheric models below. Closest approach to the planet is at 03:56 UTC on 25 Aug 89 (day 237), almost at the center of the figures. "One-sigma" error bars are as approximated for Poisson statistics by Gehrels (1986): for N particles observed, the mean μ is estimated to lie within

$$N - \sqrt{N - \frac{1}{4}} < \mu < N + \sqrt{N + \frac{3}{4}} + 1; \tag{2.6}$$

straight vertical lines are upper limits ($\mu < 1 + \sqrt{3/4}$) where no counts were observed in a two-volume interval. These errors are strictly statistical; assuming the τ_{ij} measured by Gehrels (1981), we can estimate the fractional error in C, and the resultant fractional error in j, from the spread of the LET A points about the adopted line in figure 2.7. It should be negligible compared to the statistical errors except perhaps along the extension to high LD1 rates. A larger source of systematic error in fluxes is likely to be the cuts used to assign particles to energy bins; this might be up to 20%, which is small compared to the statistical errors in all of the energy bins at most times. In any case, the modeling approach employed in chapter 5 will not prove to be sensitive enough that errors of this size will make much difference in the quality of the resultant magnetospheric model.

Figure 2.7

Correction factor C in equations 2.2 and 2.4, plotted *vs.* LAZ3* rate or LC1 or LD1 rate, as appropriate. Points are calculated from two-volume samples of LA1 PHA data as described in the text, and the dotted line is the continuous curve adopted to read out C using the LC1 or LD1 rate. Solid curves are extensions for higher rates calculated using equation 2.2 for different values of τ_{L1}, as labeled; 92 microseconds was the value adopted for use in analysis.

Figure 2.8

(a) Correction factor C in equations 2.2 and 2.4 (dotted line for LET A, dashed for LET C, and solid for LET D) and rate plots in the inner magnetosphere of Neptune, in sec^{-1}: (b) LAZ3* and (c) TET D1 and D2. LAZ3* responds primarily to piled-up electrons of tens of keV energy; the TET electron rates are included for later reference. D1 responds to electrons above ≈1 MeV, while D2 measures electrons above ≈2.5 MeV; the curve for D2 is lowered by one decade for clarity in the figure.

Figure 2.7

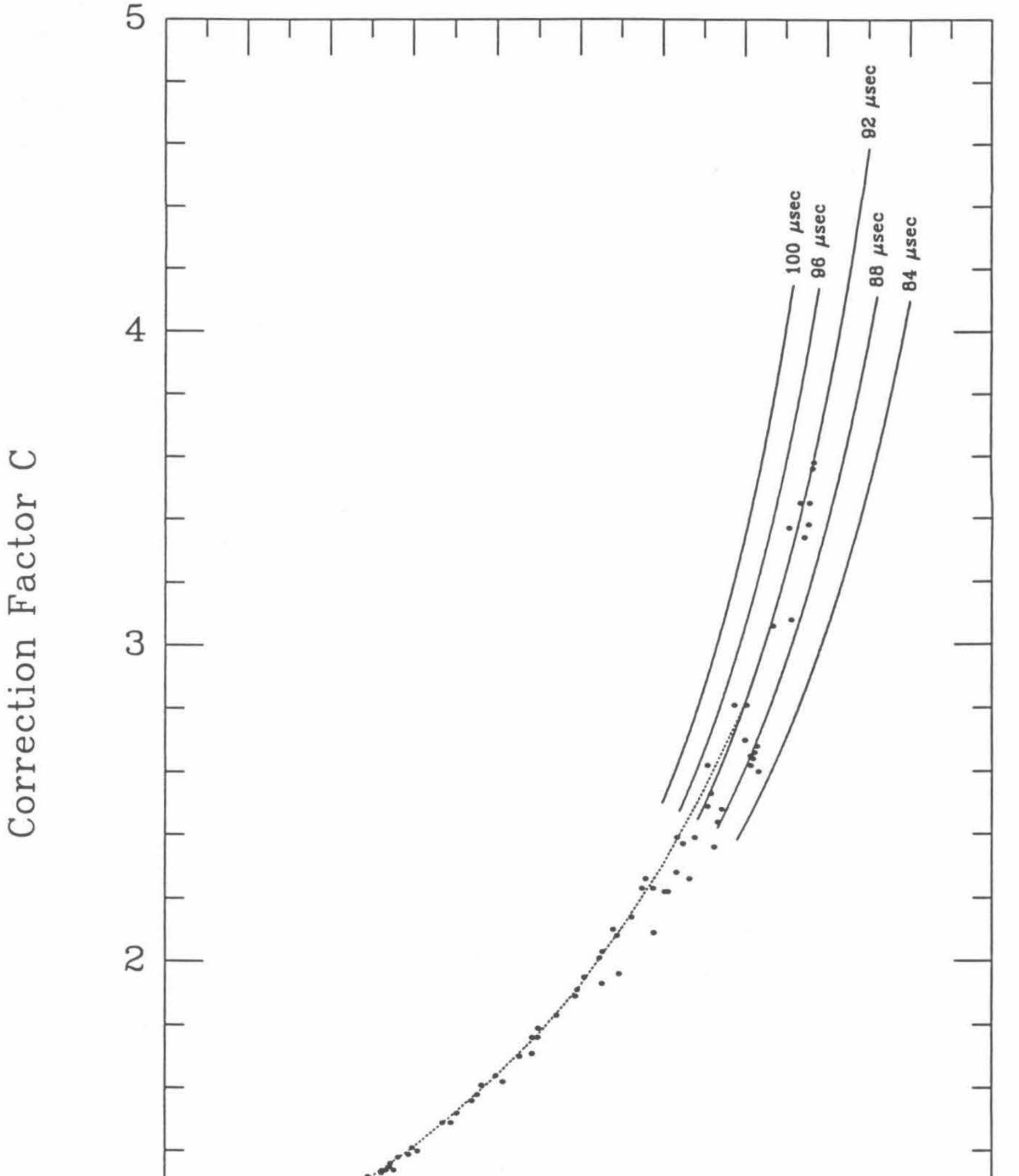
Correction Factor C
1
2
3
4
5
0
1
2
3
4
5
6
7
8
9
10
Observed LAZ3* or L1 Rate, 1000 sec^{-1}
100 μsec
96 μsec
92 μsec
88 μsec
84 μsec

Figure 2.8

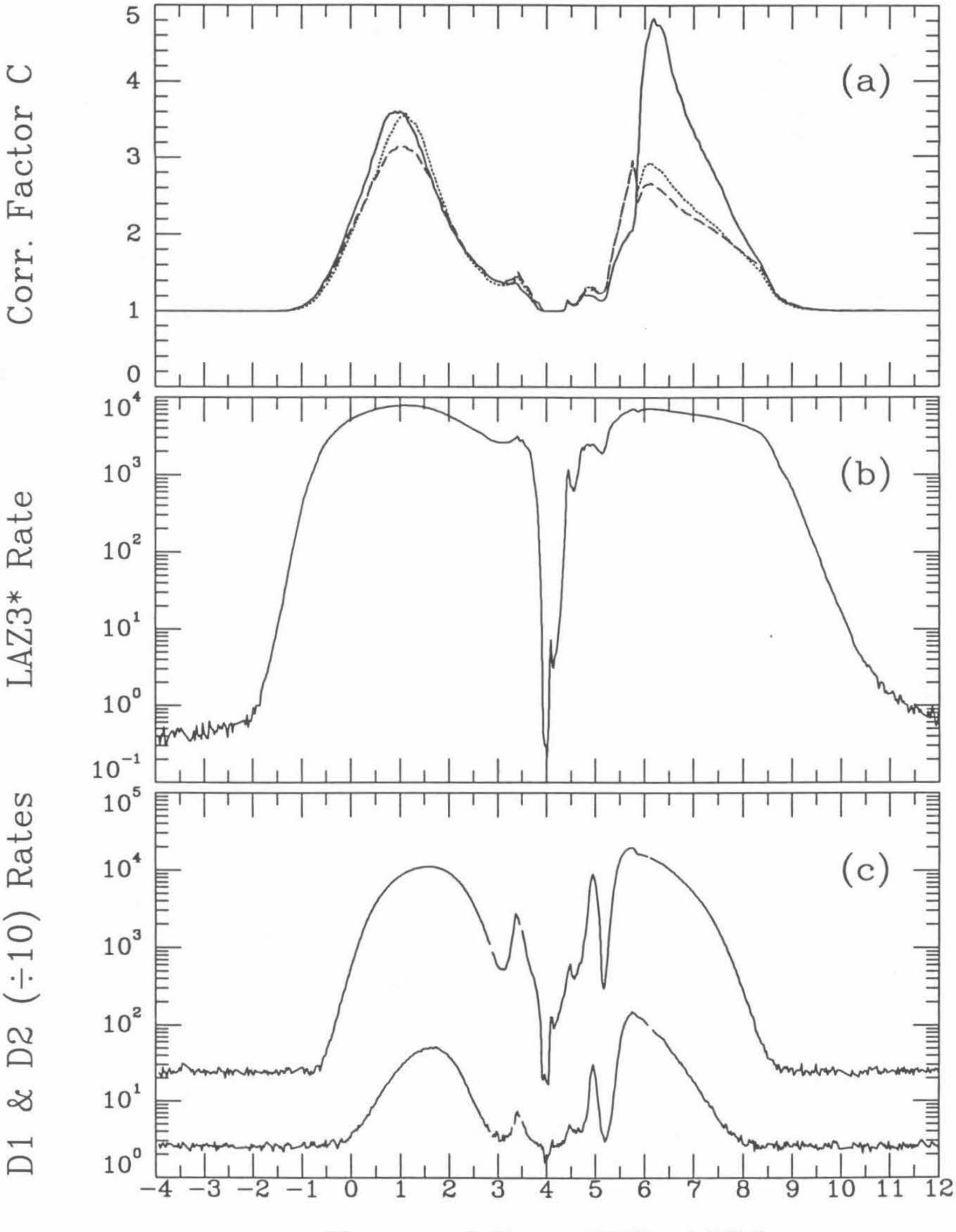
Corr. Factor C
5
4
3
2
1
0
(a)
LAZ3* Rate
10^4
10^3
10^2
10^1
10^0
10^{-1}
(b)
D1 & D2 (÷10) Rates
10^5
10^4
10^3
10^2
10^1
10^0
(c)
−4
−3
−2
−1
0
1
2
3
4
5
6
7
8
9
10
11
12
Hour of Day 237, 1989

Figure 2.9

LET C proton fluxes observed in the inner magnetosphere of Neptune, in the two doubles bins: (a) 1.9 to 2.1 MeV and (b) 2.1 to 2.9 MeV. Fluxes are in $(\mathrm{cm}^2\,\mathrm{sr}\,\mathrm{sec}\,\mathrm{MeV})^{-1}$. Vertical lines extend downward from upper limits.

Figure 2.10

LET D proton fluxes in the two doubles bins, as in figures 2.9.

Figure 2.11

LET C proton fluxes in the three triples bins: (a) 3.2 to 3.7 MeV, (b) 3.7 to 4.3 MeV, and (c) 4.3 to 5.0 MeV. Fluxes are in $(\mathrm{cm}^2\,\mathrm{sr}\,\mathrm{sec}\,\mathrm{MeV})^{-1}$. Vertical lines extend downward from upper limits.

Figure 2.12

LET D proton fluxes in the three triples bins, as in figures 2.11.

Figure 2.9

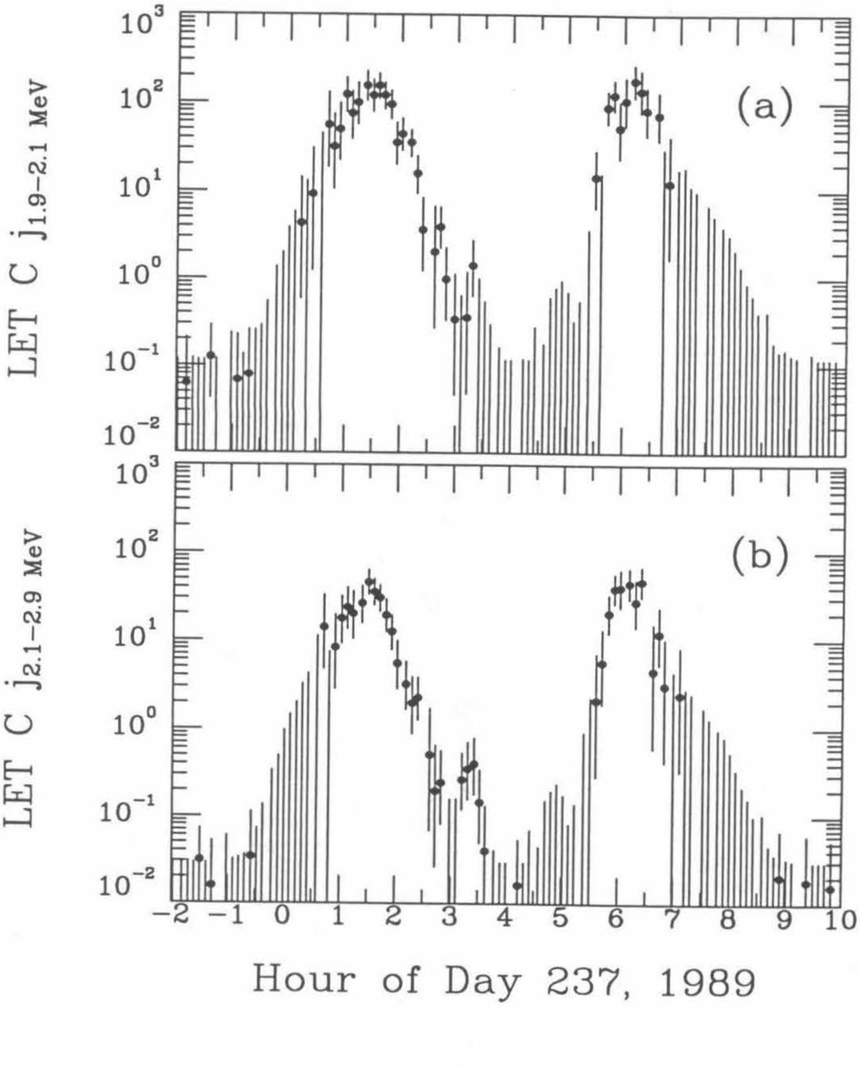
10^3
10^2
10^1
10^0
10^{-1}
10^{-2}
LET C $j_{1.9-2.1\ \mathrm{MeV}}$
(a)
10^3
10^2
10^1
10^0
10^{-1}
10^{-2}
LET C $j_{2.1-2.9\ \mathrm{MeV}}$
(b)
−2
−1
0
1
2
3
4
5
6
7
8
9
10
Hour of Day 237, 1989

Figure 2.10

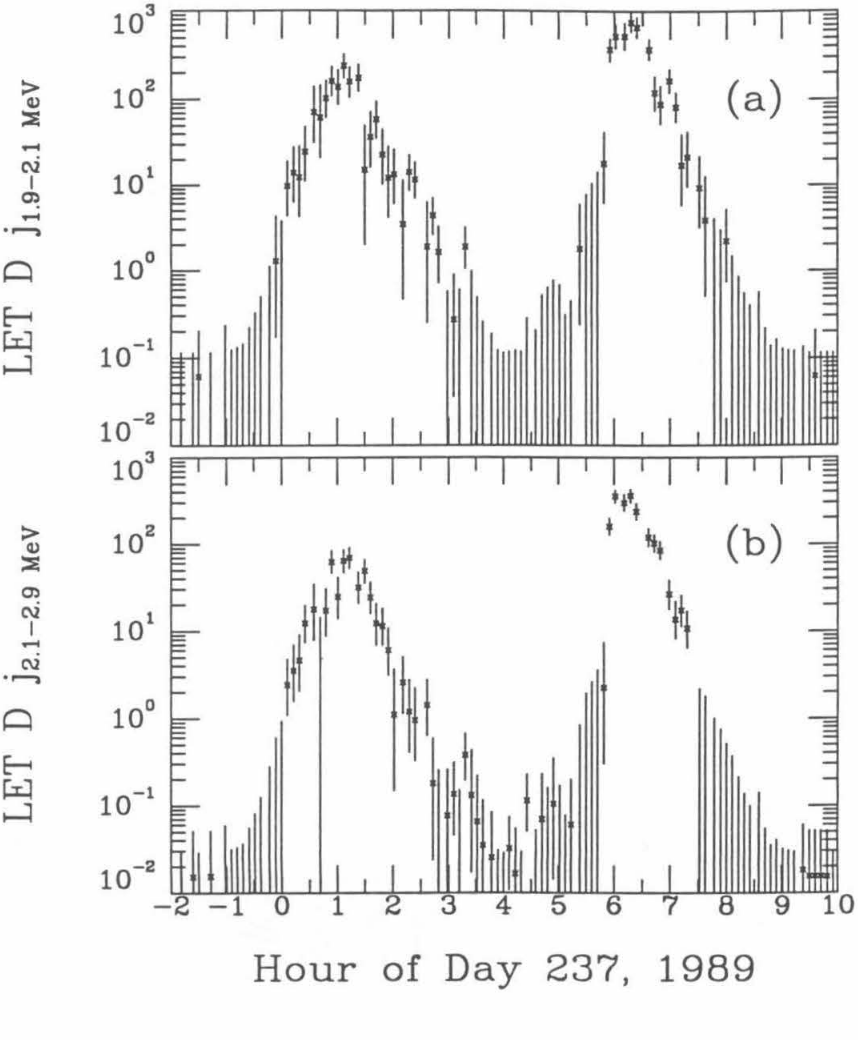
LET D $j_{1.9-2.1\ \mathrm{MeV}}$
LET D $j_{2.1-2.9\ \mathrm{MeV}}$
(a)
(b)
10^3
10^2
10^1
10^0
10^{-1}
10^{-2}
−2
−1
0
1
2
3
4
5
6
7
8
9
10
Hour of Day 237, 1989

Figure 2.11

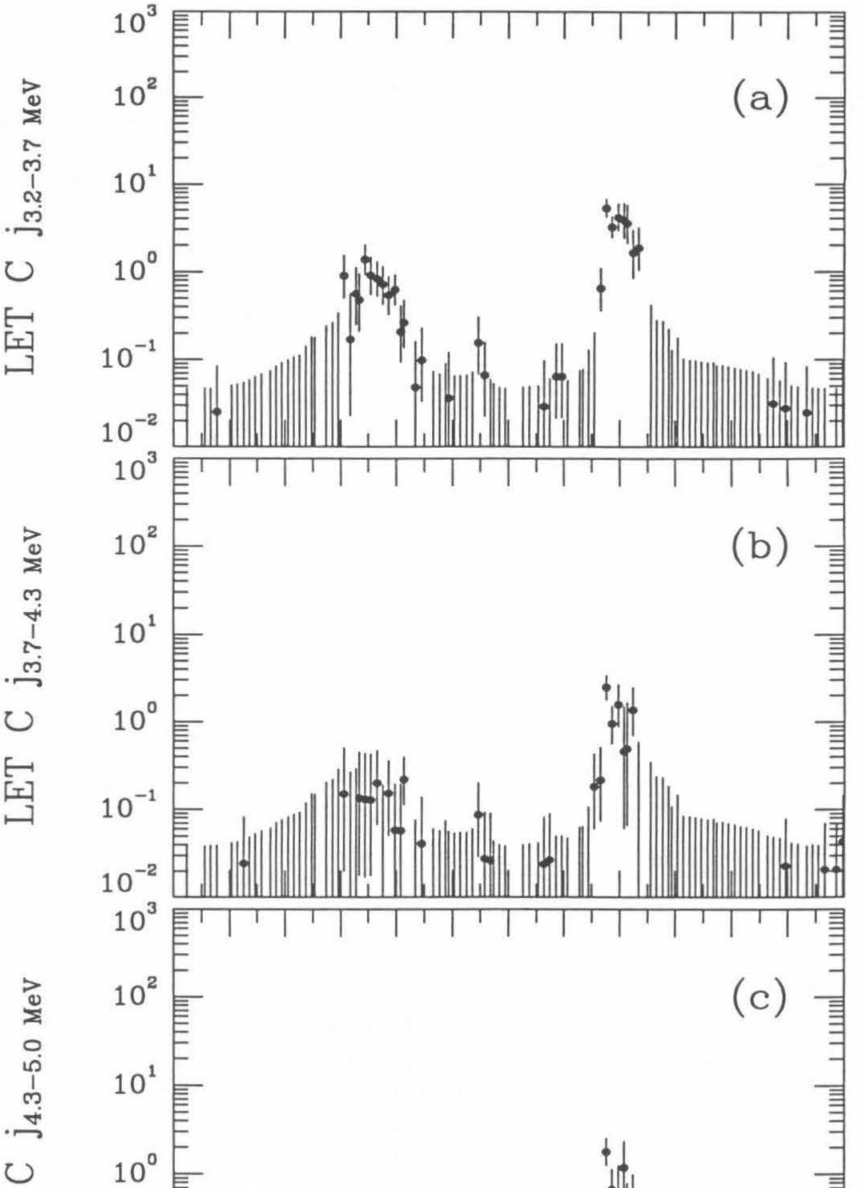
LET C $j_{3.2-3.7\ \mathrm{MeV}}$
LET C $j_{3.7-4.3\ \mathrm{MeV}}$
LET C $j_{4.3-5.0\ \mathrm{MeV}}$
(a)
(b)
(c)
10^3
10^2
10^1
10^0
10^{-1}
10^{-2}
−2
−1
0
1
2
3
4
5
6
7
8
9
10
Hour of Day 237, 1989

Figure 2.12

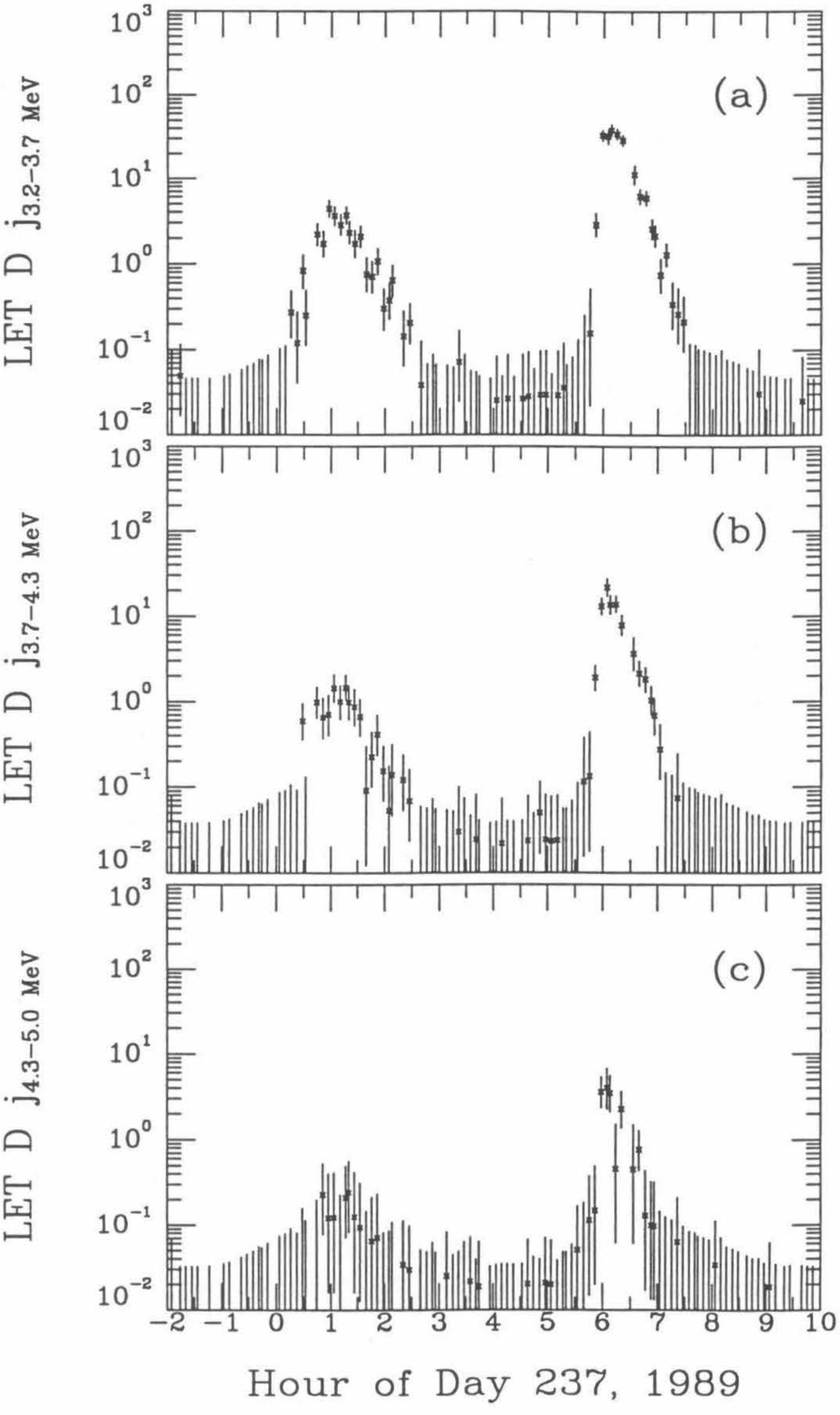
LET D $j_{3.2-3.7\ \mathrm{MeV}}$
LET D $j_{3.7-4.3\ \mathrm{MeV}}$
LET D $j_{4.3-5.0\ \mathrm{MeV}}$
(a)
(b)
(c)
10^{3}
10^{2}
10^{1}
10^{0}
10^{-1}
10^{-2}
−2 −1 0 1 2 3 4 5 6 7 8 9 10
Hour of Day 237, 1989

Chapter 3

Particle Motions and Classification

3.1. Periodic Motions and Adiabatic Invariants

3.1.1. Particles in a Dipolar Magnetic Field

In the preceding chapter, we considered incident protons as isolated particles impinging on the LETs, without regard to their relation to one another or to the magnetic field of the planet that holds them in its vicinity (other than to establish a time sequence of the observations). This magnetic field organizes the charged particles in its grip, however, in such a way that we can probe and draw conclusions about the entire magnetosphere based on observations made during a single pass through it as we fly by the planet.

As a first approximation to a planetary magnetic field, consider a dipolar field: in polar coordinates centered on and aligned with the magnetic dipole moment $\mathbf{k}_0$,

$$B_r = \frac{2k_0}{r^3}\sin\lambda, \quad B_\lambda = -\frac{k_0}{r^3}\cos\lambda, \quad B_\phi = 0, \tag{3.1}$$

where k_0 is the magnitude of $\mathbf{k}_0$. Discussion below largely follows that of Roederer (1970), with some corrections of formulae, and Schulz and Lanzerotti (1974). Field lines are of the shape shown in figure 3.1; it is convenient to specify position in the magnetic field in terms of the magnetic latitude λ above and r_0 or L, where r_0 is the width of the field line at its widest point (at the magnetic equator) and L is this distance divided by R_P, the planetary radius. In these coordinates, the magnitude of the field is

$$B = \frac{k_0}{R_P^3}\frac{1}{L^3}\frac{\sqrt{4-3\cos^2\lambda}}{\cos^6\lambda} \equiv \frac{B_P}{L^3}\frac{\sqrt{4-3\cos^2\lambda}}{\cos^6\lambda}. \tag{3.2}$$

(If the dipole is at the center of the planet, B_P is the magnetic field strength at the surface on the magnetic equator.)

A charged particle in such a field will execute three periodic motions: first is the usual cyclotron motion, wherein the particle describes a helix whose axis is parallel to the local magnetic field **B**, with a period

$$\tau_c \equiv \frac{2\pi}{\omega_c} = \frac{2\pi\gamma m_0 c}{qB} = \frac{2\pi\gamma m_0 c L^3}{qB_P}\frac{\cos^6\lambda}{\sqrt{4-3\cos^2\lambda}}, \tag{3.3}$$

where γ is the usual relativistic factor and m_0 is the particle's rest mass, q is its charge, and c is the speed of light. Associated with a periodic motion we may define a canonical angular momentum or action integral that will be adiabatically conserved, *i.e.*, it will be conserved when the external parameters (in this case, the local magnetic field) vary slowly on the time-scale of the periodic motion: if $\mathbf{q}$ and $\mathbf{\Pi}$ are canonical coordinates (position and momentum) for the system, then

$$J = \oint \mathbf{\Pi}\cdot d\,\mathbf{q} \tag{3.4}$$

is such a conserved quantity, where the integral is taken over one complete cycle of the periodic motion (see, *e.g.*, Goldstein (1950)). For a magnetostatic problem, the momentum canonically conjugate to the ordinary position vector **r** is

$$\mathbf{\Pi} = \mathbf{p} + \frac{q}{c}\mathbf{A}, \tag{3.5}$$

where **p** here is the ordinary momentum and **A** is the vector potential of the magnetic field. Let α be the pitch angle of the particle's helical trajectory, ranging from 0° for a particle moving parallel to **B** to 90° for one moving perpendicularly; then the integral in equation 3.4 for cyclotron motion is (after a little algebra)

$$J_1 = \frac{\pi c p^2 \sin^2\alpha}{|q|B} \equiv \frac{2\pi m_0 c}{|q|}M, \tag{3.6}$$

where $M \equiv \dfrac{p^2\sin^2\alpha}{2m_0 B}$ is usually called the first adiabatic invariant or the magnetic moment, and is related to the action integral J_1 by the constant factor shown; units used herein for M are MeV per Gauss.

The second periodic motion is the "bounce" motion, wherein the particle travels up and down the magnetic field line, trapped between the strong-field regions near the magnetic poles as in a "magnetic bottle." To the extent that this motion is on a timescale much slower than the cyclotron period, we can consider the local magnetic field at the particle's position (which changes as the particle travels up and down the field line) to be slowly varying on the timescale of the cyclotron period, so that M is conserved. We can then consider the "guiding center," the instantaneous center of curvature of the particle's helical path, to move along the field line at a speed $v_{||} = \frac{p}{\gamma m_0}\cos\alpha$, where α is related to the magnetic latitude through equation 3.2 and the constancy of M: in a static magnetic field (on the timescale of the bounce motion) the particle's energy (whence p) is conserved, so conservation of M implies

$$\frac{\sin^2\alpha}{B} = \text{constant} = \frac{1}{B_{mirr}} = \frac{\sin^2\alpha_0}{B_0}, \tag{3.7}$$

where B_{mirr} is the magnetic field strength at which $\alpha = 90°$ and motion along the magnetic field stops (and reverses, or "mirrors") and the subscript zeroes indicate quantities measured at the magnetic equator. Then for λ_{mirr} the magnetic latitude of the mirror point, the period of the bounce motion is

$$\tau_b \equiv \frac{2\pi}{\omega_b} = \oint\frac{ds}{v_{||}} = \frac{4R_P L}{\beta c}\int_0^{\lambda_{mirr}} \frac{\cos\lambda\,\sqrt{4-3\cos^2\lambda}}{\left[1-\frac{B(\lambda)}{B(\lambda_{mirr})}\right]^{1/2}}d\lambda \equiv \frac{4R_P L}{\beta c}H(\lambda_{mirr}). \tag{3.8}$$

$H(\lambda_{mirr})$ ranges from $\frac{\pi\sqrt{2}}{6} \approx 0.740$ for $\lambda_{mirr} = 0°$ to $1 + \frac{\log(2+\sqrt{3})}{2\sqrt{3}} \approx 1.380$ for $\lambda_{mirr} = 90°$. Integrating equation 3.4 along the field line over one cycle of the bounce motion, we find the next action integral

$$J_2 = \oint p\cos\alpha\,ds = p\oint\left[1-\frac{B(s)}{B_{mirr}}\right]^{1/2} ds$$

$$= 4pLR_P\int_0^{\lambda_{mirr}}\left[1-\frac{B(\lambda)}{B(\lambda_{mirr})}\right]^{1/2}\cos\lambda\sqrt{4-3\cos^2\lambda}\,d\lambda$$

$$\equiv 2pI \equiv 2\sqrt{2m_0M}\ K. \tag{3.9}$$

I is a field-geometric quantity (that is, it is defined without reference to the particle's p or M), and is convenient to use when considering a single field line; it ranges from 0 for $\lambda_{mirr} = 0^\circ$ to $2LR_PH(90^\circ)$ for $\lambda_{mirr} = 90^\circ$. For processes that conserve J_1 (whence M) and J_2, K is a convenient field-geometric quantity that is conserved even when p is not conserved (for example, in the radial diffusion processes considered in chapter 5); figure 3.1 shows lines of constant K (in units of $R_P\sqrt{\text{Gauss}}$) in a dipolar magnetic field. Finally, J_2 is commonly called just J, the second adiabatic invariant.

The third periodic motion of a particle in a dipolar field is a drift in azimuth around the axis defined by the magnetic dipole $\mathbf{k}_0$. This is due partly to "gradient" drift, wherein the radius of gyration tightens when the particle's cyclotron motion takes it toward the planet into a stronger field and loosens when it moves away, and partly to "curvature" drift, wherein the "centrifugal force" of the particle's motion along the curved field line has an effect like that of an electric field directed outward from the planet (for positive particles), producing a drift in the direction of the cross product of the electric and magnetic fields. The drift period is

$$\tau_d \equiv \frac{2\pi}{\omega_d} = 2\pi\frac{\tau_b}{\Delta\phi}, \tag{3.10}$$

where

$$\Delta\phi = \frac{3\gamma\beta m_0c^2L^2}{2qB_PR_P}4\int_0^{\lambda_{mirr}}\frac{1-\sin^4\lambda}{(4-3\cos^2\lambda)^{1.5}}\frac{2-\dfrac{B(\lambda)}{B(\lambda_{mirr})}}{\left[1-\dfrac{B(\lambda)}{B(\lambda_{mirr})}\right]^{1/2}}d\lambda$$

$$\equiv \frac{3\gamma\beta m_0c^2L^2}{2qB_PR_P}F(\lambda_{mirr}) \tag{3.11}$$

is the magnetic longitude interval drifted in one bounce period τ_b; $F(\lambda_{mirr})$ ranges from $4H(0^\circ)$ for $\lambda_{mirr} = 0^\circ$ to $\frac{8}{3}H(90^\circ)$ for $\lambda_{mirr} = 90^\circ$. If the drift motion is slow relative to the

Figure 3.1

Azimuthal section showing L and K for a dipolar magnetic field: field lines are shown as solid lines for $L = 4$ to 20 by steps of 4, while labeled (dotted) curves are lines of constant K. Labels are the values of K in $R_P \sqrt{G}$ for a magnetic moment of $k_0 = 0.130 G\, R_P^3$, as adopted for Neptune; these values would scale with the square root of $B_P = k_0 / R_P^3$. The heavy circle represents the planet, and the vertical scale is labeled in units of R_P.

Figure 3.1

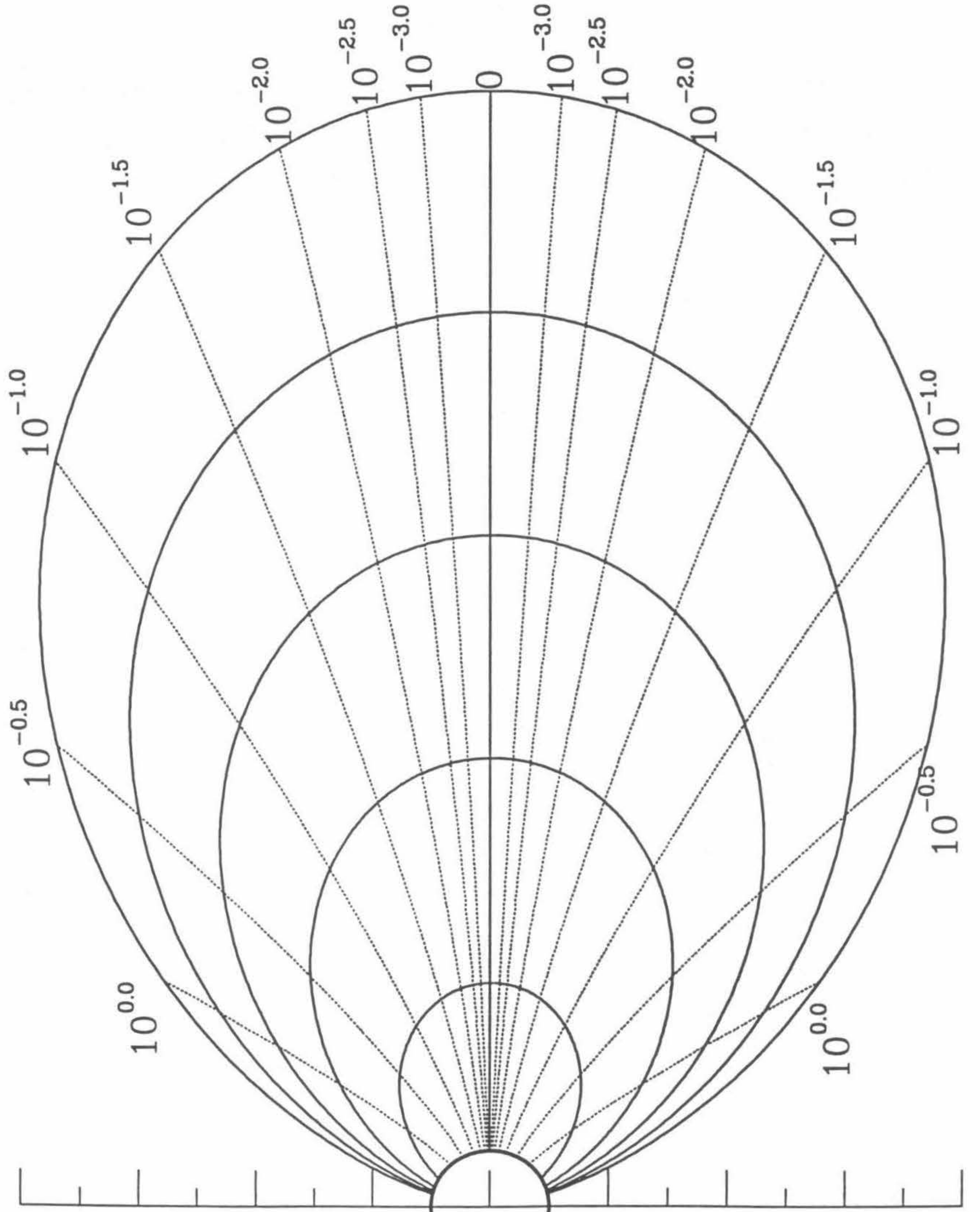

bounce motion, the contribution from the **p** term to the integral in equation 3.4 is negligible relative to that from the **A** term for this periodic motion, which, by Stokes' Theorem, is proportional to the magnetic flux through the surface enclosed by the path of integration, so the action integral for this periodic motion is

$$J_3 = \frac{q}{c}\Phi = \frac{|q|}{c}\frac{2\pi B_P R_P^2}{L}. \tag{3.12}$$

Φ is sometimes called the third, or flux, adiabatic invariant. We now have a trio of canonical angular momenta which (with their associated angle variables, the phases of their respective periodic motions) can be used to identify particles completely; hereinafter reference will usually be made to M, K, and L, which are an equivalent set.

3.1.2. Particles in a Complex Magnetic Field

A real planetary magnetic field will generally have a form involving higher-order multipolar field components (beyond the dipole), due to the complex distribution of the dynamo currents that generate the planet's internal magnetic field. External currents from the region of the magnetopause or from plasma within the magnetosphere can also contribute to the magnetic field; wherever the planet's internal higher-order terms are the dominant contributions to the non-dipolar part of the magnetic field, however, the above invariants can be used to map the trapped particle distribution onto a dipolar field.

M is defined at the point of observation in equation 3.6, in terms of the local values of the magnetic field magnitude B, particle momentum p, and pitch angle α; this makes no reference to the dipolar or non-dipolar nature of the magnetic field. The relations in equation 3.7 between values of α and B during the particle's bounce motion likewise follow only from the adiabatic assumptions leading to conservation of M, and should hold in the real field; in particular, B_{mirr} can be deduced from the values of α_0 and B_0.

Given B_{mirr} and the choice of a particular field line, the field-geometric quantity I (or K) can be calculated directly using equation 3.9, using the real relation of B and the distance s along the real field line. In a dipolar field, equation 3.9 shows that I is LR_P times an increasing function of the mirror latitude, which is in turn an increasing function of the dimensionless parameter $Q \equiv L^3 R_P^3 \frac{B_{mirr}}{k_0}$; therefore $I^3 \frac{B_{mirr}}{k_0}$ is Q times this function of Q, and we can invert to obtain Q as a function $F\left[I^3 \frac{B_{mirr}}{k_0}\right]$, which has been tabulated and parametrized by McIlwain (1961, 1966). Fixing R_P and k_0, this gives L as a function of B_{mirr} and I; the value of L determined thus for particles mirroring at a given point in a non-dipolar field is called the McIlwain L. The usefulness of this borrowing of the relation F from the dipolar field follows from the fact that most of the contribution of the integrand in equation 3.9 for I comes from near the magnetic equator on the field line, which is the region most distant from the planet and which is therefore where the higher-order internal terms in the magnetic field (which fall off with distance more rapidly than the dipole contribution) are smallest relative to the dipole. Thus, if we start with a dipolar field close to the real field and pick a field line with magnitude B_0 and a particle with pitch angle α_0 at the magnetic equator, and then turn on the higher-order terms of the real field, the positions of the mirror points (near the planet) will change substantially but the equatorial field will change little. B_0 and α_0 and therefore B_{mirr} will be nearly the same, as will I; thus McIlwain's L value will be nearly the same for all particles initially mirroring along a given field line. As these particles drift around the planet, conservation of K and M implies that they will stay on lines with the same Ls; in a magnetic field with azimuthal asymmetry, the field lines traversed by particles with different values of B_{mirr} will diverge as the particles drift, so that drift shells osculating at one longitude will be split at others (Stone 1963). However, McIlwain's L labels the drift shells of different particles in a way that provides a simple mapping back to the more-easily-visualized dipolar field in which such shells, near one another in the real field, would be degenerate (Roederer 1970). The choice of a magnitude k_0 for the calculation in the non-dipolar field must be consistent throughout, but its exact value is not crucial.

3.2. Observations at Neptune

Preliminary analysis of Neptune charged particle data used an Offset (from the planet's center), Tilted (relative to the rotation axis) Dipole model (OTD2) of the magnetic field (Ness 1990); because Voyager 2 passed within 0.18 Neptune radii of the cloud tops, well into the near-field region where higher-order terms were not diluted by distance, the field model (Connerney *et al.* 1991) to fit the whole data set of magnetometer observations required internal spherical harmonic terms to order 8, and also included a weak uniform external field; it is referred to as I8E1. This magnetic field model was supplied to other Voyager instrument teams before publication, and Selesnick (1990) calculated from it the trajectory of Voyager 2 in magnetic coordinates (B and McIlwain L), and also the orientation of the CRS telescopes relative to the local magnetic field and to the gradient of its magnitude.

LETs C and D typically observed particles which mirrored at latitudes away from the spacecraft; moreover, the large gyroradii of protons at CRS energies in the weak planetary magnetic field typically meant that the field line on which the guiding center of the particles was located was not one at the same L as the spacecraft. Rather than go through the calculation described above for the particles observed at a given time by each telescope, the magnetic field was approximated locally by a section from a dipolar magnetosphere: given L and B/B_0 for the spacecraft in the real field (as represented by the I8E1 model), we can place the spacecraft in a model dipolar magnetic field at the appropriate L and magnetic latitude λ_m, and given the orientation of the telescope axis with respect to the real field and to its gradient we can use the same angles to orient it relative to these vectors in the dipolar field. Assuming a proton of a given energy flying into the telescope, we have a velocity, which with the local magnetic field gives an acceleration, which in turn allows us to calculate the instantaneous magnitude and direction of the curvature of the proton's path; this is, of course, just the vector between the proton and its gyrocenter, so we can place the gyrocenter in the dipolar model and calculate its L directly. One source of error in identification of the L-shell by this method is shell-splitting, whereby particles whose guiding centers cross the magnetic equator at the same point but which have different pitch angles α_0 may not lie on a common drift shell, with the mirror point of one particle farther in toward the planet than the corresponding point on the field line whereon the other mirrors. This was calculated by Selesnick and

Stone (1991b) (by the method of Stone (1963)) to be less than 1% in the range of L where the CRS observations took place. Thus losing information about the mirror point of the particle by using the simplified method described here introduces a negligible error; furthermore, since distortion of the magnetic field lines from the dipolar model is what causes magnetic shell splitting, the local approximation of the field as a gyroradius-sized piece of a dipolar field should also be good enough. Finally, another source of error in identification of the L-shell observed is that for large gyroradii the instantaneous center of curvature does not remain exactly on a given magnetic field line, as implicitly assumed above; however, an exact calculation of the orbits of equatorial protons (whose large gyroradii should show this effect most strongly) in the CRS energy range, using the formulae of appendix 2, shows that the fractional error in L is at most a couple of percent. Thus we can use the method described to identify the L-shell observed by each LET, and save a lot of calculation.

M doesn't require a model, just the local $\mathbf{B}$ and $\mathbf{p}$ for the proton, to calculate; it remains to find K. We need B_0 for the guiding center field line; we have B_0 and L for the spacecraft from the I8E1 field model, so assuming a dipole-like L^{-3} dependence for B_0 we can find B_0 at the L of the guiding center. M gives us B_{mirr}, and that with B_0 for the guiding center field line gives us λ_{mirr}, which with L yields K via equation 3.9. The values of L, K, and M for protons of energy 3.45 MeV (approximately in the middle of our energy range) entering LETs C and D are shown as a function of time in figures 3.2, along with the values for particles with guiding centers at the spacecraft's L that mirror at the spacecraft's position on the field line. Plots for other energies would look qualitatively similar; the displacement in L of the LET points from the spacecraft curve in figure 3.2(a) would increase with energy, which would have smaller effects on K (which depends on L and B_0), and the normalization of the curves for M would change in direct proportion to the energy (for nonrelativistic protons). The time period in these figures is the same as that in figures 2.9, 2.10, 2.11, and 2.12; closest approach to the planet is again near the center of the time axis. Features to note are the turnaround in L on the inbound leg of the trajectory, caused by an excursion to high magnetic latitudes as the spacecraft approaches the planet (as is most clearly seen in the plot of K), and the abrupt shift in the K and M observed by the LETs just before 0600, which is due to a spacecraft roll maneuver that changes the local pitch

Figure 3.2

Values of (a) L, (b) K, and (c) M for 3.45 MeV protons observed by LETs C (circles) and D (crosses), in the I8E1 model. Continuous dotted lines are for particles of this energy on the spacecraft's L-shell, mirroring at the position of the spacecraft.

Figure 3.2

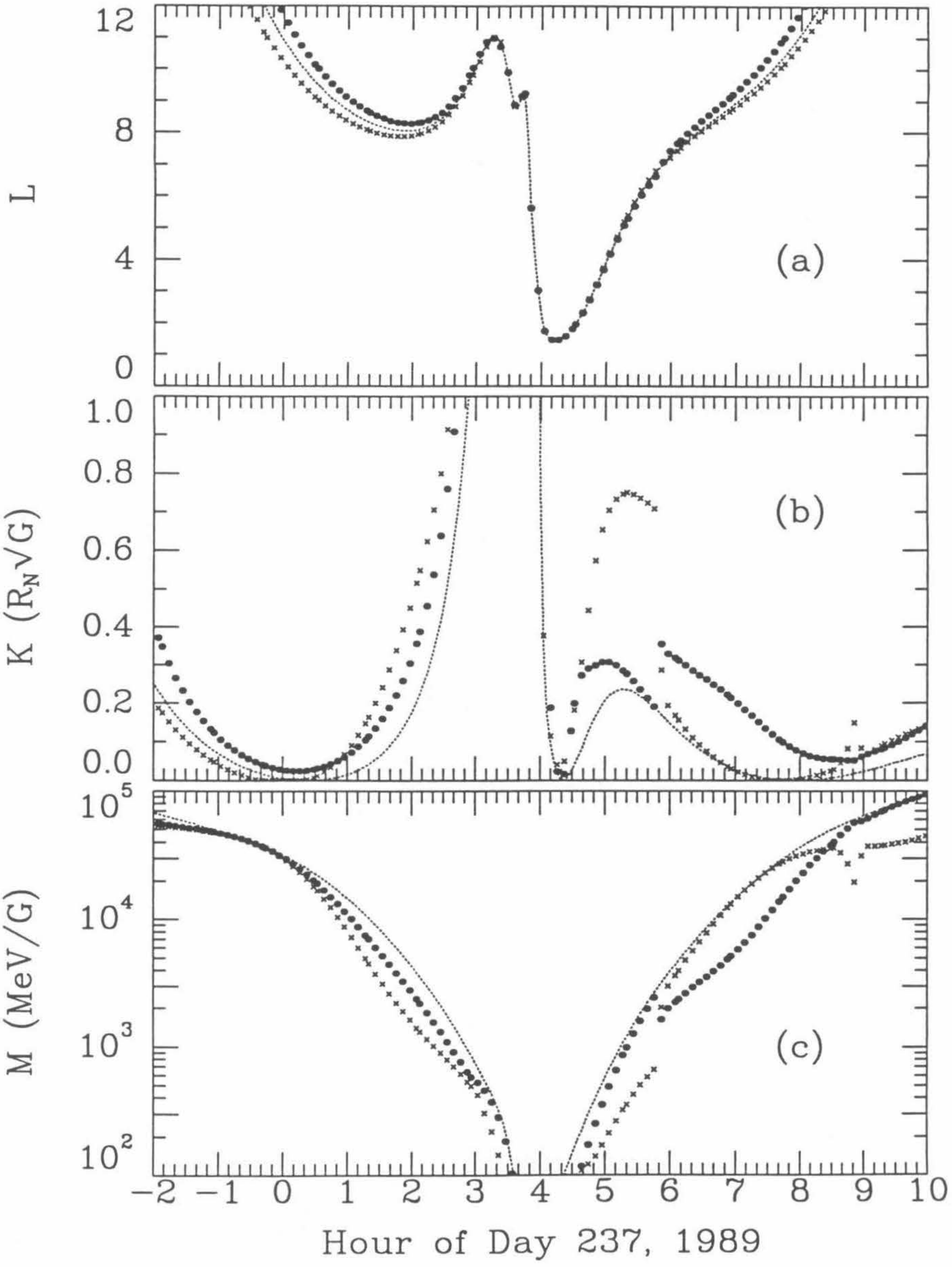
L
0
4
8
12
(a)
K ($R_N\sqrt{G}$)
0.0
0.2
0.4
0.6
0.8
1.0
(b)
M (MeV/G)
10^2
10^3
10^4
10^5
(c)
−2
−1
0
1
2
3
4
5
6
7
8
9
10
Hour of Day 237, 1989

angle observed by each LET (another roll maneuver is seen from about 0830 to 0900). The effect of this roll maneuver is visible in the particle rates plotted in chapter 2, as a step in the rates for D1, D2, and LAZ3* in figures 2.8, and as an abrupt jump in the LET D rates in figures 2.10 and 2.12. This jump, and the absence of such a drastic jump in LET C rates in figures 2.9 and 2.11, will prove particularly important to the magnetospheric models developed in chapter 5. However, it renders suspect one point on each of the subfigures, the particle events for which were accumulated during the roll maneuver and as such cover a wide span of adiabatic invariants; the doubles points are the ones centered on 05:48:48, and the triples points are centered on 05:52:00. With these exceptions, points chosen for comparison with the results of magnetospheric models in chapter 5 were those between the times listed in table 3.1; these were the continuous sequences (minus a few data gaps, and the roll maneuver) within which there were no two adjacent points comprising fewer than two proton counts in the energy bin (as determined by the analysis in chapter 2, results of which appear in figures 2.9, 2.10, 2.11, and 2.12), with the further exception that the inbound doubles data sets were cut off a little earlier because, first, the flux had declined to the point where background subtraction (heretofore ignorable) would be necessary, and second, the spacecraft was getting very close to the planet at high magnetic latitudes, where the magnetic field model was presumed to be least accurate. All told, 210 spectral points (44 LET C inbound, 32 LET C outbound, 76 LET D inbound, and 58 LET D outbound) were selected to be fit.

Table 3.1 Times for Model Fitting (Day 237, 1989)

Energy (MeV)	LET C inbound	LET D inbound	LET C outbound	LET D outbound
1.9-2.1	0:43:12-2:25:36	0:04:48-2:25:36	5:40:48-6:38:24	5:53:36-7:20:00
2.1-2.9	0:52:48-2:25:36	0:04:48-2:25:36	5:34:24-6:51:12	5:53:36-7:20:00
3.2-3.7	1:2:24-2:28:48	0:14:24-2:28:48	5:37:36-6:22:24	5:56:48-7:29:36
3.7-4.3	---	0:43:12-2:00:00	5:37:36-6:09:36	5:56:48-7:04:00
4.3-5.0	---	---	5:44:00-6:06:24	5:37:36-6:48:00

Chapter 4

Satellite Absorption of Charged Particles

4.1. The Diffusion Equation

In this chapter and the next we construct models for the absorption and diffusive transport of protons in Neptune's magnetosphere, and attempt to reproduce the observed fluxes. A more fundamental quantity than the observed flux j is the phase-space density f, the number of particles per unit volume in the six-dimensional phase space of position $\mathbf{r}$ and ordinary momentum $\mathbf{p}$, which is related to the observed flux by

$$f = \frac{j}{p^2}. \tag{4.1}$$

Because the transformation from $\mathbf{r}$ and $\mathbf{p}$ to the canonical position $\mathbf{r}$ and momentum Π of equations 3.5 has unit Jacobian, and because the ratio between volume elements (and therefore the inverse of the ratio between phase-space densities) in two different coordinate systems is just the Jacobian, the phase-space density f in ordinary phase space is numerically equal to the phase-space density in canonical phase space (Schulz and Lanzerotti 1974). The three action integrals J_1, J_2, and J_3 as defined in chapter 3, together with their conjugate angle coordinates, are related by a canonical transformation to $\mathbf{r}$ and $\boldsymbol{\pi}$, from which they were generated; since the volume element in phase space is conserved by a canonical transformation (the Jacobian of the transformation is again unity) (Goldstein 1950), the phase-space density in the system of the J_is and their conjugate angles is again numerically equal to f. Finally, the adiabatic invariants M, J, and Φ differ from J_1, J_2, and J_3 only by multiplicative constants. Thus if random perturbations to the system result in non-conservation of one or more of the J_is, so that we can write a diffusion equation for the phase-space density in these variables, then we can write for f the diffusion equation

$$\frac{\partial f}{\partial t} = \frac{1}{G}\nabla\cdot(G\mathbf{D}\cdot\nabla f) + S \tag{4.2}$$

(Haerendel (1968), borrowing notation from Selesnick and Stone (1991a)). G is the Jacobian of the (not necessarily canonical) transformation from the three adiabatic invariants to the coordinates in use (which differs only by a multiplicative constant from the Jacobian of the transformation from J_1, J_2, and J_3 to the coordinates in use), and the diffusion tensor **D** and gradient are relative to the new coordinates; S is the net source of protons. Haerendel (1968) actually derives this equation for a phase-space density averaged over the phases of the three periodic motions; as we will see, residence times for protons in the magnetosphere are considerably longer than the longest (drift) periodic timescale for all models considered, so we can assume that the absorption of particles and observations of flux take place under conditions of thorough phase mixing, and we need deal only with the phase-averaged f anyway.

For a well-phase-mixed population of protons, we can calculate (for each choice of M, J, and Φ, or whatever set of coordinates we need) a fractional rate of absorption per unit time, *i.e.*, an inverse lifetime against satellite sweeping. We then seek solutions to equation 4.2 that are constant in time, *i.e.*, solutions to

$$\frac{1}{G}\nabla\cdot(G\mathbf{D}\cdot\nabla f) = \frac{f}{\tau_{ss}}. \tag{4.3}$$

The right-hand side of the equation is $-S$, which here includes no internal source of protons and losses due only to satellite absorption.

4.2. Losses

4.2.1. Satellites of Neptune

Paonessa and Cheng (1987) present a theory for calculation of the particle sweeping rate τ_{ss}^{-1} for a moon in a circular, equatorial orbit about a planet whose magnetic field has the form of a dipole offset from the planet's center and tilted with respect to its rotational axis (OTD); we largely follow their prescription, with modifications as noted. The six newly-discovered small satellites of Neptune have circular, prograde orbits near the planet, with inclinations of $< 1^{\circ}$ (except the innermost, 1989N6, at 5°) (Stone and Miner 1989); Triton's orbit is circular, inclined, and retrograde, and Nereid's is eccentric and inclined, but these moons do not enter the region of the magnetosphere where the protons in the CRS energy range were detected. The following discussion will focus on 1989N1, outermost of the newly-discovered satellites; as we will see, this is the only one that has a perceptible effect on our proton observations. The satellites are as described in table 4.1; a is the semimajor axis of the orbit.

Table 4.1 Satellites of Neptune

(after Stone and Miner (1989), Table 3)

Discovery Designation	Name	a (10^3 km)	a (R_N)	Period (hours)	Diameter (km)
1989N6	Naiad	48.0	1.94	7.1	54±16
1989N5	Thalassa	50.0	2.02	7.5	80±16
1989N3	Despina	52.5	2.12	8.0	180±20
1989N4	Galatea	62.0	2.50	10.3	150±30
1989N2	Larissa	73.6	2.97	13.3	190±20
1989N1	Proteus	117.6	4.75	26.9	400±20
--	Triton	364.8	14.33	141.0	2705±6
--	Nereid	5513.4	222.65	8643.1	340±50

In a magnetic field that is not a simple centered, aligned dipole, even a moon in a circular, equatorial orbit traces out a complicated motion in L and magnetic latitude and longitude (λ_m and ϕ_m). If the moon's orbit *is* circular and equatorial, however, the motion is periodic; figure 4.1 presents one orbital period of 1989N1 in magnetic coordinates L, λ_m, and ϕ_m for the I8E1 magnetic field model. Because the magnetic field corotates with the planet, the cyclic period is the moon's synodic period

$$T_m = \frac{2\pi}{|\Omega_K - \Omega_P|} \approx 40.2 \text{ hours.} \tag{4.4}$$

Figure 4.1

Magnetic coordinates for 1989N1 in the I8E1 field model for approximately one orbital period around Voyager 2's closest approach to Neptune (Selesnick 1991): (a) L, (b) latitude, and (c) longitude.

Figure 4.1

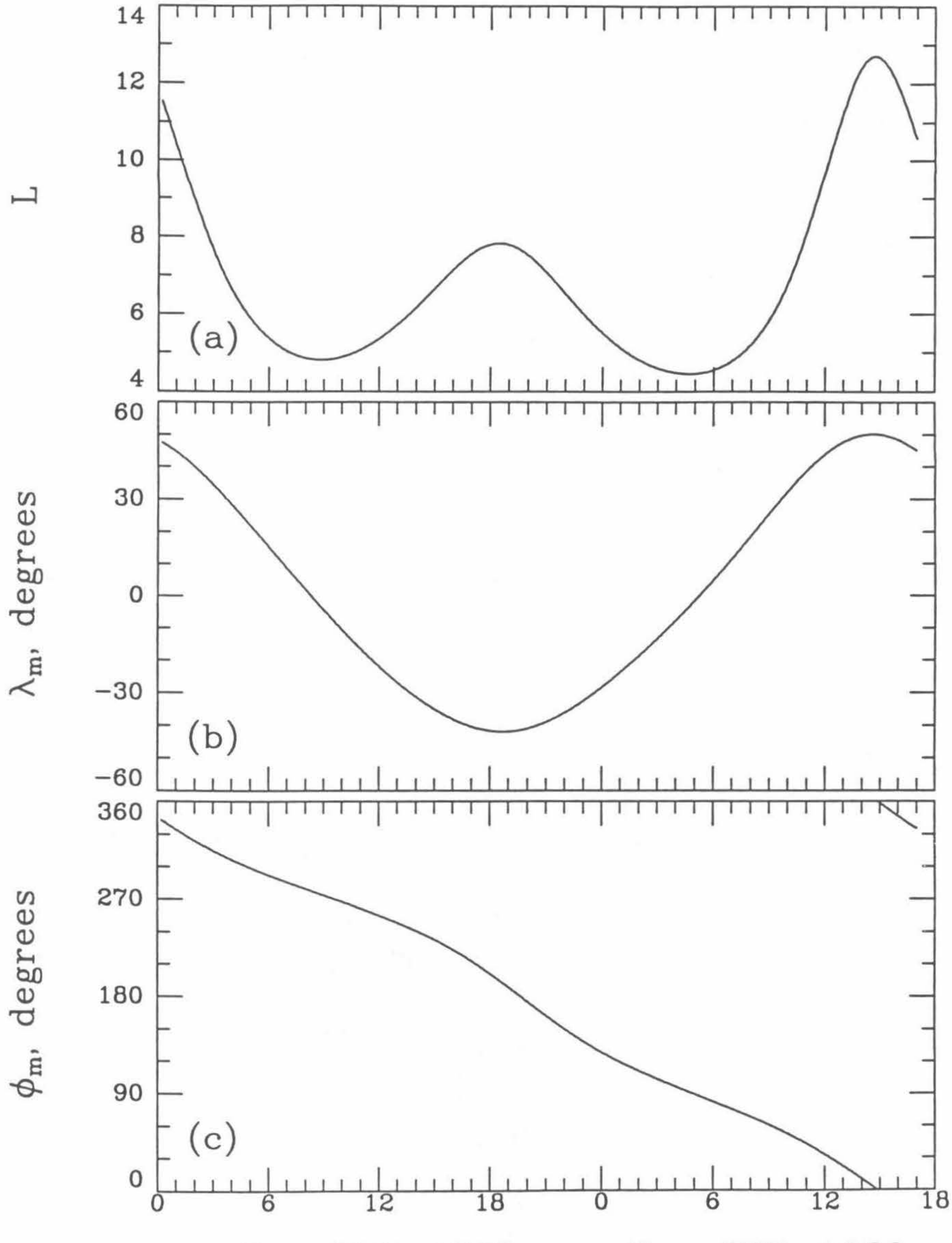
L
14
12
10
8
6
4
(a)
λm, degrees
60
30
0
−30
−60
(b)
φm, degrees
360
270
180
90
0
(c)
0
6
12
18
0
6
12
18
Day 236, 1989
Day 237, 1989

Ω_K is the Keplerian angular velocity of the moon in an inertial frame, positive for a prograde orbit, and Ω_P is the planet's (positive) rotational angular velocity.

4.2.2. Absorption Rate

4.2.2.1. Absorption by a Satellite in a Complex Magnetic Field

To calculate τ_{ss}^{-1}, consider a population of protons at given M, J, and Φ, or equivalently at given K, L, and M. As can be seen from figure 4.1(a), during a single synodic period particles at a given L can be absorbed during either two or four (depending on L) "sweeping episodes," when the moon is near that L. The particles drift in magnetic longitude at a bounce-averaged angular velocity ω_d as given in equation 3.10, which is positive for protons at Neptune (since the dipole moment of Neptune has a positive projection on the rotational axis, opposite to the situation at Earth). The moon has an angular velocity in magnetic longitude Ω_m, the time derivative of ϕ_m in figure 4.1(c), which is negative for a moon outside the radius for a synchronous orbit. Assuming particles are uniformly distributed around the L-shell, *i.e.*, assuming thorough drift-phase mixing, the probability that a particle will be absorbed during a single sweeping episode is

$$P_1 = \frac{\Delta t \, |\omega_d - \Omega_m|}{2\pi} P_a, \tag{4.5}$$

and if we consider the absorption to take place over the entire orbit rather than in two or four discrete episodes, then the average probability per unit time is

$$\tau_{ss}^{-1} = \frac{1}{T_m} \sum_{2\, or\, 4} P_1. \tag{4.6}$$

Δt is the duration of the sweeping episode, *i.e.*, the time during which the moon is in a position at which it can absorb particles of the specified L. The moon's effective radius for particle absorption, the distance from gyrocenter to moon center within which there is some chance for a particle to hit the moon's surface, is

$$r_m = R_m + \rho_g, \tag{4.7}$$

where R_m is the moon's physical radius and ρ_g is the local gyroradius. Thus Δt is the time during which the moon's center is within a distance r_m of the L-shell in question. We will divide the orbit into four "legs," each corresponding to a journey from one local extremum of L in figure 4.1 to the next; thus near an extremum the single sweeping episode will be divided between two legs. P_a is the probability that a particle which drifts past the moon during Δt actually hits it. P_a is not always unity, in fact for the particles considered in this work is often not even close to unity, for two reasons related to the large gyroradii of energetic protons in Neptune's middle magnetosphere. First, the larger the gyroradius the smaller the separation of the three timescales of particle motion, so that in the time it takes a particle to bounce from the moon's magnetic latitude λ_m to a mirror point λ_{mirr} and back again, it can drift so far in magnetic longitude that its guiding center will move from more than r_m "upstream" to more than r_m "downstream" of the moon, *i.e.*, it will not come close enough to the moon to be absorbed (the "leapfrog effect"). Second, when ρ_g is not small relative to R_m, the moon can actually fit within the empty spaces in the (locally) helical trajectory of a particle, and thus the particle can move past the moon even if its guiding center passes within r_m of the moon's center (the "corkscrew effect").

Paonessa and Cheng (1985) calculate P_a and thence τ_{ss}^{-1} for an aligned, centered dipole magnetic field, and Paonessa and Cheng (1987) generalize the calculation to an offset, tilted dipole with offset in the $\hat{z}$ direction only, *i.e.*, parallel to the planet's rotation axis (ZOTD), which is a good approximation at Uranus. The latter generalization is further generalized here by finding quantities like λ_m, Ω_m, and (indirectly) Δt numerically from the orbit in figure 4.1 rather than from closed-form expressions; we still use dipolar-field values for such quantities as ω_d and λ_{mirr}, transforming K, L, and M into these quantities as for a dipole field of moment

$$k_0 = 0.130 \text{ Gauss} \times R_N^3 \tag{4.8}$$

(from the second preliminary field model (OTD2) for Neptune (Ness 1990)).

4.2.2.2. Duration of A Sweeping Episode

Except near the extrema in L of the orbit, where dL/dt approaches zero, we can read λ_m and dL/dt for the moon at each L from figure 4.1, calculate r_m given L, λ_m, and the particle's K and M, and write

$$\Delta t = \frac{2\Delta L}{\left|\frac{dL}{dt}\right|} \tag{4.9}$$

for

$$\Delta L = \frac{r_m}{R_N} \frac{\sqrt{1 + 4\tan^2\lambda_m}}{\cos^2\lambda_m}. \tag{4.10}$$

The trigonometric terms in equation 4.10 were introduced by Selesnick and Stone (1991a) to account for the fact that away from the magnetic equator the moon covers a larger range in L as the field lines (and L-shells) bunch together near the poles. Near the extrema in L, where equation 4.9 breaks down, Paonessa and Cheng (1987) took advantage of the small electron gyroradius and therefore small ΔL to use a constant value for Δt within ΔL of L_{min}; Cooper (1990) and Selesnick and Stone (1991a) gave a more exact variable expression inside $L = 1.01\ L_{\text{min}}$, but still one that uses the ZOTD formulae for the moon's magnetic coordinates. These papers only consider the minimum L of the moon (there is only one for a ZOTD model), where most electron absorption occurs, but for energetic protons absorption around the secondary maximum L ($L_{\text{max}} \approx 7.8$) is actually more important, as we will see. We approximate the extrema of figure 4.1(a) by parabolae, *i.e.*, make L a quadratic function of time with second derivative equal to that of the orbit in figure 4.1(a) at the extremum, and can then write a closed expression for Δt. At a minimum in L,

$$\Delta t = \left[\frac{2(L - L_{\text{min}} + \Delta L)}{\left|\frac{d^2L}{dt^2}\right|} \right]^{1/2} \tag{4.11}$$

for $L_{\text{min}} - \Delta L \leq L \leq L_{\text{min}} + \Delta L$, and

$$\Delta t = \left[\frac{2(L - L_{\text{min}} + \Delta L)}{\left|\frac{d^2L}{dt^2}\right|} \right]^{1/2} - \left[\frac{2(L - L_{\text{min}} - \Delta L)}{\left|\frac{d^2L}{dt^2}\right|} \right]^{1/2} \tag{4.12}$$

for $L_{\min} + \Delta L \leq L \leq L_{\min} + 2\Delta L$. At a maximum in L,

$$\Delta t = \left[\frac{2(L - L_{\max} - \Delta L)}{\left| \frac{d^2L}{dt^2} \right|} \right]^{½} \tag{4.13}$$

for $L_{\max} + \Delta L \geq L \geq L_{\max} - \Delta L$, and

$$\Delta t = \left[\frac{2(L - L_{\max} - \Delta L)}{\left| \frac{d^2L}{dt^2} \right|} \right]^{½} - \left[\frac{2(L - L_{\max} + \Delta L)}{\left| \frac{d^2L}{dt^2} \right|} \right]^{½} \tag{4.14}$$

for $L_{\max} - \Delta L \geq L \geq L_{\max} - 2\Delta L$. The large proton gyroradius means that we must use these expressions over a much larger region in L than is necessary for electrons before we can go back to equation 4.9; on the other hand, the parabolic approximation to the orbit deteriorates away from the extremum. The choice made, *i.e.*, to go a distance $2\Delta L$ from the extremum (rather than $0.01L_{\min}$, as did Cooper (1990) and Selesnick and Stone (1991a)), works well at $L_{\max} \approx 7.8$ (we have no proton data in the energy range considered beyond $L \approx 10$, so we need not calculate τ_{ss}^{-1} near $L_{\max} \approx 12.7$), but some discontinuity at the changeover is evident near the two $L_{\min}$s. However, as we will see, errors in the region inside of $L \approx 6$ have little effect on our simulated data for the range of models considered. Figures 4.4(a), 4.5(a), and 4.6(a) present Δt as a function of L for three pairs of K, M; the dotted lines are the contributions for the four legs of the orbit, and the solid line is the sum. Each leg's contribution is cut off at the L at which the particle mirrors below the moon's λ_m. If these were electrons, for which P_a is very nearly unity, τ_{ss}^{-1} would be roughly proportional to this L-shell contact time (only the variation in ω_d in equation 4.5, approximately as $L^{-½}$ for relativistic particles (as L^{-2} for non-relativistic) at constant K and M, would change the proportionality); the effect of variable P_a for protons can be seen by comparing these figures with figures 4.6(b), 4.5(b), and 4.6(b). Figures 4.4 and 4.6 are near the limits of K that we need to calculate to model our observations; figure 4.5 is at an intermediate K with the worst mismatch seen between equations 4.9 and 4.12, resulting in the discontinuities (up to about 30%) in Δt at the Ls indicated by the short vertical lines in figure 4.5(a).

4.2.2.3. "Leapfrog" and "Corkscrew" Effects

The last step remaining is to calculate P_a, the fraction of particles encountering a moon during a sweeping episode that are actually absorbed by it. Consider the set of particles at the K, L, and M of interest whose guiding centers will enter the zone of radius r_m about the moon's center in the next bounce period τ_b; in a plane perpendicular to the magnetic field at the λ_m of the moon, these will form a band as shown in figure 4.2(a) (the area labeled A, which does not include the crosshatched area within r_m of the moon), where

$$y_{dt} = \phi_{dt} LR_N \cos^3\lambda_m \equiv \tau_b \, |\omega_d - \Omega_m| LR_N \cos^3\lambda_m \tag{4.15}$$

is the drift distance relative to the moon in time τ_b. During each interval of τ_b in Δt, another patch like this will drift by the moon; thus it suffices to calculate the P_a for one patch. (By calculating absorption probabilities for particles with gyrocenters at different positions and the moon's center fixed at the L of interest, rather than placing the moon's center at all the different Ls it will occupy during a sweeping episode for particles at a fixed L, we are ignoring variations in ρ_g, λ_m for the moon, and other relevant quantities on a scale of ΔL.) P_a will be the average over area A of the probability P_i that a particle first crossing the plane in figure 4.2(a) at a point i will actually be absorbed by the moon. Assuming an equal number of particles moving up the field line and down it, we must average the probability P_i calculated for both directions of travel. Particle paths are shown schematically in figure 4.2(b); thus we move the particle rightward in figure 4.2(a) in alternating short and long steps of length

$$y_{da} = \phi_{da} LR_N \cos^3\lambda_m \tag{4.16}$$

and

$$y_{db} = \phi_{db} LR_N \cos^3\lambda_m , \tag{4.17}$$

and averaging over travel directions amounts to averaging over P_i as calculated with the short hop first and with the long hop first. Paonessa and Cheng (1987) approximate ϕ_{da} and ϕ_{db} by assuming the drift rate in longitude is constant with latitude, so

$$\phi_{db} = |\omega_d - \Omega_m| \left[\frac{\tau_b}{2} + 2 \int_0^{|\lambda_m|} \frac{dl}{v_{||}} \right]$$

$$= |\omega_d - \Omega_m| \left[\frac{\tau_b}{2} + \frac{8R_N L}{\beta c} \int_0^{|\lambda_m|} \frac{\cos\lambda\sqrt{1 + 3\sin^2\lambda}}{(1 - B(\lambda)/B(\lambda_{mirr}))^{1/2}} d\lambda \right], \tag{4.18}$$

where the integral is a partial integral of $H(\lambda_{mirr})$ as defined in equation 3.8; ϕ_{da} is the difference between ϕ_{dt} and ϕ_{db}. Actually, it is not calculationally necessary to average over the entire area A, nor over both directions, as can be seen from figure 4.3, which shows several cases of relative sizes among y_{da}, y_{db}, and $2r_m$. In each case, only particles that start out in the letter-labeled areas upstream of the crosshatched zone near the moon will actually enter the zone and encounter the moon. For the case in figure 4.3(a) with $2r_m < y_{da} < y_{db}$, particles whose guiding centers start in areas A or B will encounter the moon once, with equal P_i at corresponding points whether B is y_{da} downstream from A as shown or y_{db} downstream. Figures 4.3(b) and 4.3(c) show the case $y_{da} < 2r_m < y_{db}$, with the two choices of which step to take first: the areas labeled the same in each of these two figures have identical histories, *i.e.*, they first enter the crosshatched zone at the same place and after the same size step, and thus have the same P_i at corresponding points. The same holds in figures 4.3(d) and 4.3(e), which show the case $y_{da} < y_{db} < 2r_m$. Thus we do not have do the full averaging discussed above: it suffices to set $P_i = 0$ in the unlabeled areas shown (the larger these areas are, the greater the magnitude of the leapfrog effect) and to choose, say, the short step to be taken first.

At each point i, we move the guiding center rightward by alternating-size steps until it comes within $2r_m$ of the moon's center; at this point we calculate the probability α_g that it will hit the moon *on that bounce* through the moon's λ_m, which is a function of the impact parameter s by which the guiding center trajectory misses the moon's center. If the next step does not take the particle out of the crosshatched zone, as will be the case for area B in figures 4.3(b) and 4.3(c) and for most of areas A and B in figures 4.3(d) and 4.3(e), we calculate α_g for the new guiding center position, and so on, building up the product

$$1 - P_i = \prod_j [1 - \alpha_g(s_j)]. \tag{4.19}$$

There may be only one term in the product, for a point in areas A or C of figure 4.3(b), say. Paonessa and Cheng (1985) follow individual particle trajectories to calculate α_g numerically;

Figure 4.2(a)

Area "upstream" of moon, over which P_i is to be integrated, after Paonessa and Cheng (1987), figure 2(b). Particle drift motion is to the right.

Figure 4.2(b)

Geometry for modeling absorption probability during a single drift encounter of particles with a moon, after Paonessa and Cheng (1987), figure 2(a). Dashed line indicates magnetic latitude of moon.

Figure 4.2(a)

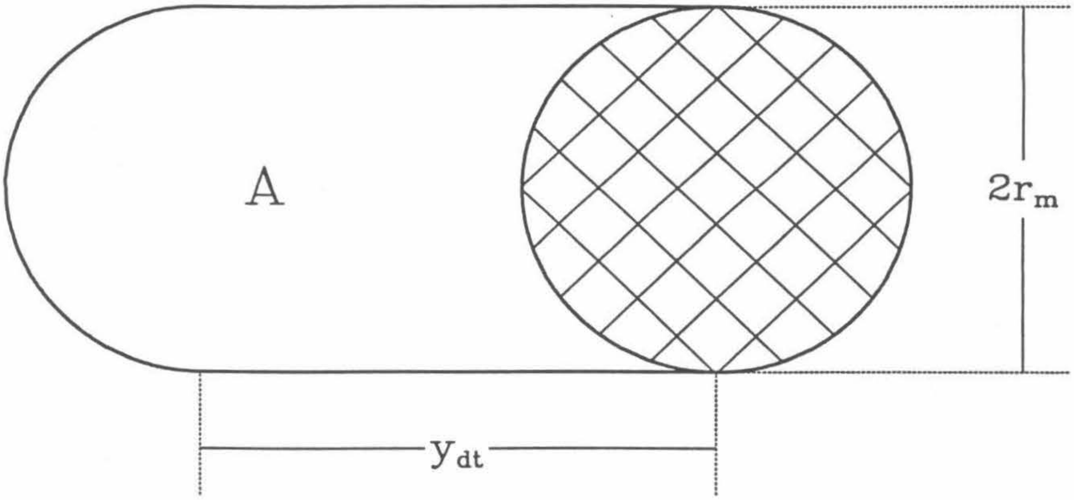

Figure 4.2(b)

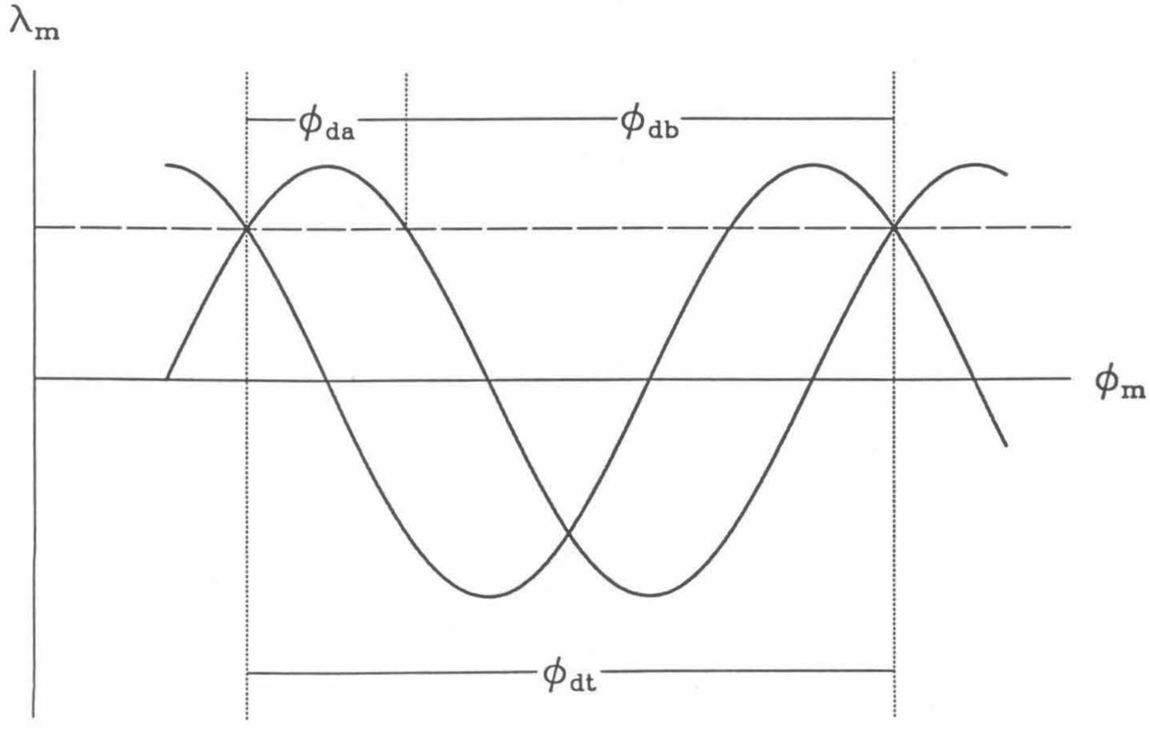

Figure 4.3

Various cases of "leapfrog" effect: (a) $2r_m < y_{da} < y_{db}$; (b) $y_{da} < 2r_m < y_{db}$, long hop first; (c) $y_{da} < 2r_m < y_{db}$, short hop first; (d) $y_{da} < y_{db} < 2r_m$, long hop first; (e) $y_{da} < y_{db} < 2r_m$, short hop first.

Figure 4.3

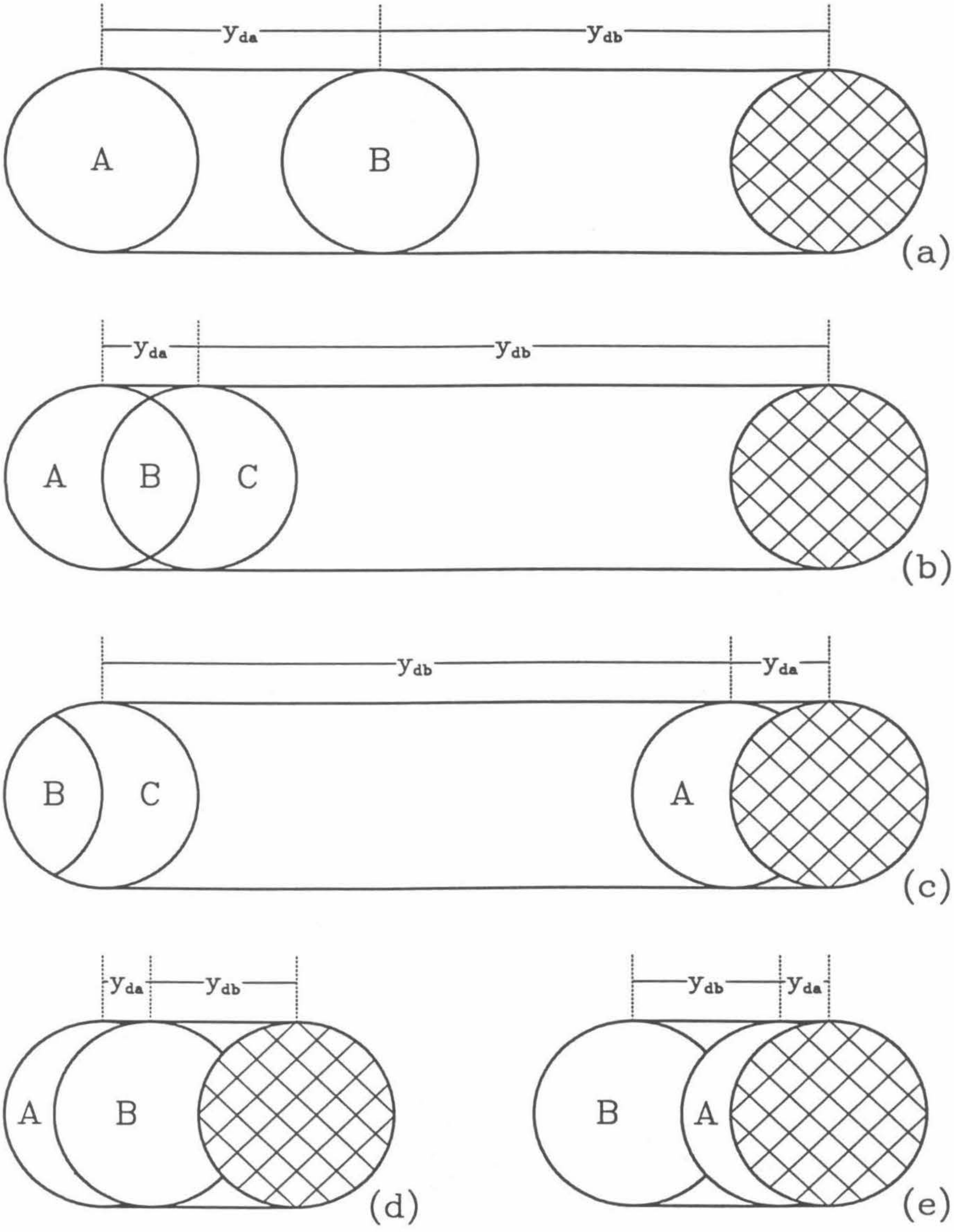

a set of closed formulae for this quantity are derived in appendix 1. (A large corkscrew effect results in a reduced α_g and P_i.)

4.2.2.4. Results for τ_{ss}^{-1}

Some results of the above calculation of τ_{ss}^{-1} are shown in figures 4.4(b), 4.5(b), 4.6(b), with contributions from each of the four legs of the orbit again shown as dotted lines. In contrast to Δt for the same Ks and Ms, as in figures 4.4(a), 4.5(a), and 4.6(a), τ_{ss}^{-1} is strongly peaked around the high-L end of each of the dotted curves; this is because the protons there are being absorbed near their mirror points, and the increasingly flat spiral at the high local pitch angle reduces the corkscrew effect. Some additional irregularities are visible in the vicinity of the changeover from equation 4.9 to 4.12 or 4.14: the two legs meeting there suddenly start to diverge. This is because λ_m is read at the moon's extremal value of L from figure 4.1 for use in equations 4.12 and 4.14, while it is calculated from the particle's K and L for use in equation 4.9; this can produce a noticeable difference in P_a. Like the mismatch in Δt, this has the biggest effect at low Ls, and thus little effect on simulated data for the models considered.

For comparison, figures 4.4(c), 4.5(c), and 4.6(c) show τ_{ss}^{-1} for electrons (calculated assuming $P_a \equiv 1$) at the same values of K and M. The absorption is much more sharply peaked at the extremal values of L for the moon, since the electrons' gyroradius is so much smaller than the protons', so that the region of high Δt does not extend to Ls much away from the extremal value at the turnaround; also, the constancy of P_a removes the high-L enhancement apparent in the proton curves. Δt is actually about tenfold less for electrons than for the corresponding protons due to the reduced r_m, and at the same K, L, and M, ω_d in equation 4.5 scales inversely as the relativistic factor γ and does not depend separately on particle mass; thus if P_a were the same for protons as for electrons, τ_{ss}^{-1} would be more than an order of magnitude larger for protons than for electrons. The importance of the leapfrog and corkscrew effects for protons is seen in that it is actually less.

4.2.2.5. Contributions To τ_{ss}^{-1} Not Included

Several modifications to the above method were considered but not used, as in all cases the resulting changes in τ_{ss}^{-1} either were concentrated in the region $L < 5$, and thus there would be little or no alteration to the data simulated in the range of models considered, or were tried out in simulations and found directly to have little effect, or both. First, the smoothing implicit in the use of figure 4.2(a) and parenthetically noted near that figure is generally better for particles absorbed away from the magnetic equator, *i.e.*, at higher Ls; and in particular, the method described above would give $\tau_{ss}^{-1} = 0$ for equatorial particles. A more exact calculation of τ_{ss}^{-1} is possible for these particles, and is given in appendix 2; a comparison of figure 4.4(b) with figure A2.2(c) is most direct, as the particles in these two figures are at the same M. The peaks in figures A2.2 are due to enhanced absorption when the moon is near x_1 or x_2 in figure A2.1; the averaging implicit in the above discussion would suppress these, even if Δt weren't assumed to vanish because the moon center is above $\lambda_m = 0$ for all but an instant. This approximation would be calculationally difficult to remove, and as noted it is suspect mostly in a region with little effect on simulated data.

An approximation that *could* be removed easily is that made by Paonessa and Cheng (1987) in calculating ϕ_{db} (equation 4.18). Rather than assuming an angular drift rate constant in λ_m, we can write the drift longitude directly as a partial integral of $F(\lambda_{mirr})$ as defined in equation 3.11. Another approximation is that in the calculation of $\alpha_g(s)$ the particle was assumed to be bouncing along the field line. This means that the guiding center motion on each pass through the plane of figure 4.2(a) is perpendicular to that plane. But if bounce and drift timescales are not well separated, as would cause a significant leapfrog effect, then the motion will be more like that diagrammed in figure 4.2(b) (which was meant to be schematic), *i.e.*, the crossing of the moon's λ_m might take place at a significant angle to the vertical. This would be a stronger effect for particles absorbed nearer the equator, *i.e.*, at low Ls; the stronger field at high λ_m reduces ρ_g and separates the local timescales, so that the sinusoids in figure 4.2(b) should actually be sharply cusped near the mirror points. Still, an improvement on the approximation can be made by reducing s, the impact parameter of the guiding center trajectory past the moon's center, by an amount derived geometrically by angling the trajectory by the appropriate amount relative to the perpendicular at each point in

Figure 4.4

(a) 1989N1 proton sweeping episode duration, (b) proton absorption rate, and (c) electron absorption rate for $K = 10^{-2.25}\ R_N\sqrt{\mathrm{G}}$, $M = 10^{4.4}$ MeV/G.

Figure 4.5

Same as figure 4.4, for $K = 10^{-1}\ R_N\sqrt{\mathrm{G}}$, $M = 10^{4.2}$ MeV/G; in figure 4.5(a), L values at changeover from equation 4.9 to equation 4.12 for each leg of the moon's orbit are indicated by short vertical lines.

Figure 4.6

Same as figures 4.4 and 4.5, for $K = 10^{-0.25}\ R_N\sqrt{\mathrm{G}}$, $M = 10^{3.3}$ MeV/G; each short vertical line in figure 4.6(a) indicates changeover L as in figure 4.5(a) for one pair of legs.

Figure 4.4

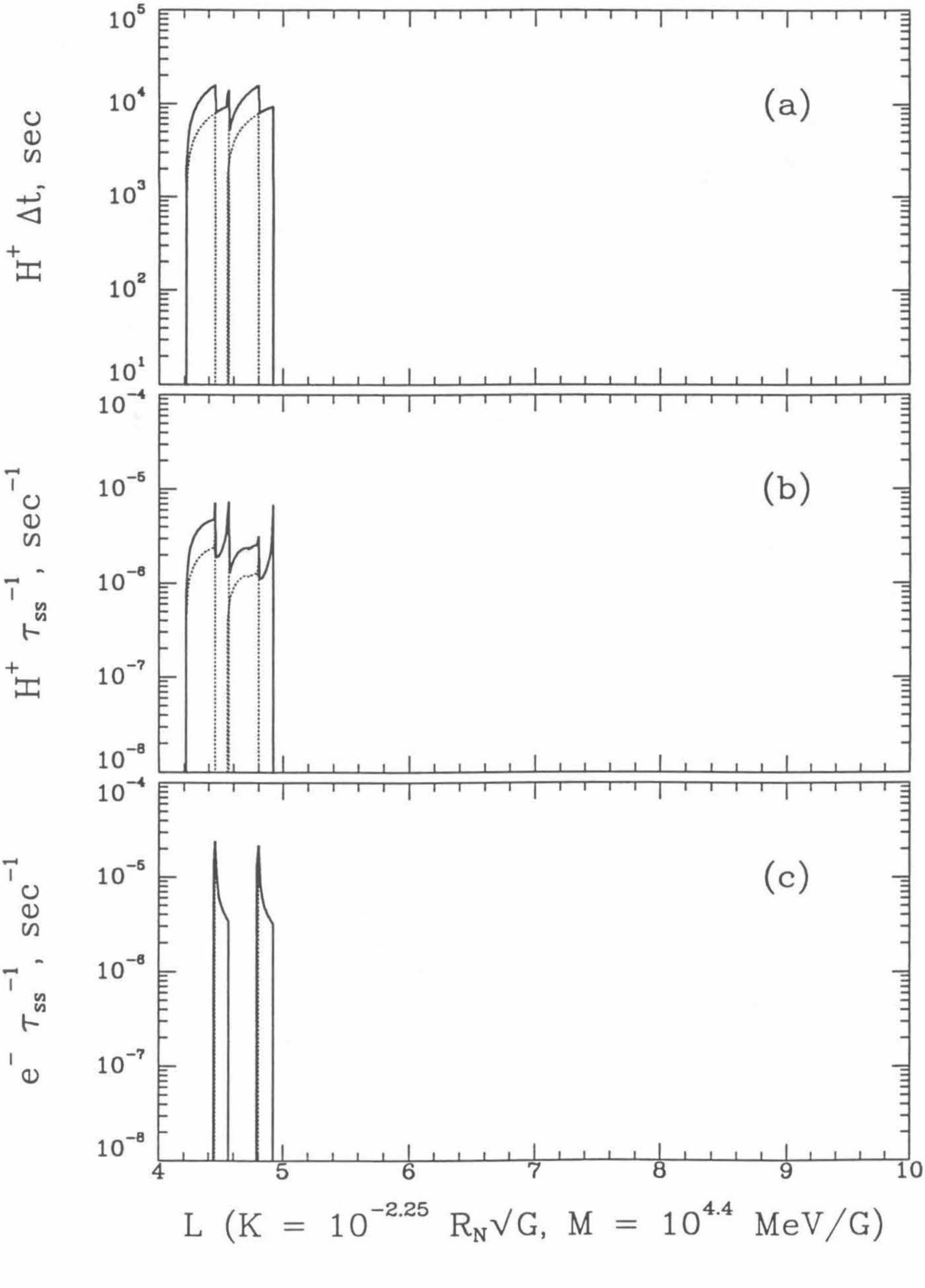
10^5
10^4
10^3
10^2
10^1
(a)
H^+ Δt, sec
10^{-4}
10^{-5}
10^{-6}
10^{-7}
10^{-8}
(b)
H^+ τ_{ss}^{-1}, sec^{-1}
10^{-4}
10^{-5}
10^{-6}
10^{-7}
10^{-8}
(c)
e^- τ_{ss}^{-1}, sec^{-1}
4
5
6
7
8
9
10
L ($K = 10^{-2.25}$ $R_N\sqrt{G}$, $M = 10^{4.4}$ MeV/G)

Figure 4.5

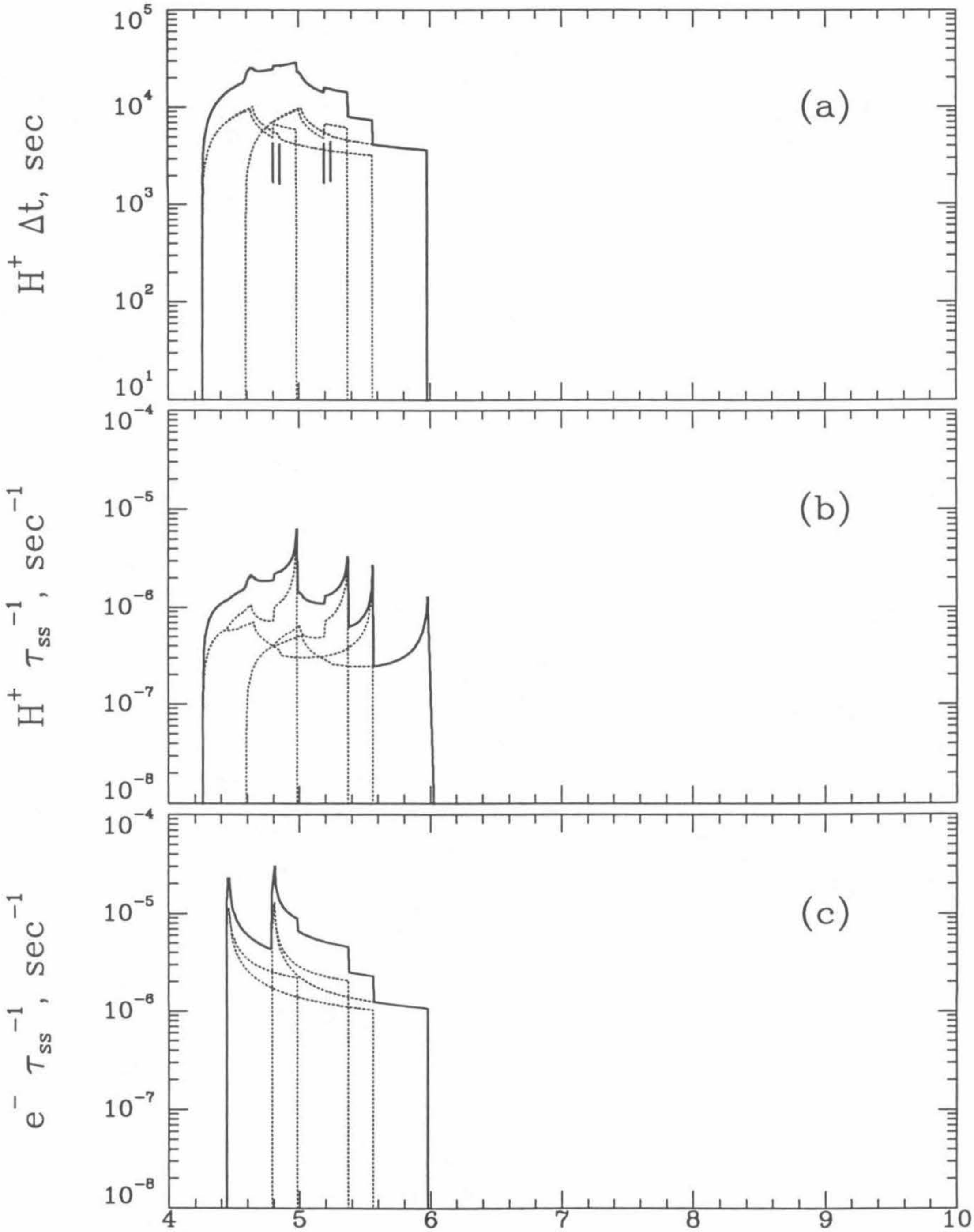
(a)
(b)
(c)
H^+ Δt, sec
H^+ τ_{ss}^{-1}, sec^{-1}
e^- τ_{ss}^{-1}, sec^{-1}
10^5
10^4
10^3
10^2
10^1
10^{-4}
10^{-5}
10^{-6}
10^{-7}
10^{-8}
4
5
6
7
8
9
10
L (K = 10^{-1} $R_N\sqrt{G}$, M = $10^{4.2}$ MeV/G)

Figure 4.6

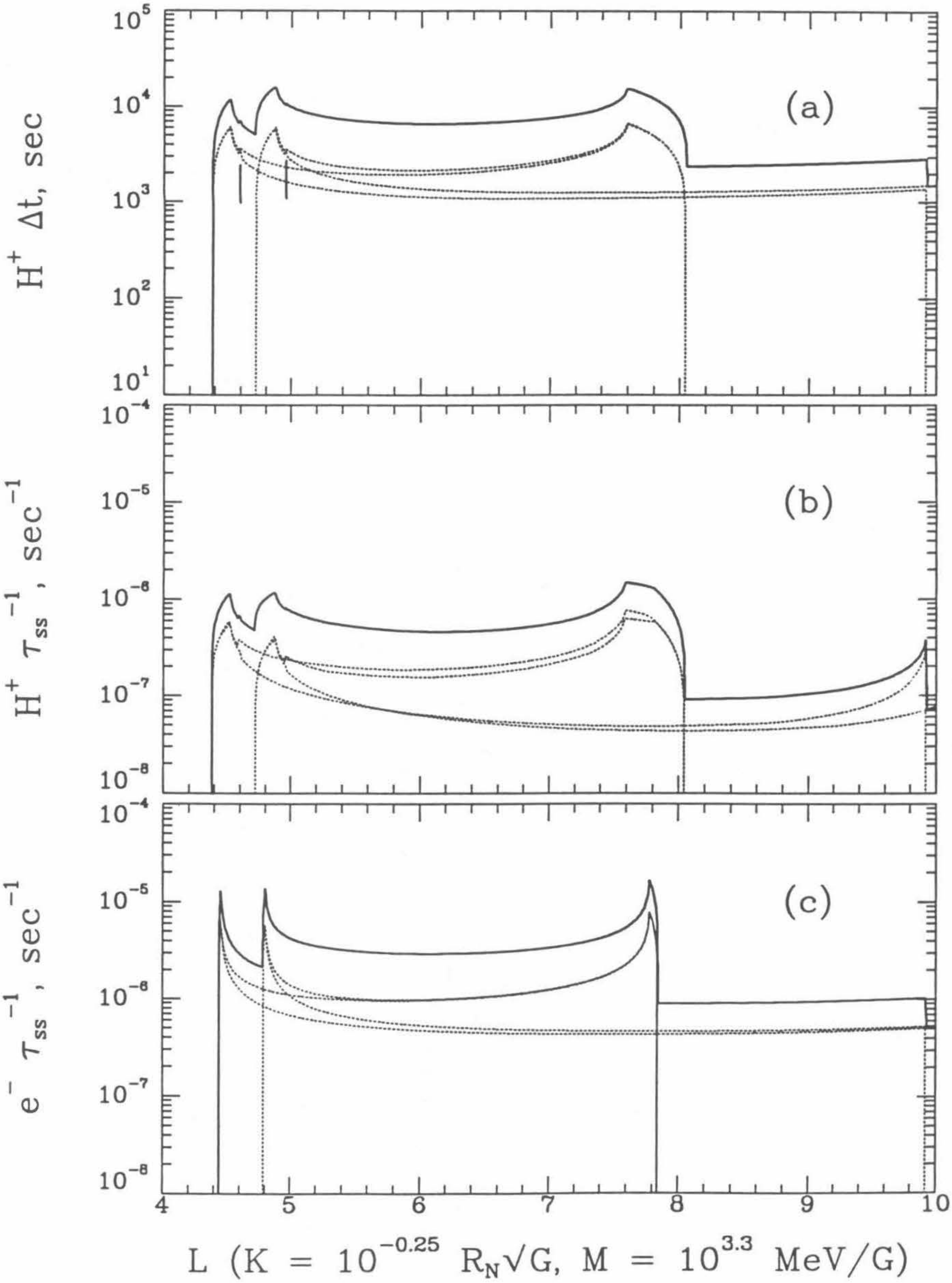
H^+ Δt, sec
10^5
10^4
10^3
10^2
10^1
(a)
H^+ τ_{ss}^{-1}, sec^{-1}
10^{-4}
10^{-5}
10^{-6}
10^{-7}
10^{-8}
(b)
e^- τ_{ss}^{-1}, sec^{-1}
10^{-4}
10^{-5}
10^{-6}
10^{-7}
10^{-8}
(c)
4
5
6
7
8
9
10
L (K = $10^{-0.25}$ $R_N\sqrt{G}$, M = $10^{3.3}$ MeV/G)

the crosshatched area in figure 4.2(a); this would keep the *particle's* trajectory as a helix with axis along the guiding center trajectory, rather than reproducing the more complicated path actually followed, but still it should give an idea of the magnitude of the effect (in addition to allowing us to continue to use the formulae of appendix 1). Both changes noted here were made; the difference in τ_{ss}^{-1} was at most a few percent in the region beyond $L \approx 5$, and the data simulated were not noticeably different; thus the approximations from Paonessa and Cheng (1987) as detailed above were retained.

Another modification would be to add the other five small inner moons listed in table 4.1. The result is shown in figure 4.7 for the Ks and Ms corresponding to figures 4.4, 4.5, and 4.6. Even for the highest K, the moons inward of 1989N1 are just beginning to absorb outside $L \approx 5$, contributing a small amount over the absorption due to 1989N1 alone; at the two lower Ks, the highest L swept by the inner moons is less than the lowest swept by 1989N1. The absorption, of course, extends farther inward in L than for 1989N1 alone. A model calculation of simulated data was made using all six moons; again, no noticeable change from that found using only 1989N1 was seen. There are also four rings about Neptune, from approximately the orbit of 1989N4 inward; Paranicas and Cheng (1991) present a theory for calculation of the particle sweeping rate due to planetary rings. They find that ring absorption can exceed moon absorption in the region where it is effective; but again, this is too far inward in L to have an effect on the data simulated from the range of models considered here. Thus we consider only absorption due to 1989N1 hereinafter.

Figure 4.7

Proton absorption rates for all six inner small moons for (a) $K = 10^{-2.25}\ R_N\sqrt{\mathrm{G}}$, $M = 10^{4.4}$ MeV/G, (b) $K = 10^{-1}\ R_N\sqrt{\mathrm{G}}$, $M = 10^{4.2}$ MeV/G, and (c) $K = 10^{-0.25}\ R_N\sqrt{\mathrm{G}}$, $M = 10^{3.3}$ MeV/G; solid line is 1989N1, dotted lines are other moons, heavy solid line is sum. 1989N1 is distinguishable from the sum only in figure 4.7(c); in the other two figures, its absorption is disjoint in L from that of the other moons.

Figure 4.7

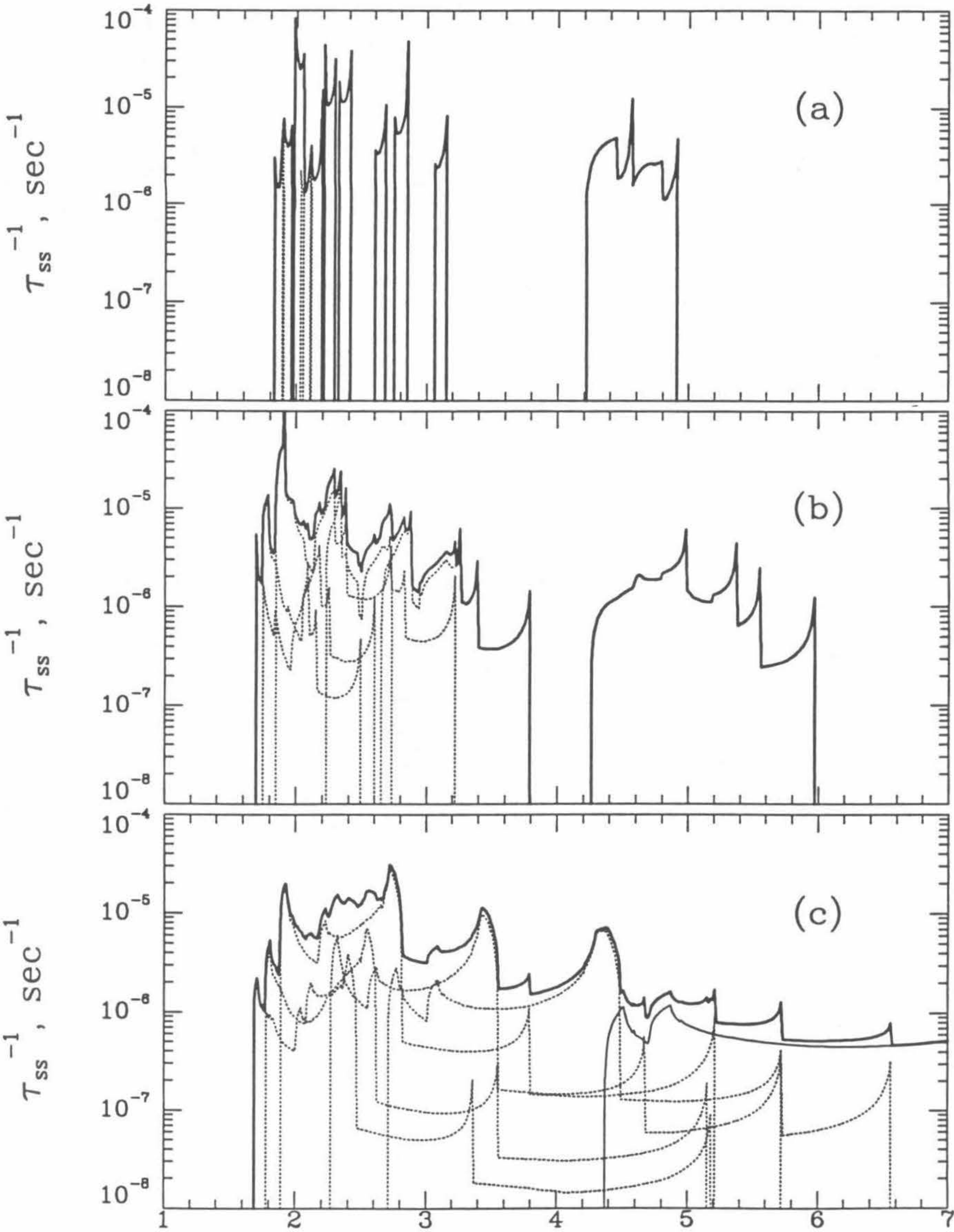

Chapter 5

Models of the Energetic Proton Distribution

5.1. Radial-Diffusion Models

5.1.1. Theory

A charged particle trapped in a static near-dipolar magnetic field will execute a motion determined by the values of the three adiabatic invariants, as described in chapter 3. If a variable electromagnetic field is present that changes on a timescale rapid enough to break down the "adiabatic" assumptions used to derive these invariants, these values may be changed. Since the variable fields will distinguish among particles with the same values of the invariants but with different phases of one or more of the periodic motions (*e.g.*, geomagnetic sudden impulses will not distinguish among particles with different cyclotron or bounce phases, but will affect particles with different drift phases differently), phase-mixing of the affected particles will randomize the effects of the variations and cause the changes in the value(s) of the invariant(s) to be diffusive, describable by equation 4.2 (Schulz and Lanzerotti 1974).

The nature of the perturbing field(s) will determine which of the invariants cease(s) to be invariant; some mechanisms for diffusion will be discussed in chapter 6. The longest of the three time scales of periodic motion discussed in chapter 3 is the drift time τ_d; thus perturbations occurring on a characteristic timescale comparable to or somewhat shorter than τ_d (but longer than τ_b or τ_g) can be expected to violate the invariance of J_3 (or Φ or L). This one-dimensional variation is referred to as radial diffusion. Let us label particles by M, K, and L; for radial diffusion, M and K remain invariant, while L varies. Then the Jacobian G in equation 4.3 is proportional to L^{-2} (Haerendel 1968), the diffusion tensor D has only the one component D_{LL}, and the diffusion equation becomes

$$L^2 \frac{d}{dL}\left[\frac{D_{LL}}{L^2}\frac{df}{dL}\right] = \frac{f}{\tau_{ss}}, \tag{5.1}$$

which is to be solved for f as a function of L at each pair of K and M.

5.1.2. Fits

5.1.2.1. Boundary Conditions

Equation 5.1, a second-order differential equation, requires two boundary conditions to define a solution; we choose to put one at each end of the interval of interest in L. For an inner boundary condition, we note (from the L *vs.* time relation in figure 3.2(a) and the proton flux as a function of time in figures 2.9, 2.10, 2.11, and 2.12) that there was no significant proton flux seen at L much less than 6, so we set $f = 0$ at $L = 3$ (which is far enough inward that we should see any model-dependent effects around the minimum L of 1989N1--as will be seen, the flux vanishes even farther out than this for all models considered). For an outer boundary condition, we specify a spectrum in M and K at $L = 10$ (outside of which the observed proton flux is again negligible, so the phase-space density will not be constrained by data). It is convenient to assume a pitch-angle distribution of form

$$j = p^2 f \propto \sin^{2n}\alpha_0 = \left[\frac{B(\lambda)}{B_0}\right]^n \sin^{2n}\alpha, \tag{5.2}$$

where the last equality follows from equation 3.7, and which implies that the power law form in $\sin^2\alpha$ is the same at all magnetic latitudes along the field line, with only the normalization varying. Leaving n free as a fit parameter, it suffices to define the spectrum $f_F(M)$, or equivalently $j_F(E)$, at one particular fiducial K_F (and $L = 10$). Then we find f at other Ks by matching M at the K of interest with that M_F which at K_F has the same value of E (whence p^2 in equation 5.2), and setting the ratio of f to $f_F(M_F)$ in accordance with equation 5.2 using the equatorial pitch angles α_0 corresponding to K and K_F. We choose $K_F = 0.3\,R_N\sqrt{\text{G}}$, which is close to the values observed by LET C at most of the points chosen for fitting on the outbound leg of the trajectory (see figure 3.2(b)).

To set $f_F(M)$, we assume that the modifications to the boundary spectrum as it diffuses inward and suffers absorption are reasonably smooth as a function of K, L, and M. Then we can treat each two-volume, two- or three-point doubles or triples spectrum as a segment from the boundary spectrum at the K observed, preserving the spectral slope though reduced in magnitude. Further, if n in equation 5.2 is not a function of M (or E) we can consider that segment to be itself a segment from f_F, at a different M_F and magnitude but again preserving the spectral slope. Thus, finally, we can shift each segment to its points' M_Fs, then attempt to splice the segments together (by shifting each one's magnitude, both or all three of its points by the same amount) into a single spectrum. This will give us the *shape* of the overall spectrum; the normalization can be left to float as another fit parameter, or set to have the flux calculated from f_F agree with that observed near $L = 10$.

Figures 5.1 show the phase-space densities calculated from the observed proton flux points (for those selected out in chapter 3 to be fit), each plotted at its M_F; figures 5.2 show the results of the shifting process described above. As seen in the latter figures, we can move all the segments to lie close to a single spectrum (with some outliers), which is shown in each of the figures as a solid line. The shifting was done by eye, as was the drawing of the adopted $f_F(M_F)$, which has breakpoints at 1600 and 2200 MeV/G, with power law indices of -3, -7, and -10 in M (the indices of $j(E)$ in E are -2, -6, and -9). Normalization is chosen to reproduce the fluxes seen by LET C (at about K_F) at the highest Ls in the outbound leg of the trajectory (in which region absorption has reduced phase-space densities but little from the values at $L = 10$).

5.1.2.2. Results

We now seek a prescription for D_{LL} such that f derived by solution of equation 5.1 reproduces the observed proton fluxes as well as possible; we also find the best value of n in equation 5.2. Equation 5.1 is solved by converting it to a finite difference equation on a grid spacing of 0.01 units in L, which is solved with a sparse matrix inversion algorithm (SOLVDE) from Press *et al.* (1988) as specialized to the linear case by Selesnick. A maximum-likelihood fit was done, but using

Figure 5.1

Proton phase-space densities as observed, plotted at M_F as calculated for each point: (a) LET C inbound, (b) LET C outbound, (c) LET D inbound, (d) LET D outbound. Solid line in each graph is the boundary-condition spectrum f_F as described in the text.

Figure 5.2

Observed proton phase-space densities shifted to line up in one spectrum, plotted at M_F as calculated for each point: (a) LET C inbound, (b) LET C outbound, (c) LET D inbound, (d) LET D outbound. Solid line in each graph is the boundary-condition spectrum f_F as described in the text.

Figure 5.1

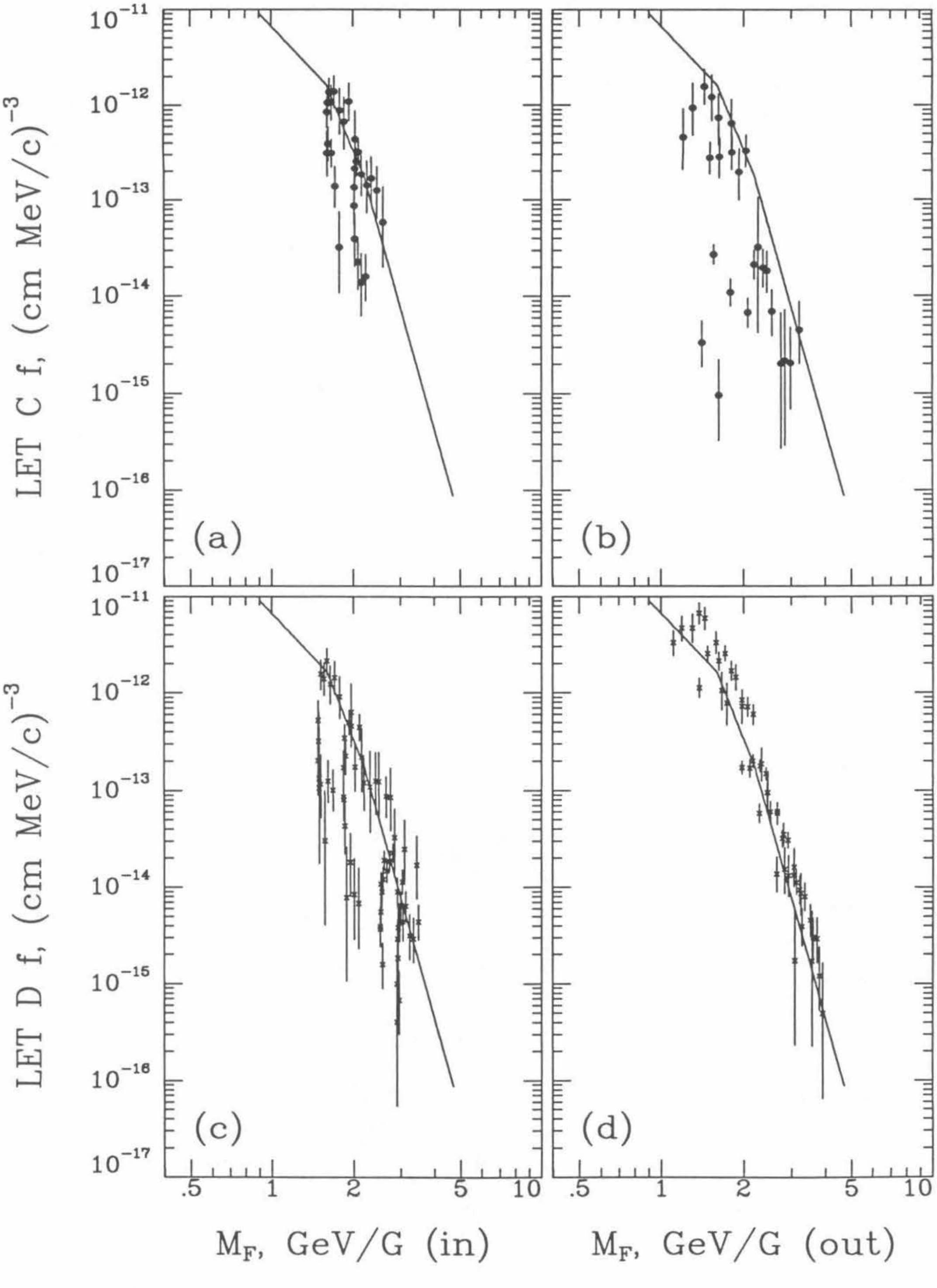
LET C f, (cm MeV/c)$^{-3}$
LET D f, (cm MeV/c)$^{-3}$
10^{-11}
10^{-12}
10^{-13}
10^{-14}
10^{-15}
10^{-16}
10^{-17}
(a)
(b)
(c)
(d)
.5
1
2
5
10
M_F, GeV/G (in)
M_F, GeV/G (out)

Figure 5.2

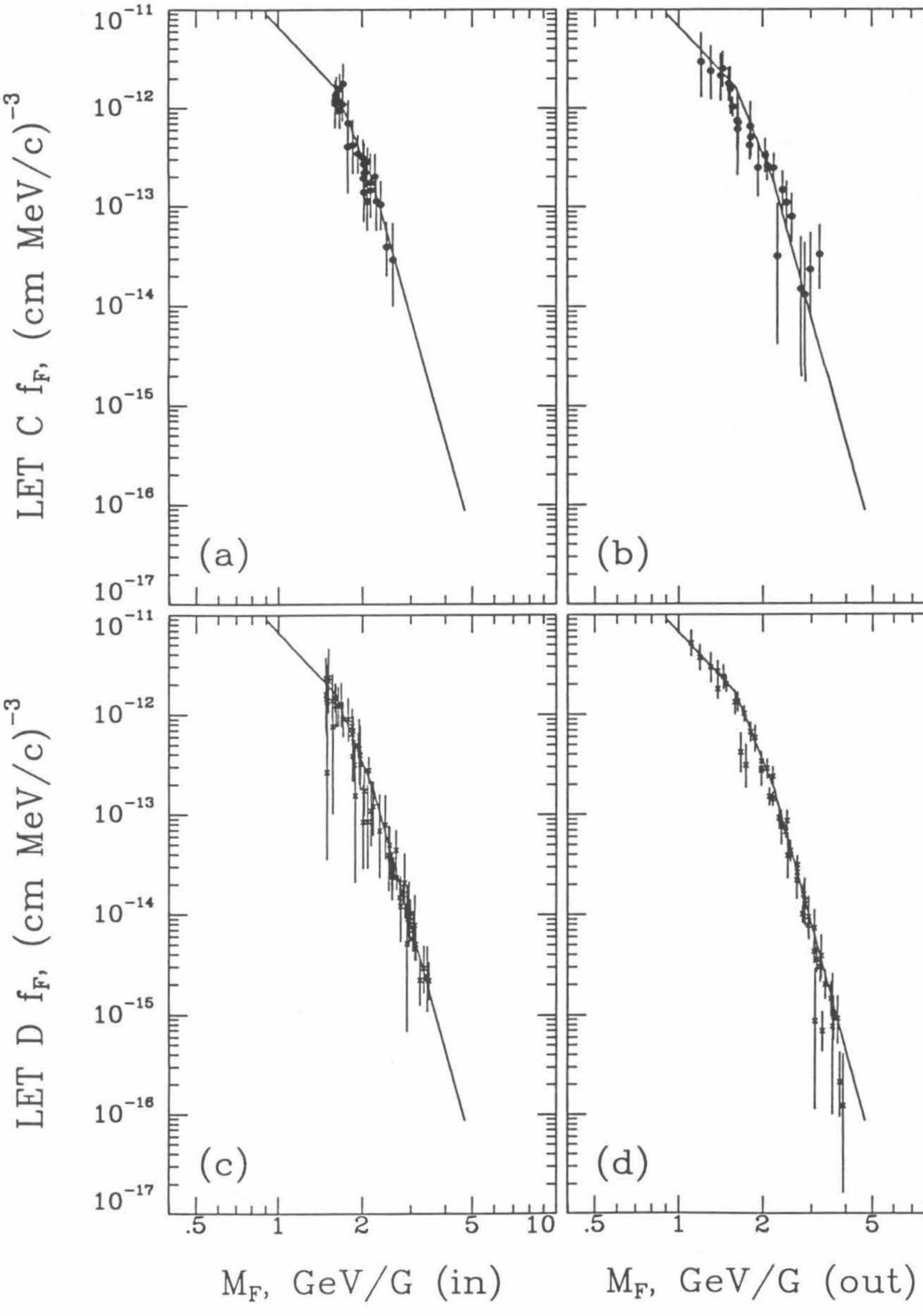
LET C f_F, (cm MeV/c)$^{-3}$
LET D f_F, (cm MeV/c)$^{-3}$
10^{-11}
10^{-12}
10^{-13}
10^{-14}
10^{-15}
10^{-16}
10^{-17}
(a)
(b)
(c)
(d)
.5
1
2
5
10
M_F, GeV/G (in)
M_F, GeV/G (out)

$$\chi_P^2 \equiv 2\sum_i \left[\mu_i - N_i + N_i \ln\left(\frac{N_i}{\mu_i}\right)\right] \tag{5.3}$$

(Baker and Cousins 1984) for Poisson statistics instead of the usual Gaussian χ^2; μ_i is the expected number of counts calculated from the model (and considerations such as livetime, geometry factor, energy bin width, *etc.*) for a given energy channel at a given time period, the set of which is varied by adjusting the model parameters to give the best fit to the observed numbers of counts N_i. D_{LL} was taken to be a power law in L; thus the fit parameters were the normalization and exponent of this power law, and the exponent n in equation 5.2. The minimum of χ_P^2 was sought using a conjugate gradient algorithm (FRPRMN) from Press *et al.* (1988). The best fit achieved is shown in figures 5.3; for this,

$$D_{LL} = 1.7\times10^{-8}\left(\frac{L}{8}\right)^{9.6} \text{sec}^{-1} \text{ and } n = 0.44. \tag{5.4}$$

Fluxes in individual energy bins are plotted on the same scale, spread by 10× for easier visibility. Outbound fluxes are plotted against guiding center L; inbound fluxes are plotted against time because of the turnaround in L apparent in figure 3.2(a).

The model behind the calculated fluxes in figures 5.3 is illustrated in figures 5.4. Figure 5.4(a) shows phase-space density as a function of L for several Ks and Ms chosen to have approximately the same energy at each L (and exactly the same at $L = 10$); figure 5.4(b) shows contours in the L-α_0 plane of the phase-space density in figure 5.4(a), and also shows the guiding center Ls and equatorial pitch angles of the particles that comprise the observations in figures 5.3. The relatively good agreement in figures 5.3(a) and 5.3(c) between model and observations in both LETs' later inbound data implies that the model does a good job of reproducing the real pitch angle distribution as the LETs sample a wide range of equatorial pitch angles around $L \approx 8$ (as the turnaround in L occurs and the spacecraft goes to high latitudes). In particular, note that the last several points (at the highest Ks or lowest α_0s) should reflect the reduction, indeed reversal, of the pitch-angle anisotropy as seen in figure 5.4(b) in that as α_0 approaches 0 the contour lines bend back sharply, becoming nearly vertical in the vicinity of the observations; this is reflected in figure 5.4(a) by the fact that the lowest two phase-space density curves (for $K = 0.50\,R_N\sqrt{\text{G}}$ and $K = 0.73\,R_N\sqrt{\text{G}}$)

cross and recross from $L \approx 7.8$ to 9.0, while the curves for all other pitch angles are spreading out. The explanation for this feature of the model follows from the orbit of the moon, shown as a heavy dashed line in figure 5.4(b): note that inside of our outer boundary at $L = 10$ the moon does not travel to latitudes above the mirror points of particles with $\alpha_0 \approx 17^\circ$, or $K \approx 0.50 R_N \sqrt{G}$ (and it does not go much higher at Ls outside our boundary, so the effect is not strongly dependent on the choice of that boundary). Thus, considering a higher K than that, at a given L particles diffusing inward from higher Ls will not have suffered additional absorption at Ls where particles with $K = 0.50 R_N \sqrt{G}$ would not have been absorbed: both Ks will have been absorbed at Ls all the way out to the boundary, since the moon absorbs a fraction of all particles with mirror points above its latitude, and its latitude is below the mirror points of the high-K particles considered at all Ls inside the boundary. Thus there is not increased absorption of particles as K increases beyond $K \approx 0.50 R_N \sqrt{G}$; in fact, absorption is reduced: the steeper pitch angle at a given λ_m (whence L for the absorbing moon) for a higher K increases the corkscrew effect so τ_{ss}^{-1} is smaller at a given L for a higher K. Thus the contour lines in figure 5.4(b) become nearly vertical above the moon's highest point, and then bend back as the reduced τ_{ss}^{-1} has its effect at lower α_0s. In terms of our observations, this means that the calculated fluxes are relatively insensitive to the pitch-angle distribution assumed at the boundary and to any errors in identifying the K of the particles, so that the relatively good agreement of model and observations for these points reflects mostly on the choice of D_{LL} in that region. A further discussion of the sensitivity of the fit to different parameters in different regions is presented in appendix 3.

Qualitatively, in terms of locations of maxima and minima, the model fluxes agree worst with the observations in the LET C outbound data set, which not coincidentally samples the lowest values of L. Of particular interest is the jump in flux evident in the model, but not in the observations, from $L > 7$ to $L < 7$ in figure 5.3(b); this is the location of the spacecraft roll maneuver mentioned in chapter 3. This jump is even more prominent in a model (with higher exponent in D_{LL}) resulting from a fit with boundary condition normalization left to float. The reason for the jump is evident in figures 5.4: absorption by 1989N1 extends to higher Ls at higher Ks (except as noted above for very high Ks), so phase-space densities of particles mirroring farther from the equator are eroded more drastically at a given

Figure 5.3

Observed and simulated proton fluxes; from top to bottom in each figure are plotted 1.9-2.1 MeV, 2.1-2.9 MeV, 3.2-3.7 MeV, 3.7-4.3 MeV, 4.3-5.0 MeV (some figures lack the one or two highest-energy bins). The lowest-energy bin is normalized correctly, but each subsequent curve is reduced by a factor of 10 relative to the previous one, to improve visibility. Figures are (a) LET C inbound, (b) LET C outbound, (c) LET D inbound, (d) LET D outbound. Points with error bars are observed fluxes; open points are from a radial-diffusion model with

$$D_{LL} = 1.7\times10^{-8}\left[\frac{L}{8}\right]^{9.6} \text{sec}^{-1} \text{ and } n = 0.44,$$

with boundary condition normalization as in figures 5.1 and 5.2.

Figure 5.3

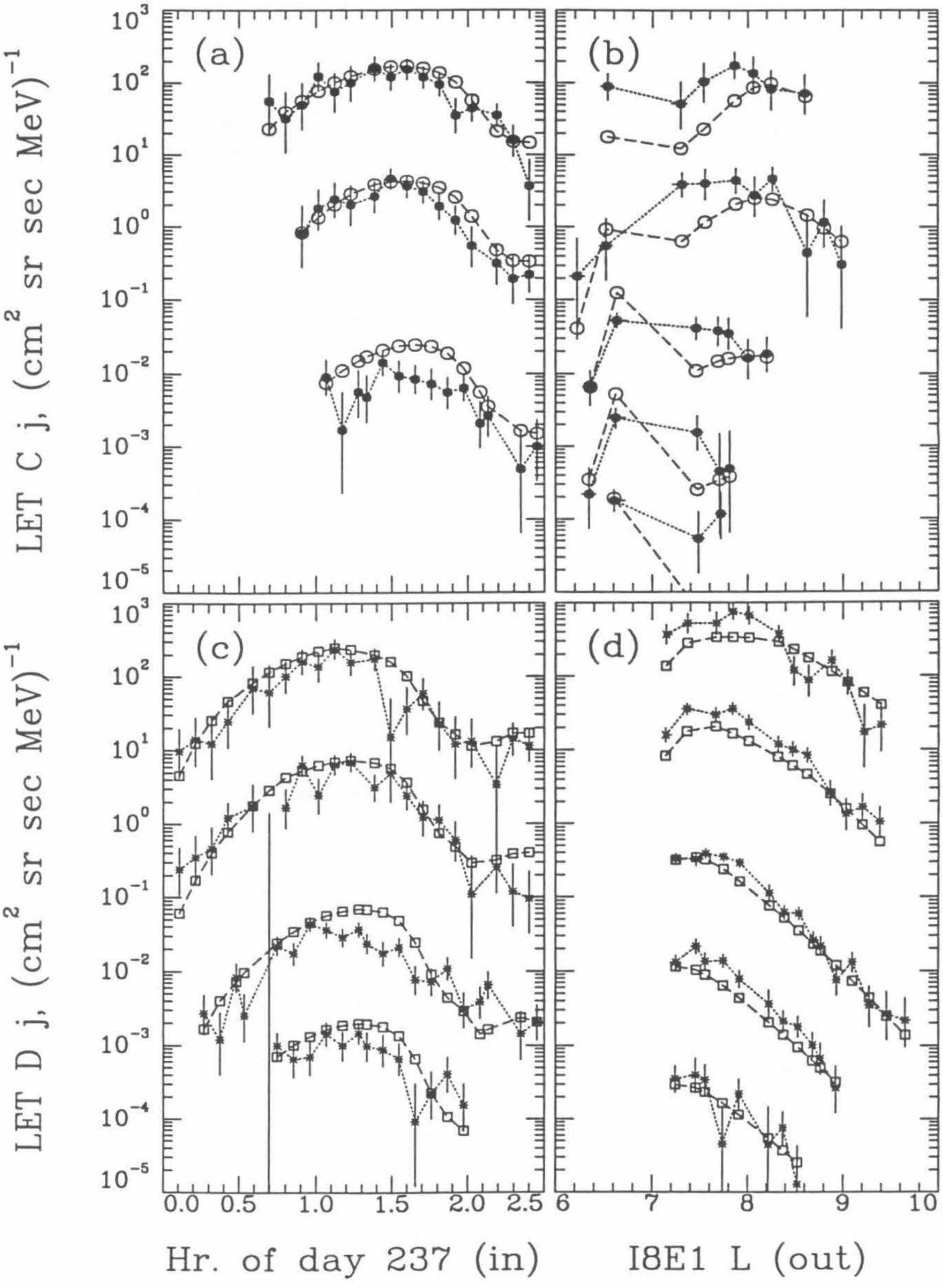
(a)
(b)
(c)
(d)
LET C j, (cm^2 sr sec MeV)$^{-1}$
LET D j, (cm^2 sr sec MeV)$^{-1}$
10^3
10^2
10^1
10^0
10^{-1}
10^{-2}
10^{-3}
10^{-4}
10^{-5}
0.0
0.5
1.0
1.5
2.0
2.5
6
7
8
9
10
Hr. of day 237 (in)
I8E1 L (out)

Figure 5.4(a)

Proton phase-space densities for the model of figures 5.3, plotted for fixed K and M. The Ks and Ms plotted are chosen for most direct comparison to later figures, and to have the same energy (1.3 MeV) at $L = 10$ for all curves. For K in $R_N\sqrt{G}$ and M in GeV/G, from top to bottom (in order at the $L = 10$ boundary) are plotted $K = 0$, $M = 10$; $K = .0035$, $M = 9.6$; $K = .016$, $M = 8.4$; $K = .045$, $M = 6.4$; $K = .13$, $M = 3.6$; $K = .18$, $M = 2.775$; $K = .27$, $M = 1.9$; $K = .50$, $M = 0.975$; $K = .73$, $M = 0.591$.

Figure 5.4(b)

Contour plot in plane of equatorial pitch angle vs. L of the phase-space densities produced by the same model, for Ks and Ms that have a constant energy (1.3 MeV) at $L = 10$. Curves are from $\log_{10}f = -12$ to $-16\frac{1}{2}$ by steps of $\frac{1}{2}$ (in units of (cm MeV/c)$^{-3}$) from lower right to upper left. Closed circles (LET C) and crosses (LET D) represent the α_0 and L values of the data points in figures 5.3; heavy dashed line is the orbit of 1989N1, with the moon's magnetic latitude converted to the α_0 of particles mirroring at that latitude.

Figure 5.4

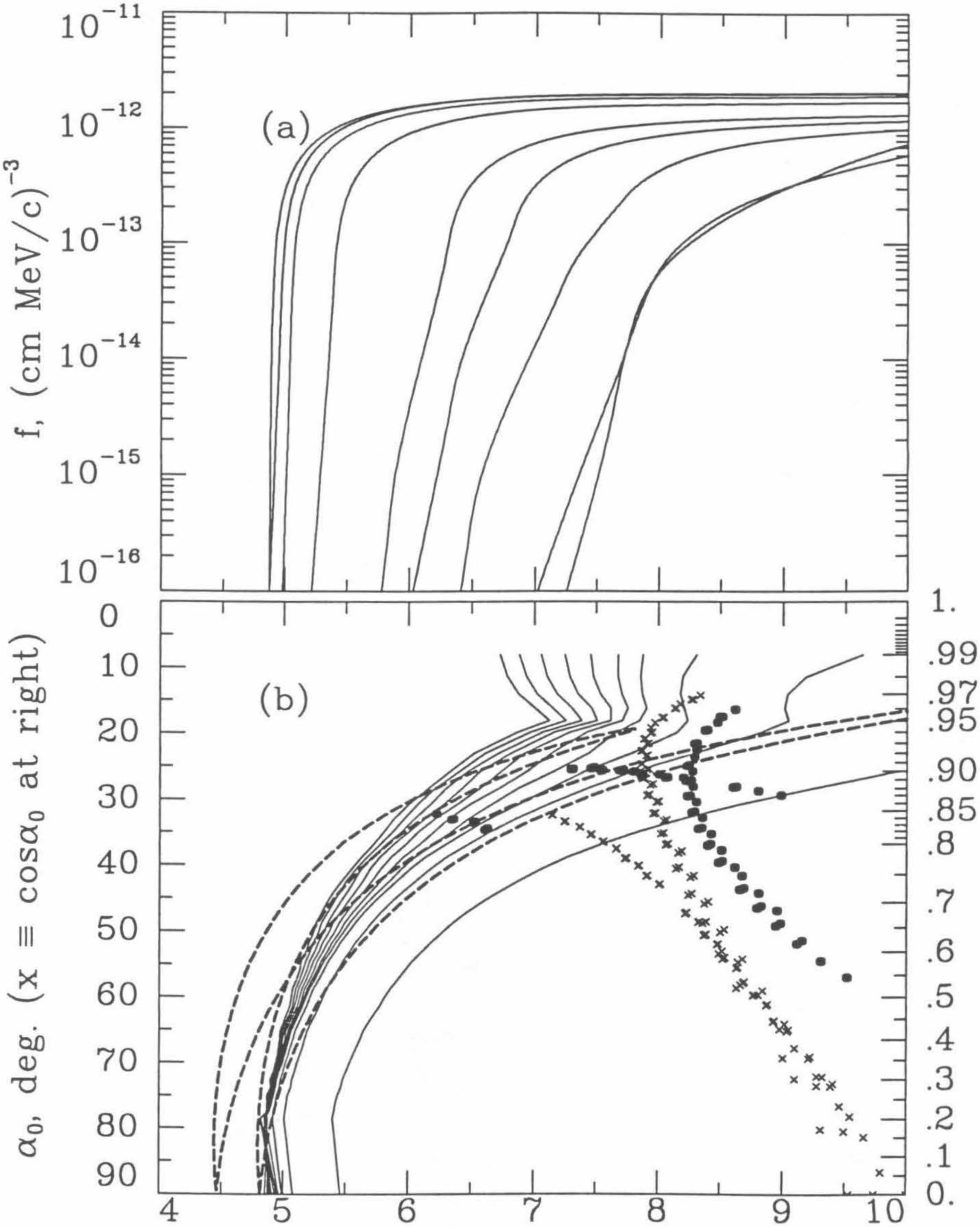
(a)
f, (cm MeV/c)$^{-3}$
10^{-11}
10^{-12}
10^{-13}
10^{-14}
10^{-15}
10^{-16}
(b)
α_0, deg. (x ≡ cosα_0 at right)
0
10
20
30
40
50
60
70
80
90
1.
.99
.97
.95
.90
.85
.8
.7
.6
.5
.4
.3
.2
.1
0.
4
5
6
7
8
9
10
L

L inward from the boundary at $L = 10$ than are particles mirroring nearer the equator. This results in extreme pitch-angle anisotropy by $L \approx 7$ in the range of K sampled by our data, as seen in figure 5.4(a) by the spreading-out of the curves and in figure 5.4(b) by the crowding-together of the contour lines in that region. LET C would be expected to observe this anisotropy as the roll maneuver changes its pointing direction (LET D on the low-L side of the roll samples even steeper pitch angles, so it gives qualitative evidence of the anisotropy as well by its vanishing count rate there; this is where the data points end in figure 5.3(d)). But while there is evidence in the observations for anisotropy in that LET C in figure 5.3(b) shows higher fluxes at $L < 7$ than at $L > 7$ at most energies, as contrasted with the decline shown by LET D in figure 5.3(d) around those Ls (which reflects the general decrease in f with decreasing L, rather than pitch-angle variations), the large jump in the model fluxes in figure 5.3(b) shows that the model clearly produces too much pitch-angle anisotropy in the region observed near the roll maneuver.

Finally, the large exponent on L and small normalization of D_{LL} are reflected in the relatively sudden onset of the decline in f (whence j) with decreasing L observed on the outbound leg, and also in that the proton fluxes do not recover inward from the minimum L of 1989N1 as do the electron fluxes in figure 2.8(c) (the minima in the TET D1 and D2 rates are at about 05:10; as can be seen in figures 2.9, 2.10, 2.11, and 2.12, the proton flux is down to background levels at that point). A larger value of D_{LL} is associated with more filling-in and widening of an absorption feature; thus the small normalization and large exponent in the power law assumed for D_{LL}, which result in a very small D_{LL} at lower Ls, suggest that as protons diffuse inward, once the flux starts to be cut into by 1989N1 it will not recover. As D_{LL} approaches 0, phase-space density profiles like those in figure 5.4(a) would become flatter outside the cutoff L where particles at each K first encounter the moon, and the cutoff would become sharper; in a contour plot like figure 5.4(b), vanishing D_{LL} would result in all the contour lines bunching up on top of the dashed line indicating the highest-L leg of the moon's orbit. In fact, this is a good description of the model at lower Ls (with lower D_{LL}s), and is not a bad approximate description at all Ls. In contrast, the electrons at CRS energies, for which Selesnick and Stone (1991b) found

$$D_{LL} \approx 5\times10^{-7}\left[\frac{L}{8}\right]^{7} \text{sec}^{-1}, \tag{5.5}$$

show the absorption signature largely filled in outside $L \approx 6$ (by which point the CRS protons have vanished altogether), and their flux recovers inward of $L \approx 4.75$ before finally being cleared out by the satellites and rings inward from 1989N1. (Modeling the proton distribution with the same D_{LL} also produces a recovery of flux inside the minimum L of 1989N1.) That this occurs, despite the more rapid absorption of electrons evident in, *e.g.*, figures 4.6(b) and 4.6(c), clearly implies that the proton data cannot support this much diffusion. A comparison of models with more and less diffusion than that of the nominal model above in appendix 3 indicates that the normalization of D_{LL} at $L = 8$ is probably correct within a factor of about 3, while the electrons have about 30 times as much diffusion at $L = 8$. The exponent on L in the assumed power law for D_{LL} is not as well constrained by the observations. A large exponent, in addition to cutting D_{LL} at low Ls and thus helping explain the lack of a recovery of flux inward of 1989N1, would result in a high value of D_{LL} at high Ls and would thus flatten the phase-space density profiles of figure 5.4(a) there at Ks for which the absorption signature of 1989N1 extends that far out. However, as our observations sample those Ls only at relatively low Ks where there is no absorption anyway, the dependence of the expected flux from the model at the points observed on this exponent is weak there, and on the whole this parameter is not very well constrained by the observations; as argued in appendix 3, we can say with confidence only that it is between about 5 and 15. The third parameter of our fit, n in equation 5.2, results in models consistent with the observations if it is between about 0 and 1.2; this is also not a very good constraint.

In summary, the radial-diffusion model presented here seems to explain several qualitative features of the proton observations, and to give good quantitative results from $L \approx 8$ outward, but inward of $L \approx 7$ it produces too much pitch-angle anisotropy.

5.2. Combined Radial- and Pitch-Angle-Diffusion Models

5.2.1. Theory

In order to decrease the pitch-angle anisotropy produced by the model just discussed, we now introduce pitch-angle diffusion into our models, whereby the more-abundant particles at lower Ks act as a source to repopulate the more-effectively-swept higher Ks. Elastic or nearly-elastic pitch-angle scattering will cause protons to diffuse in both K and M, which will require us to solve equation 4.3 in three dimensions. To simplify the task to two dimensions, Walt (1970) changes variables from (M, J, Φ) or (M, K, L) to (ζ, x, L) (within a constant multiplying ζ), where

$$x = \cos(\alpha_0) \equiv \sqrt{1 - y^2} \tag{5.6}$$

and

$$\zeta = \frac{M}{\sin^2(\alpha_0)} \equiv \frac{M}{y^2}. \tag{5.7}$$

x is approximately conserved in radial diffusion at constant K and M (that is, to the degree that the lines of constant K in figure 3.1 approximate lines of constant magnetic latitude λ_m, whence x for particles mirroring there); and ζ is conserved in pitch-angle scattering at constant energy, and is approximately conserved in radial diffusion to the same extent as is x. Thus on the assumption of nearly-elastic pitch-angle scattering at constant L, we can consider the diffusion tensor $\mathbf{D}$ in equation 4.3 to have only components D_{LL} and D_{xx}, and solve the resulting equation at constant ζ. Then the Jacobian

$$G \propto \left[\frac{\zeta}{L^5}\right]^{\frac{1}{2}} xT(y), \tag{5.8}$$

where $T(y)$ equals $H(\lambda_{mirr})$ from equation 3.8 expressed as a function of y, and equation 4.3 becomes

$$L^{\frac{5}{2}} \frac{\partial}{\partial L}\left[L^{-\frac{5}{2}} D_{LL} \frac{\partial f}{\partial L}\right] + \frac{1}{xT(y)} \frac{\partial}{\partial x}\left[xT(y) D_{xx} \frac{\partial f}{\partial x}\right] = \frac{f}{\tau_{ss}} \tag{5.9}$$

(Schulz and Lanzerotti 1974). A test of the quality of the approximate conservation of x and ζ under radial diffusion (at constant K and M) is to redo the solution of the diffusion equation in the previous section using equation 5.9 with D_{xx} set to zero, using the same numerical procedure as for equation 5.1 at fixed x and ζ rather than K and M; the result of this is shown in figures 5.5 as dotted curves (the previous solution is shown as solid curves). The difference amounts to a small displacement of each curve, which will certainly produce a small difference in the fit compared to other sources of error.

To solve equation 5.9, Walt (1970) suggests expanding the solution f at each L in a series of eigenfunctions of the x differential operator in the second term. If D_{xx} is assumed not to depend on x and if the derivative with respect to x of $T(y)$ is ignored ($T(y)$ varies by less than a factor of 2 over the whole range of y), then they can be taken outside the partial derivative, and the eigenvalue equation becomes (Schulz and Lanzerotti 1974)

$$\frac{D_{xx}}{x}\frac{\partial}{\partial x}\left[x\frac{\partial g_i}{\partial x}\right] = -\lambda_i g_i(x) \tag{5.10}$$

with boundary conditions

$$g_i(1) = 0 \tag{5.11}$$

(assuming a small loss cone, *i.e.*, near $x = 1$, of pitch angles with such high λ_{mirr} that they will intersect the planet's atmosphere within τ_b; this is appropriate for the L range covered by the proton observations) and orthonormalization

$$\int_0^1 x g_i(x) g_j(x) dx = \delta_{ij}. \tag{5.12}$$

The eigenfunctions are

$$g_i(x) = 2^{½}\frac{J_0(k_i x)}{J_1(k_i)}, \tag{5.13}$$

where J_0 and J_1 are the Bessel functions of orders 0 and 1, and the eigenvalues are

$$\lambda_i = D_{xx} k_i^2, \tag{5.14}$$

where k_i is the ith root of J_0: $k_1 \approx 2.405$, $k_2 \approx 5.520$, $k_3 \approx 8.654$, *etc.* (*e.g.*, Abramowitz and Stegun 1964). Then for each ζ we can expand

$$f(x,L) = \sum_i a_i(L) g_i(x) \tag{5.15}$$

and use equation 5.12 to break equation 5.9 into a set of coupled linear ordinary differential equations

$$L^{\frac{5}{2}}\frac{d}{dL}\left[L^{-\frac{5}{2}} D_{LL}\frac{da_i}{dL}\right] - \lambda_i a_i = \sum_j \tau_{ij}^{-1} a_j, \tag{5.16}$$

Figure 5.5(a)

Proton phase-space densities for the model of figures 5.3 and 5.4, plotted for fixed x and ζ. Solid curves match the curves in figure 5.4(a) at $L = 10$, but inward from there they assemble solutions of equation 5.1 at the appropriate (slightly different) Ks and Ms to match the selected xs and ζ at each L. $\zeta = 10^4$ MeV/G for all curves, and from top to bottom (in order at the $L = 10$ boundary) are plotted $x = .0$, $x = .2$, $x = .4$, $x = .6$, $x = .8$, $x = .85$, $x = .90$, $x = .95$, and $x = .97$. Dotted curves are for the same xs and ζ, but calculated directly for fixed x and ζ rather than K and M, using equation 5.9 rather than equation 5.1.

Figure 5.5(b)

Contour plots of the calculations above, plotted as in figure 5.4(b) except that $\zeta = 10^4$ MeV/G is held constant as in figure 5.5(a). Again, solid lines are calculated using equation 5.1 and dotted lines using equation 5.9.

Figure 5.5

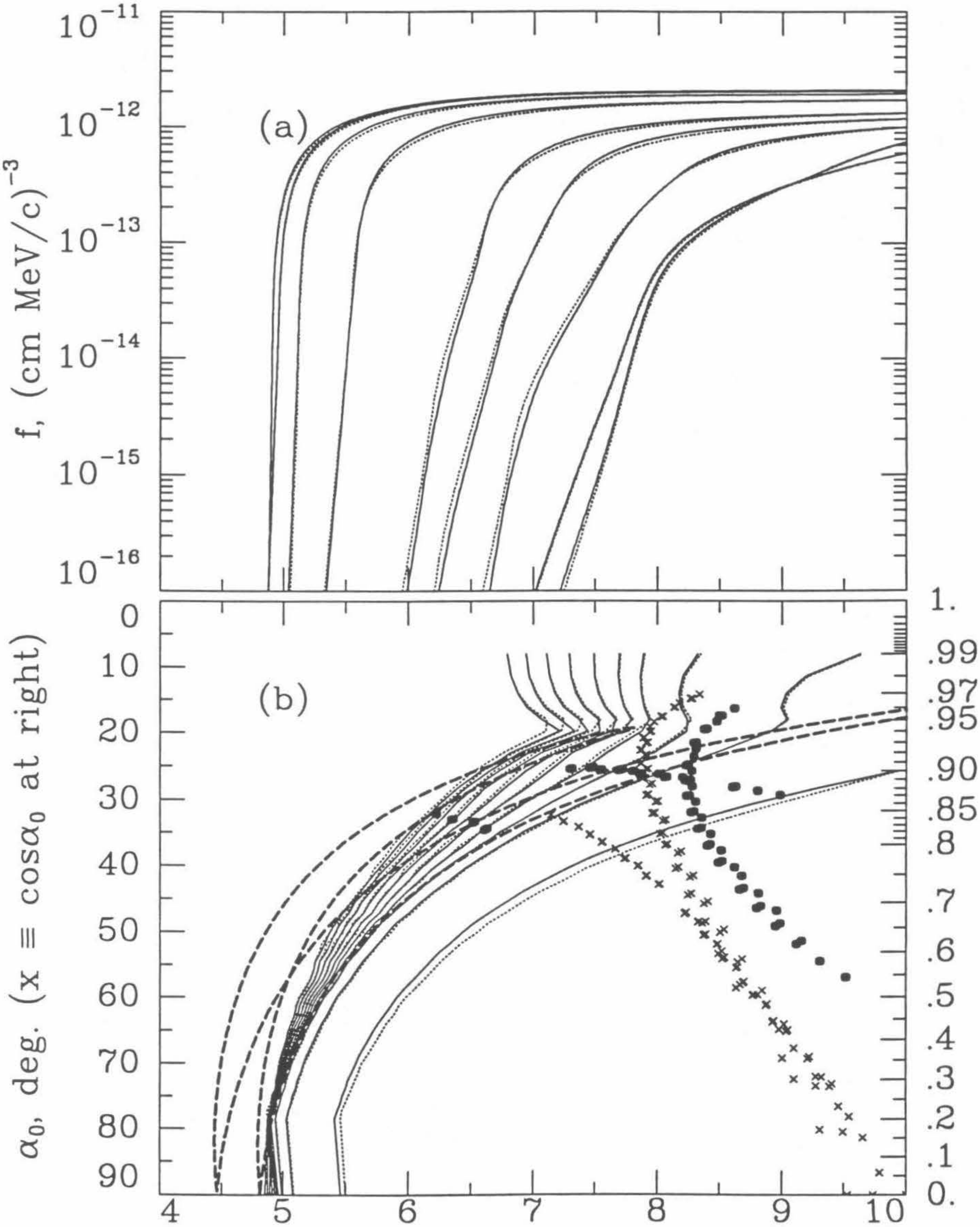

(a)
(b)
f, (cm MeV/c)$^{-3}$
10^{-11}
10^{-12}
10^{-13}
10^{-14}
10^{-15}
10^{-16}
α_0, deg. (x ≡ cosα_0 at right)
0
10
20
30
40
50
60
70
80
90
1.
.99
.97
.95
.90
.85
.8
.7
.6
.5
.4
.3
.2
.1
0.
4
5
6
7
8
9
10
L (ζ = 10^4 MeV/G)

where

$$\tau_{ij}^{-1} = \int_0^1 \tau_{ss}^{-1}(x) x g_i(x) g_j(x) dx \tag{5.17}$$

(Selesnick and Stone 1991a).

5.2.2. Fits

5.2.2.1. Boundary Conditions

We need two boundary conditions for each of the coupled equations 5.16; as in the radial diffusion fit of §5.1, we assume that f, whence each a_n, vanishes at $L = 3$, and set a pitch-angle distribution and spectrum at $L = 10$. The spectral shape assumed is the same as in that calculation, with overall normalization left as a fit parameter, and a pitch-angle distribution of the form of equation 5.2 is also assumed, *i.e.*,

$$f(x, L=10) \propto \sin^{2n}\alpha_0 = (1 - x^2)^n ; \tag{5.18}$$

using equation 5.12, this means that

$$a_i(L=10) \propto \int_0^1 x(1 - x^2)^n g_i(x) dx , \tag{5.19}$$

with proportionality constant determined from the spectrum in ζ. In a region of no absorption, equations 5.16 will decouple and each mode g_n will diffuse independently, with λ_n as an inverse lifetime against scattering into the loss cone. Since λ_n increases with n, the lowest mode is longest-lived, and thus it should be the dominant contribution to f where pitch-angle diffusion operates in the absence of satellite losses. Where pitch-angle diffusion dominates satellite absorption as a mechanism for shaping the pitch-angle distribution, this should also be approximately true. $g_1(x)$ is approximately proportional to a pitch-angle distribution of the form of equation 5.18 with $n = 1.4$ (Selesnick and Stone 1991a); thus if pitch-angle diffusion operates on protons in our K and M range in the region between the outer range of absorption by 1989N1 and the minimum L (and inner edge of absorption) of Triton, we might expect the best fit to have n of approximately this value at our boundary of

$L = 10$. Since we expect our solution to resemble that of the radial-diffusion model near this boundary (as it reproduced the observations there pretty well), and since the best-fit value of n was well below 1.4 for that model, we already have an indication that pitch-angle diffusion is not significant for protons at CRS energies at these higher Ls. This, of course, assumes that the lowest pitch-angle eigenmode is well-represented by $g_1(x)$, *i.e.*, that D_{xx} is approximately independent of x as assumed in the derivation of equations 5.10 to 5.12; one could construct an x-dependent D_{xx} which would produce a lowest eigenmode with a different form, say, one with $n \approx 0.44$, so this is not a conclusion independent of the assumptions in our simple model.

5.2.2.2. Truncation of the Series

Selesnick and Stone (1991a) found that numerical solutions of equations 5.16 for CRS electrons around the Uranian satellite Ariel required only terms up to $i,j = 6$ for stability of the modeled data. However, the observations being reproduced were made with single detectors of the TET, and as such had a broad acceptance cone; thus the counting rates and energy spectra were dominated by the more-abundant low-x fluxes, which require fewer terms in the series to model. The LETs are highly directional, however, and thus sample only a narrow range of xs; and simulation of our proton observations requires calculation of phase-space densities to $x = 0.97$. It was found that there was little difference between the fluxes calculated with 16 terms and 20 terms, so the results below use 20 terms in the series. However, the use of a finite number of terms and the fact that the integral in equation 5.17 for τ_{ij}^{-1} was done numerically with a finite resolution ($dx = 0.02$) result in some errors in the solution, as detailed in appendix 4; in particular, phase-space densities are not forced to be nonnegative by the construction of the equations, as is the case for equation 5.1, and some model calculations resulted in phase-space densities at high xs that were negative. This is not a problem for the range of models discussed below, however, and other limitations of the parametrization below overshadow the difficulties described in appendix 4.

5.2.2.3. Results

A power law dependence of D_{LL} on L is predicted for several possible forms of perturbation of the magnetic field, as will be discussed in chapter 6; however, the need for a nonzero D_{xx} inside about $L = 7$ and zero outside does not suggest any particular parametrization. Accordingly, we fit a model to the data by assuming a constant value for D_{xx} inside some particular $L = L_0$, and zero outside; actually, the numerical procedure used to solve equations 5.16 (the same as used for equations 5.1 and 5.9 with $D_{xx} \equiv 0$, but with 20 coupled equations to cover all xs at each ζ, rather than one uncoupled equation for each x and ζ) became confused in the region of L_0 if the turn-on of D_{xx} was too abrupt, so a Fermi-like function was used to smooth the transition:

$$D_{xx} \propto \frac{1}{e^{\frac{L-L_0}{\Delta L}} + 1}. \tag{5.20}$$

Thus the fit had seven parameters: the normalization and exponent in L of D_{LL}; the normalization of D_{xx}, and the location L_0 and width ΔL of the transition from zero; and the pitch-angle exponent n at $L = 10$ and the normalization of the boundary spectrum, as before assuming the shape to be proportional to f_F.

The best fit achieved is shown in figures 5.6 and 5.7; for these,

$$D_{LL} = 1.2\times10^{-8}\left(\frac{L}{8}\right)^{10.0}\text{sec}^{-1},\ D_{xx} = 1.3\times10^{-8}\left(e^{\frac{L-6.8}{0.15}} + 1\right)^{-1}\text{sec}^{-1},\ \text{and } n = 0.63, \tag{5.21}$$

with normalization reduced to 0.56 times f_F. The phase-space densities are plotted as in figures 5.4, and the fluxes as in figures 5.3. Comparing the latter with figures 5.7, we see that the agreement of the two models with the inbound observations is similar, while the outbound LET C agreement is much improved (with the exception of the one point in the lowest energy bin at $L \approx 6.5$, which looks like a statistical fluctuation). The lower-energy channels in LET D outbound actually agree worse with the observations than in figure 5.3(d); looking at figure 5.6(a), we see that this region of L, and also the region where LET C outbound agreement is worst, is just where the transition from pitch-angle diffusion to no pitch-angle

Figure 5.6

Proton phase-space density (a) traces and (b) contour plot as in figures 5.4 and 5.5, from a model with combined radial and pitch-angle diffusion with

$$D_{LL} = 1.2\times10^{-8}\left(\frac{L}{8}\right)^{10.0} \text{sec}^{-1},\ D_{xx} = 1.3\times10^{-8}\left(e^{\frac{L-6.8}{0.15}} + 1\right)^{-1} \text{sec}^{-1}, \text{ and } n = 0.63,$$

with boundary condition normalization 0.56 times that in figures 5.1 and 5.2. $\zeta = 10^4$ MeV/G throughout, and xs in figure 5.6(a) are as in figure 5.5(a).

Figure 5.7

Observed and simulated proton fluxes plotted as in figures 5.3, from the model of figures 5.6.

Figure 5.6

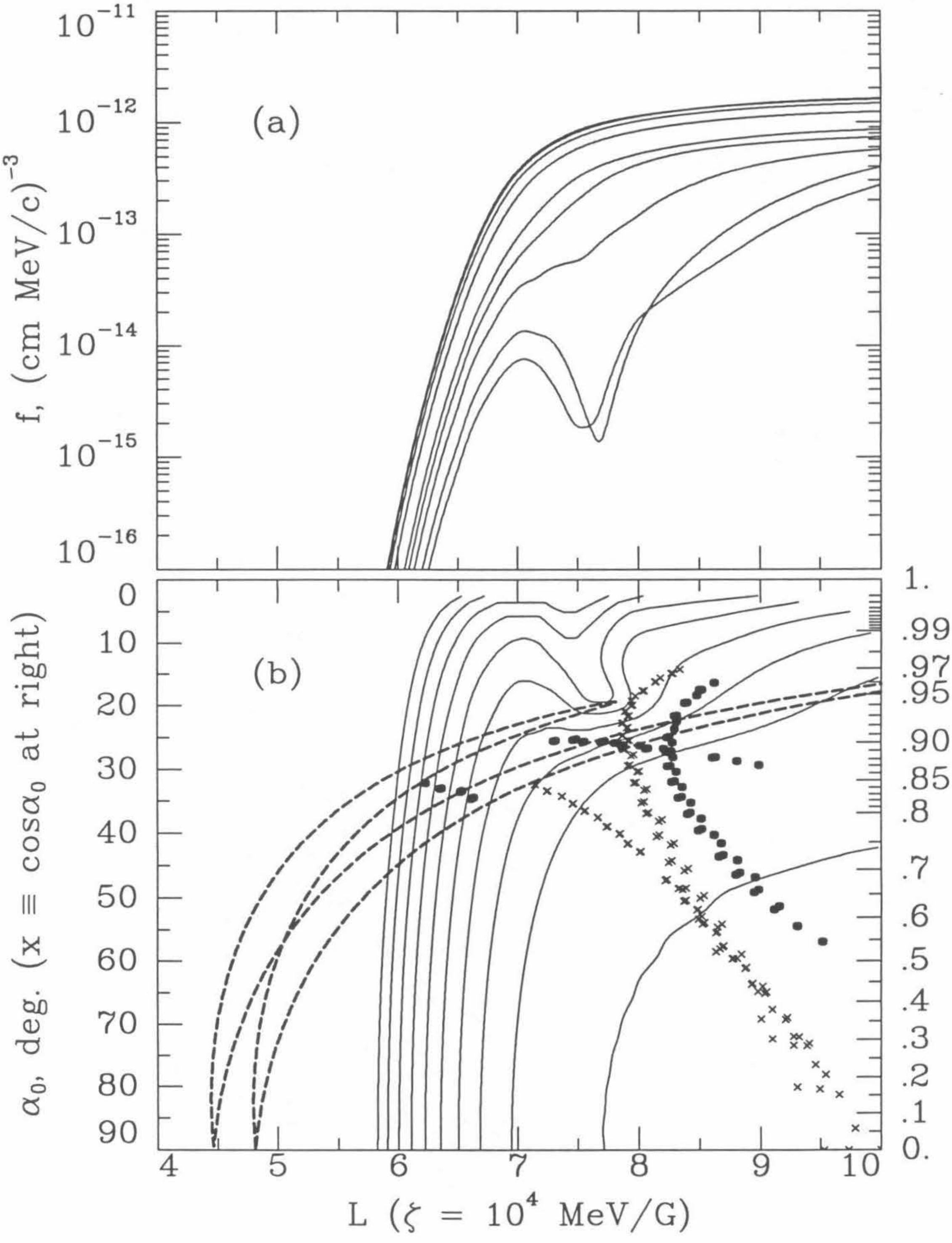
(a)
(b)
f, (cm MeV/c)$^{-3}$
10^{-11}
10^{-12}
10^{-13}
10^{-14}
10^{-15}
10^{-16}
α_0, deg. (x ≡ cosα_0 at right)
0
10
20
30
40
50
60
70
80
90
1.
.99
.97
.95
.90
.85
.8
.7
.6
.5
.4
.3
.2
.1
0.
4
5
6
7
8
9
10
L (ζ = 10^4 MeV/G)

Figure 5.7

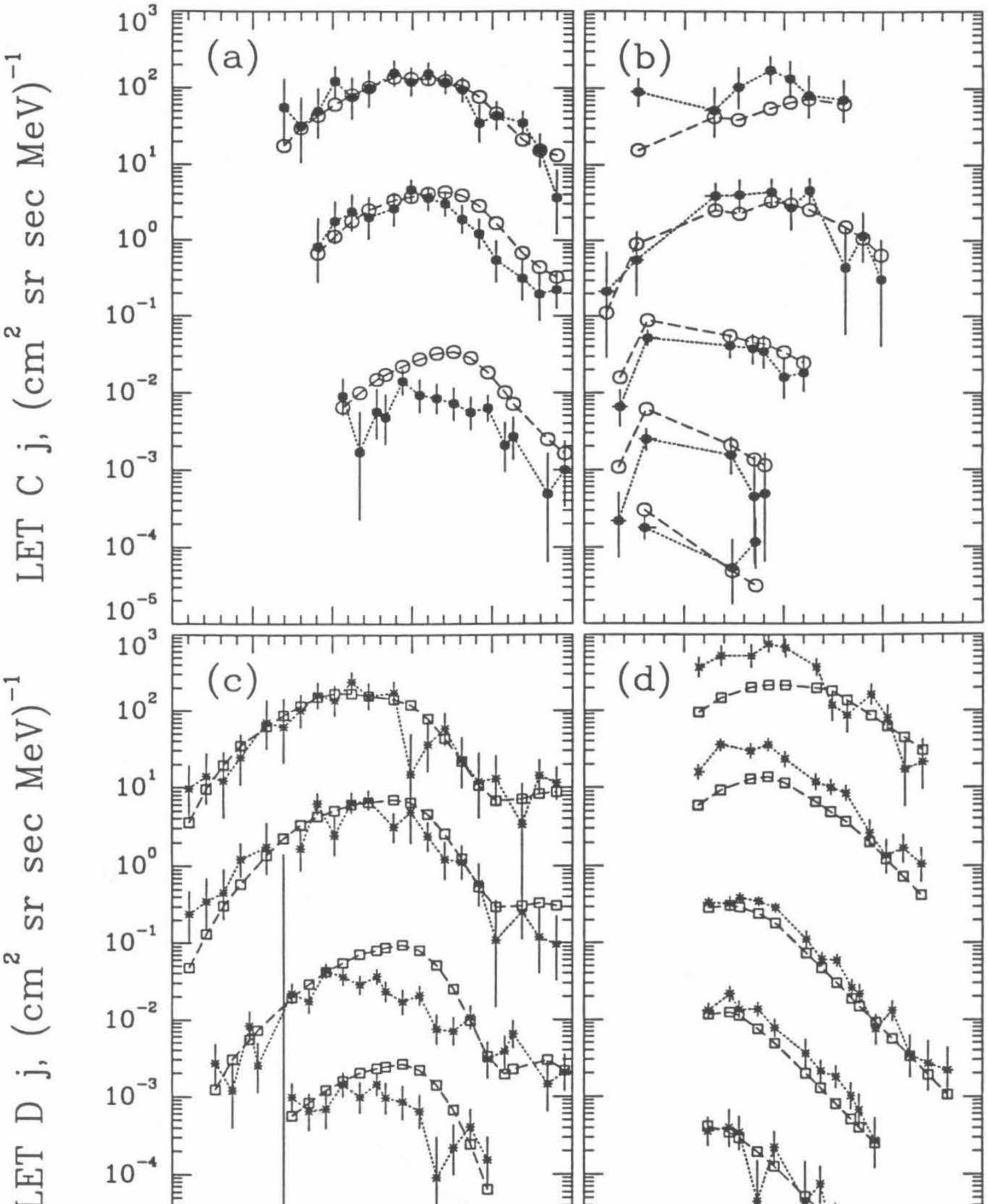
(a)
(b)
(c)
(d)
LET C j, (cm^2 sr sec MeV)$^{-1}$
LET D j, (cm^2 sr sec MeV)$^{-1}$
10^3
10^2
10^1
10^0
10^{-1}
10^{-2}
10^{-3}
10^{-4}
10^{-5}
0.0
0.5
1.0
1.5
2.0
2.5
6
7
8
9
10
Hr. of day 237 (in)
I8E1 L (out)

diffusion is taking place, *i.e.*, in the region of the dips in the phase-space density curves for the higher xs, where filling-in via D_{xx} from lower xs starts to dominate the absorption losses. In figure 5.6(b), this region is visible in that the contour lines lose their doubled-back form (as in figures 5.4(b) and 5.5(b)) and all become roughly parallel to one another, indicating predominance of $g_1(x)$ as absorption-induced anisotropy is reduced. This is, of course, the region most sensitive to the details of our rather simple pitch-angle diffusion model, and thus disagreement here should not undermine the conclusions that we made about D_{LL} and n at the boundary using the radial-diffusion-only model, and which continue to be supported here, as argued in appendix 3; or the general conclusions about D_{xx}, namely that it is comparable to or larger than D_{LL} in the region of its applicability, and that the transition is rather abrupt at $L \approx 6.8$. In appendix 3, a comparison of models differing in the parameters related to pitch-angle diffusion, namely L_0, ΔL, and the normalization of D_{xx}, leads to the conclusions that, as with D_{LL}, we have determined the amount of pitch-angle diffusion within about a factor of 3; that the location L_0 where pitch-angle diffusion comes into play is accurate within about ±0.4 units of L; and that the turn-on is abrupt on the scale of this uncertainty.

More generally, to demonstrate that even a small amount of pitch-angle diffusion in the region outside $L \approx 8$ is too much, figures 5.8 and 5.9 present another model with combined radial and pitch-angle diffusion, but with a uniform value of $D_{xx} = 1.2\times10^{-9}\text{sec}^{-1}$ in the entire region of L considered, and other parameters as in the fit result above. This is about ten times less than the value of D_{xx} inside L_0 for the fit; nonetheless, it is enough to fill in most of the anisotropy developed at high xs in that model outside L_0. This is evident from a comparison of figures 5.8 with 5.6, where the dip in figure 5.6(a) does not have a chance to develop in figure 5.8(a) and the contour lines in figure 5.8(b) never have the doubled-back form mentioned above in figure 5.6(b); and of figures 5.9 with 5.7, where the later inbound data in figures 5.9(a) and 5.9(c) lack the pronounced dip present in figures 5.7(a) and 5.7(c). Indeed, the pitch-angle distribution appears to approximate $g_1(x)$ from the region of the secondary maximum L of 1989N1 ($L_{\text{max}} \approx 7.8$) out to nearly $L = 10$ (where the boundary condition of $n = 0.63$ comes into play), indicating that even this small amount of pitch-angle diffusion is enough to dominate satellite absorption there and force the pitch-angle distribution to match the assumed form of $g_1(x)$. Even if the real form of $g_1(x)$ is different from this, the fact that D_{xx} of this magnitude forces the pitch-angle distribution to conform to $g_1(x)$ in this range of L should remain true in the real case, and since the observations seem to require the pitch-angle distribution to vary it seems that we can conclude that the pitch-angle diffusion really must be negligible there, and that it does turn on fairly sharply in the region stated.

Figure 5.8

Proton phase-space density (a) traces and (b) contour plot as in figures 5.6, from a model with combined radial and pitch-angle diffusion with

$$D_{LL} = 1.2\times10^{-8}\left[\frac{L}{8}\right]^{10}\text{sec}^{-1},\ D_{xx} = 1.2\times10^{-9}\text{sec}^{-1},\ \text{and } n = 0.63,$$

with boundary condition normalization 0.56 times that in figures 5.1 and 5.2.

Figure 5.8

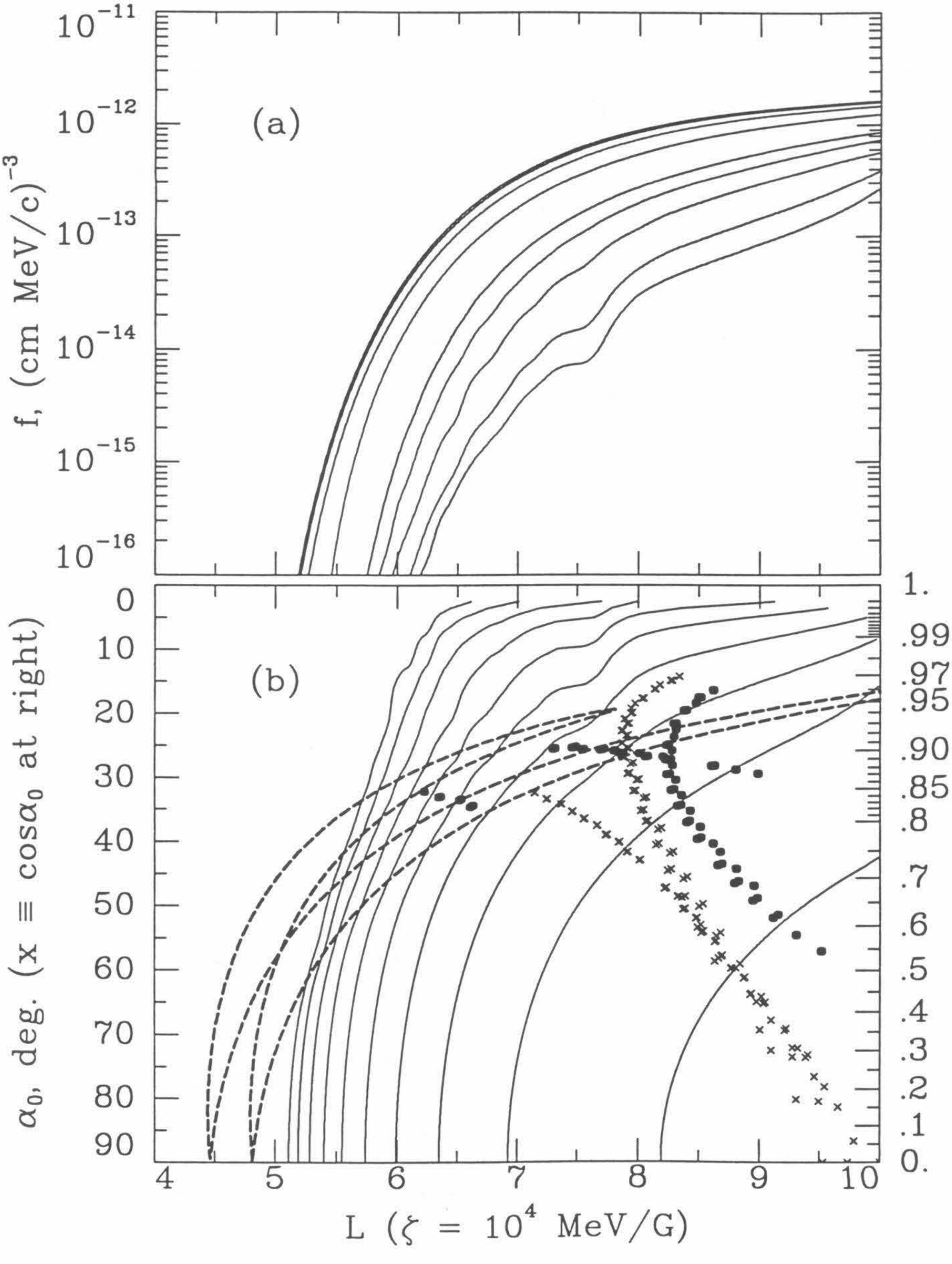
(a)
f, (cm MeV/c)$^{-3}$
10^{-11}
10^{-12}
10^{-13}
10^{-14}
10^{-15}
10^{-16}
(b)
α_0, deg. (x ≡ cosα_0 at right)
0
10
20
30
40
50
60
70
80
90
1.
.99
.97
.95
.90
.85
.8
.7
.6
.5
.4
.3
.2
.1
0.
4
5
6
7
8
9
10
L (ζ = 10^4 MeV/G)

Figure 5.9

Observed and simulated proton fluxes plotted as in figures 5.3 or 5.7, from the model of figures 5.8.

Figure 5.9

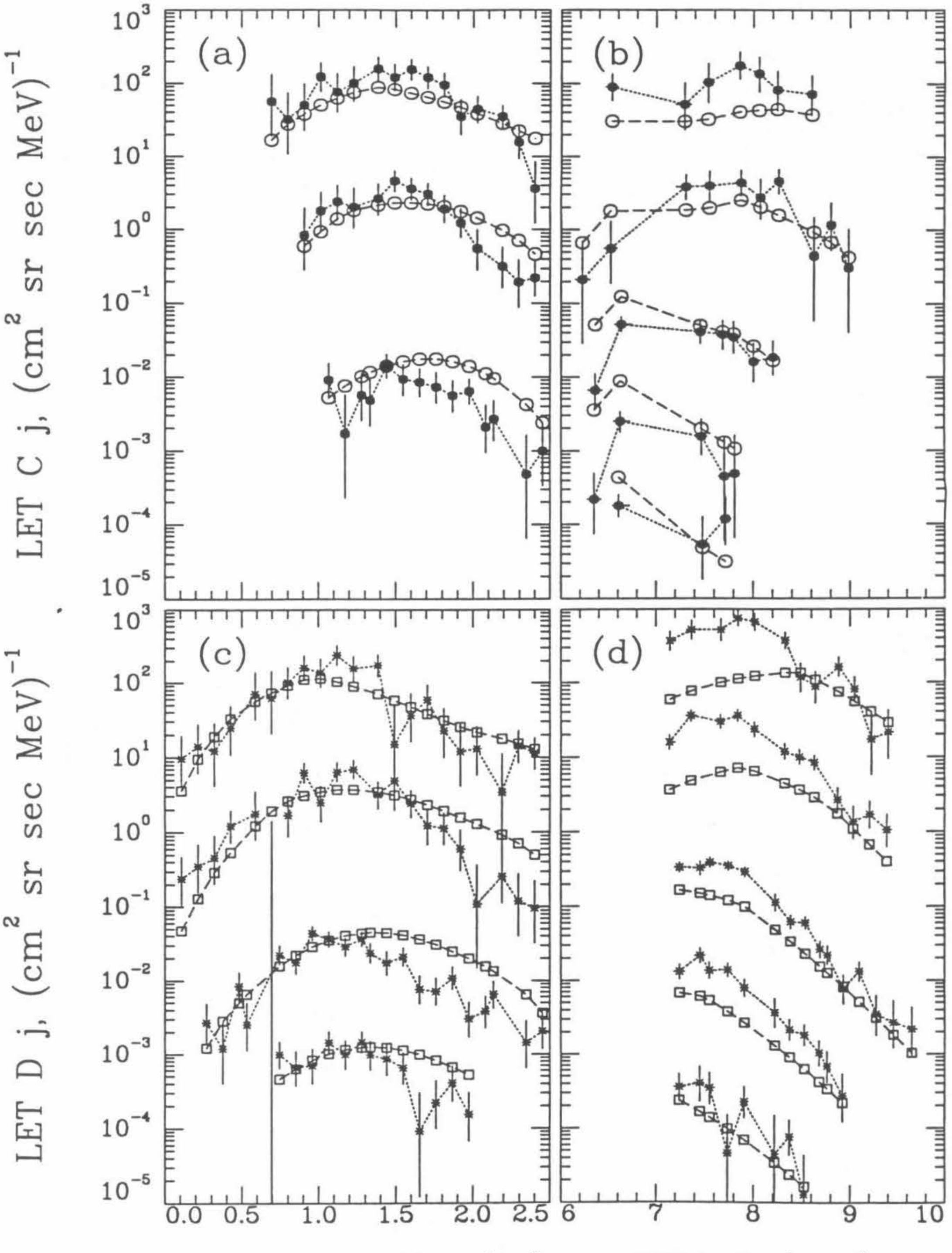
(a)
(b)
(c)
(d)
LET C j, (cm^2 sr sec MeV)$^{-1}$
LET D j, (cm^2 sr sec MeV)$^{-1}$
10^3
10^2
10^1
10^0
10^{-1}
10^{-2}
10^{-3}
10^{-4}
10^{-5}
0.0
0.5
1.0
1.5
2.0
2.5
6
7
8
9
10
Hr. of day 237 (in)
I8E1 L (out)

Chapter 6

Discussion

6.1. Comparison with Other Planets' Energetic Ion Populations

The Cosmic Ray Subsystems aboard the two Voyager spacecraft have observed energetic ions trapped in the magnetic fields of all four of the giant planets in the course of their mission. Each magnetosphere has presented a very different population, and just as the giant planets' magnetospheres differ qualitatively from that of Earth, those of Uranus and Neptune exhibited some systematic differences from those of Jupiter and Saturn. Jupiter's magnetosphere is extensive enough to trap ions other than hydrogen from the solar wind at CRS energies, either ions from flares or lower-energy particles accelerated within the magnetosphere, and it also has a substantial internal source of energetic heavy ions accelerated from the Io plasma torus (Vogt *et al.* 1979). Saturn's contains, in addition to accelerated inward-diffusing protons, an internal source from cosmic ray interactions with the ring material (Schardt and McDonald 1983). Uranus' and Neptune's magnetospheres contain, in the CRS energy range, only protons that have diffused inward from the outer magnetosphere.

The morphologies of the magnetospheres are also very different; first, the two larger planets' magnetospheres are much more shaped by the presence of plasma than are those of the two smaller worlds. β, the ratio of plasma pressure to magnetic pressure $B^2/8\pi$, was greater than unity throughout most of Jupiter's magnetosphere outside 10 Jovian radii (Krimigis *et al.* 1981) and in much of Saturn's outer magnetosphere as well (Krimigis *et al.* 1983); in particular, Jupiter's magnetosphere extends to a much greater distance sunward than would be expected solely from the strength of its internal magnetic field because it is inflated by plasma. Uranus and Neptune, by contrast, have relatively empty "vacuum" magnetospheres with β of much less than unity (Krimigis *et al.* 1986; Krimigis *et al.* 1990), and therefore magnetic fields mostly reflective of the planets' internal dynamos. Also, those internal fields are more complex at the two more distant planets, as reflected in harmonics of higher than dipolar order or in the large tilts and offsets in the dipolar approximations in table 1.1.

Finally, Neptune stands alone in having a well-defined inner edge to its energetic proton population; CRS proton fluxes at other planets in the energy range analyzed here increased as far inward as the spacecraft ventured. Of course, Voyager 2 passed closer to Neptune by far than either Voyager came to any other planet since launch; however, in terms of L-shells (or distance in R_P), all Voyager flybys except Voyager 2 at Jupiter came within the distance from Neptune at which CRS proton flux disappears. Satellite absorption signatures were observed in the proton fluxes at other planets, both macrosignatures and microsignatures, but the relatively simple system (low-β plasma, energization by inward radial diffusion, and (effectively) one absorber and no internal sources in our energy range) for energetic protons at Neptune has allowed us to model the situation globally with some degree of completeness.

6.2. Radial Diffusion

As remarked in chapter 1, the presence of satellites within the magnetospheres of the outer planets allows additional sources and sinks for charged particles besides those operative in the magnetosphere of Earth; in addition, the *in situ* observations starting with Pioneer 10's visit to Jupiter have generally indicated that the mechanisms producing radial diffusion at the outer planets differ from those effective in Earth's magnetosphere. These mechanisms leave their mark in the radial dependence of D_{LL}, with a stronger variation observed at Earth than at the outer planets. Diffusion coefficients can be derived by calculating the effect on particles with a drift period $\tau_d = 2\pi/\omega_d$ of an oscillatory perturbation to the electromagnetic field with a frequency in resonance with the drift motion (which therefore might violate conservation of the third adiabatic invariant, while preserving the first two), and relating this to the power spectrum with respect to frequency of the field fluctuations. At Earth, one mechanism of importance is a compression or expansion of the magnetosphere as a whole in response to changing conditions in the incident solar wind; this has been modeled (Fälthammar 1968; Schulz and Lanzerotti 1974) to give

$$D_{LL}^{M} \propto L^{10}\omega_d^2\tilde{B}(\omega_d), \tag{6.1}$$

where $\tilde{B}(\omega)$ is the power spectrum of the perturbations to the magnetic field and the proportionality accounts for the magnitudes of the undisturbed field and of the disturbance, and for dependence on the equatorial pitch angle of the particles in question. If the compression takes the form of a sudden onset followed by a recovery to the unperturbed state on a timescale long compared to τ_d, then $\tilde{B}$ is just inversely proportional to the square of the frequency, and the ω_d dependence cancels out, taking with it any energy or M dependence of D_{LL}^M. In this case $D_{LL}^M \propto L^{10}$, with a pitch-angle dependence of about a factor of 10 across the range of α_0. Another mechanism that gives a similar L dependence to D_{LL} is due to sudden changes in the magnetospheric electric field; in this case (Fälthammar 1968; Schulz and Lanzerotti 1974)

$$D_{LL}^E = \frac{c^2 L^6}{8 R_P^2 B_P^2} \sum_m \tilde{E}_m (L, m\,\omega_d), \tag{6.2}$$

where $\tilde{E}_m(L,\omega)$ is the power spectrum of the (time-varying) mth azimuthal harmonic of the electric field at L. For the case of variations of the $m = 1$ convection electric field with time variation as described above for magnetic compression (sudden onset, slow decay), the power spectrum is again inversely proportional to ω^2; since at constant K and M, ω_d is proportional to L^{-2}, equation 6.2 again gives $D_{LL}^E \propto L^{10}$ for diffusion with K and M conserved. (Since the energy and pitch-angle variation of ω_d is approximately proportional to $M/\sin^2\alpha_0$, D_{LL}^E has weak dependence on α_0, but depends on kinetic energy (for non-relativistic particles) approximately as E^{-2}.)

At the outer planets, analysis of charged particle phase-space densities suggests weaker dependence of D_{LL} on L. Mechanisms that result in a proportionality to L^3 at low particle energies are flux tube interchange due to centrifugal instability of corotating plasma with a negative radial gradient of mass per unit flux shell, invoked to explain Voyager observations in the vicinity of the Jovian moon Io (Siscoe and Summers 1981), and electric field variations driven by winds in the planetary ionosphere, suggested before the first spacecraft visits to the outer planets in order to explain the the distribution of decimetric synchrotron radio emission at Jupiter (Brice and McDonough 1973). This weak L dependence of D_{LL} is indicated at Saturn as well (Hood 1983), though the balance between the two mechanisms is less clear; at Uranus, the configuration of the cold plasma ruled out centrifugal interchange, but phase-space density profiles of protons and electrons with energies from tens to hundreds of keV suggested a similar weak dependence of D_{LL} on L (Hood 1989), and likewise at Neptune (Cheng *et al.* 1992). At Neptune, Selesnick (1992b) considered a wind-driven model with fluctuations in wind speed δW that turn on suddenly and decay on the timescale of the planet's rotation, so that

$$\tilde{E}_1(L,\omega) = \frac{4\Omega_P^{-1}(\delta E)^2}{1 + \left[\frac{\omega_d}{\Omega_P}\right]^2} \tag{6.3}$$

in equation 6.2, for

$$\delta E = L^{-\frac{3}{2}} B_P \frac{\delta W}{c} \tag{6.4}$$

the mean electric-field fluctuation projected into the magnetosphere; this gives

$$D_{LL}^W = \frac{(\delta W)^2 L^3}{2\Omega_P R_P^2 \left[1 + \left[\frac{\omega_d}{\Omega_P}\right]^2\right]}. \tag{6.5}$$

At low particle energies, the ratio of angular velocities in the denominator is small, so for $\delta W \approx 50$ m/sec,

$$D_{LL}^W \approx 2\times10^{-8} L^3 \mathrm{sec}^{-1}, \tag{6.6}$$

which is close to the estimates from the Voyager 2 Plasma (PLS) (Richardson *et al.* 1991) and Low Energy Charged Particle (LECP) (Cheng *et al.* 1992) experiments' observations of ions, both of which are of order $D_{LL} \approx 10^{-7} L^3 \mathrm{sec}^{-1}$. At high energies, the ratio becomes much greater than unity, so for

$$\omega_d \approx \frac{3c\zeta}{qR_P^2 \gamma L^2} = \frac{4.9\times10^{-2}\mathrm{sec}^{-1}}{\gamma L^2}\left[\frac{\zeta}{10^3\,\mathrm{MeV/G}}\right] \tag{6.7}$$

(within a factor of 1.5 variation with α_0), we have

$$D_{LL}^W = \frac{(\delta W)^2 \Omega_P L^3}{2R_P^2 \omega_d^2} \approx 2\times10^{-7}\gamma^2\left[\frac{L}{8}\right]^7\left[\frac{10^3\,\mathrm{MeV/G}}{\zeta}\right]^2 \mathrm{sec}^{-1}. \tag{6.8}$$

This is in reasonable agreement with the result for CRS electrons of Selesnick and Stone

(1991b), quoted in equation 5.5 as

$$D_{LL}^{e} \approx 5\times10^{-7}\left[\frac{L}{8}\right]^{7}\text{sec}^{-1}, \tag{6.9}$$

for ζ ranging from one thousand to a few thousand MeV/G for most of the particles observed (the agreement is exact for $\zeta \approx 1300$ MeV/G at the minimum L of 1989N1, kinetic energy about 500 keV). As noted in the previous chapter, the models considered for CRS protons are not sufficiently sensitive to the exponent of the L dependence of D_{LL}^{p} to allow us to constrain it well at all, though the observations are certainly consistent with an L^7 dependence. More noteworthy, however, is the normalization of D_{LL}^{p}, which is found to be

$$D_{LL}^{p} \approx 10^{-8}\text{sec}^{-1} \tag{6.10}$$

near $L = 8$ as quoted in equation 5.21, an order of magnitude less for protons than for electrons; this fits with the dependence on γ^2 in equation 6.8 for particles that have approximately the same ζ, as did CRS protons and electrons, in that those electrons were relativistic, with γ of about 3 for a 1-MeV electron at the CRS threshold, whereas CRS protons are nonrelativistic. Thus D_{LL}^{W} for electrons should be at least an order of magnitude greater than for protons, as is indicated by the observations, and thus the CRS proton observations appear to be consistent with this model and with the CRS electron observations.

6.3. Pitch-Angle Diffusion

Pitch-angle diffusion can readily be caused by interactions of energetic particles with plasma waves; candidate waves will have a frequency below the cyclotron frequency ω_c of the particle, and will be Doppler-shifted into resonance with the cyclotron motion (thereby violating the adiabatic assumption leading to conservation of M, as required for pitch-angle diffusion at constant energy) by the particle's motion along the field line. Electrons can resonate with whistler waves, which propagate along the field lines below the cold (nonrelativistic) electron cyclotron frequency, and protons with ion-cyclotron waves, which propagate similarly below the proton ω_c. For these processes the assumption of diffusion at constant energy is a good approximation; nonetheless, some energy will be exchanged between the particles and the waves, and under conditions of sufficient intensity (above a certain threshold energy) and anisotropy of the energetic particle flux, energy can be systematically transferred to the plasma wave population (Kennel and Petschek 1966; Schulz and Davidson 1988), causing spontaneous excitation of whistler or ion-cyclotron waves. At Uranus and Neptune, in parts of the magnetosphere these conditions were met by electrons above a threshold energy of order keV, and at Uranus intense whistler amplitudes were observed by the PWS (Plasma Wave Subsystem); at Neptune, very low amplitudes were observed, but the amplitude necessary to produce strong pitch-angle diffusion (calculated using formulae of Thorne (1983)) was only about ten times the upper limit on the observed amplitude at $L = 10$ (Krimigis *et al.* 1990). Strong diffusion is the situation when particles are so thoroughly mixed in pitch angle that the distribution nears isotropy, including in the loss cone, so that a fraction of the particles equal to the solid angle in the loss cone divided by 4π steradians is lost to the atmosphere every bounce period; this is as fast as pitch-angle diffusion can proceed (though non-diffusive processes that preferentially scatter particles into the loss cone could conceivably cause faster particle losses). The proton cyclotron frequency was below the lowest frequency observable by the PWS (10 Hz) except for the period of about one hour on each side of closest approach (Gurnett *et al.* 1989), as the equatorial value is only $\frac{200\,\mathrm{Hz}}{L^3}$, so it is not possible to compare the amplitude of these waves with the value required for D_{xx} as modeled. We can, however, compare this value of D_{xx} with the amount necessary under conditions of strong pitch-angle diffusion: in this case,

$$D_{xx}^{SD} \approx \frac{3\alpha_L^2}{\tau_b} \approx \frac{\beta c}{3.6 R_P L^4} \tag{6.11}$$

for large L, where α_L is the equatorial pitch angle at the edge of the loss cone (approximately $\sqrt{\frac{1}{2}L^{-3}}$ radians) (Thorne 1983). For a 2-MeV proton at $L = 6.8$, strong diffusion requires $D_{xx}^{SD} \approx 10^{-4}\mathrm{sec}^{-1}$; the value resulting from the model in chapter 5, and quoted in equation 5.21 as

$$D_{xx}^{P} \approx 10^{-8}\mathrm{sec}^{-1}, \tag{6.12}$$

is four orders of magnitude less than this.

6.4. Summary

The energetic proton population at Neptune displays positive radial phase-space gradients throughout most of the observed region, indicating transport inward from a source outside $L \approx 10$. The radial diffusion coefficient is approximately an order of magnitude less than that for energetic electrons, though its L-dependence is not well constrained; this is consistent with a model for radial diffusion caused by ionospheric winds varying on a timescale much longer than the particles' drift periods. Pitch-angle diffusion is necessary to explain the pitch-angle profiles inside $L \approx 6.8$; the diffusion coefficient is comparable in magnitude to that for radial diffusion in this region, and is much less than the coefficient needed for strong pitch-angle diffusion. Finally, as we approach the planet the energetic proton flux drops below detectability well outside the minimum L-shell of 1989N1, indicating the importance of the high-latitude absorption that extends the radial sweeping range of a satellite in a magnetic field far from aligned with the planetary rotation axis, and of the enhanced high-L absorption peculiar to energetic ions with large gyroradii. This combination of factors enables a single small moon to empty the planet's inner magnetosphere of energetic protons, a situation unique among the planets.

Appendix 1

Closed-Form Calculation of α_g

α_g, the probability that a particle spiraling past a moon will be absorbed by it, was calculated by Paonessa and Cheng (1985) by numerically following the trajectories of particles distributed uniformly in gyrophase as they pass the moon, and noting what fraction of them actually intersect the moon. This appendix presents formulae for direct calculation of this quantity.

Figure A1.1(a) defines the quantities and coordinate system used below: a ring of particles with a common guiding center and gyroradius ρ_g travels past a moon of radius R_m in the $\pm\hat{z}$ direction, with the guiding center passing the moon's center at (positive) impact parameter s. The set of helical trajectories of individual particles (with common local pitch angle α) defines a cylinder; labeling points on this cylinder by axial distance z from point O in figure A1.1(a) and azimuth θ from the $\hat{x}$ axis, the curve of intersection of the moon's surface with the cylinder is defined by

$$\cos\theta = \frac{R_m^2 - \rho_g^2 - s^2 - z^2}{2\rho_g s}. \tag{A1.1}$$

From this we confirm the geometrical conclusions that if $s > R_m + \rho_g$ or $s < \rho_g - R_m$ then there is no solution of equation A1.1, *i.e.*, the cylinder and sphere are disjoint and no particles hit the moon; and if $s < R_m - \rho_g$ then there is a solution for every θ, *i.e.*, at $z = 0$ the section of the cylinder lies within the sphere and all particles hit the moon.

An intermediate case is shown in figure A1.1(b), in which the cylinder is unrolled; the intersection is the heavy solid line. On a diagram such as this, a ring of particles uniformly distributed in gyrophase becomes a uniformly-populated line at a given z; the individual particles' trajectories at a given pitch angle become a family of parallel lines defined by

$$\theta - \theta_0 = \frac{z}{\rho_g}\tan\alpha. \tag{A1.2}$$

Figure A1.1(a)

Geometry for modeling absorption probability during a single bounce of particles past a moon, after Paonessa and Cheng (1985), figure 2(a).

Figure A1.1(b)

Unrolled gyrocylinder and calculation of θ_a. (Example has $\alpha = 45^o$, $\rho_g = s = 0.7\times R_m$.)

Figure A1.1(a)

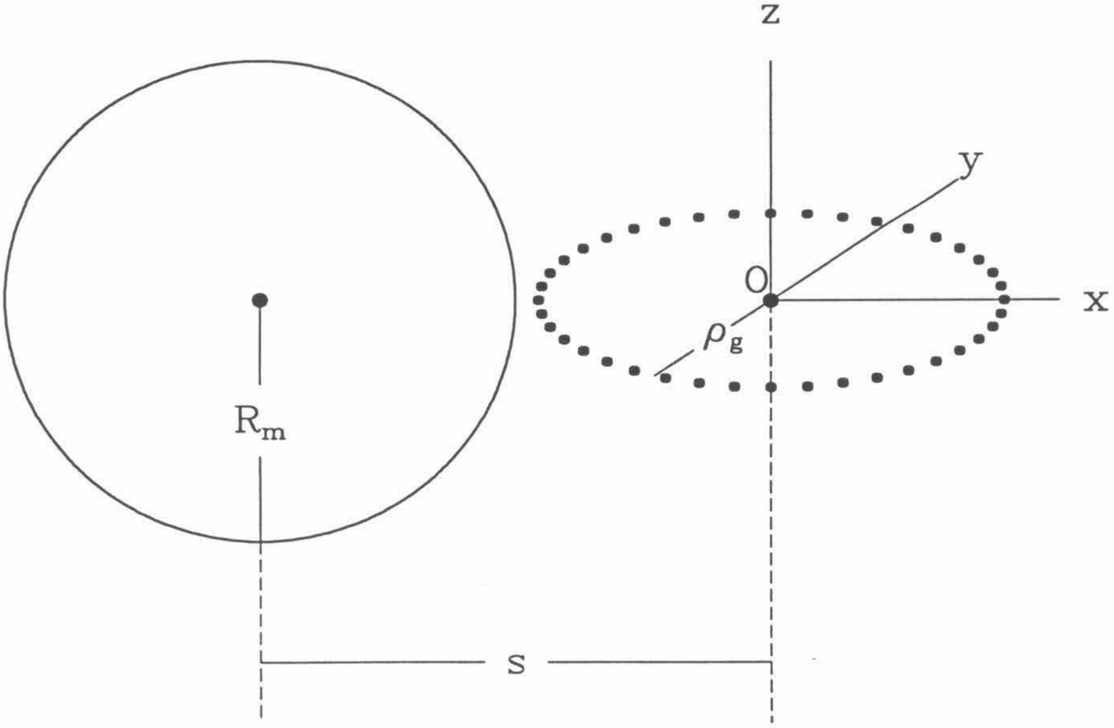

Figure A1.1(b)

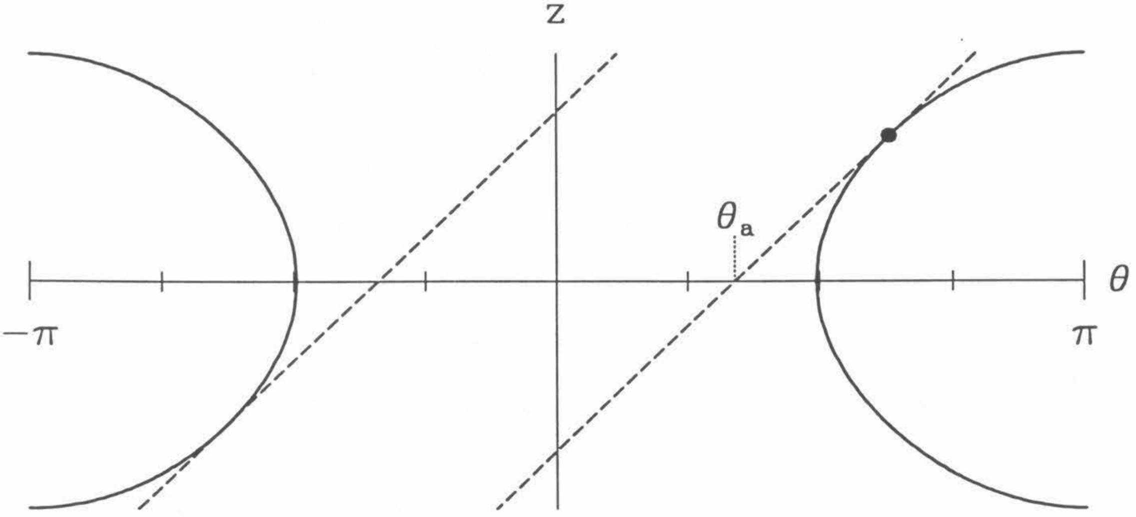

The trajectories that do not hit the moon's surface lie between the two dashed lines in the figure. The θ-intercepts of the boundaries of this subset are extremal values of θ_0 from equation A1.2, subject to equation A1.1: *i.e.*, θ_a in the figure is the smallest value of θ_0 calculated for θ and z lying on the right lobe of the intersection curve. Then the fraction of particles absorbed by the moon is

$$\alpha_g = 1 - \frac{\theta_a}{\pi}. \tag{A1.3}$$

To find θ_a, calculate θ_0 from equations A1.1 and A1.2 as a function of z along the first-quadrant portion of the intersection curve, and find the minimum with respect to z: this is at

$$z^2 = R_m^2 - \rho_g^2 - s^2 + \frac{2\rho_g^2}{\tan^2\alpha} \left[\left[1 + \frac{s^2}{\rho_g^2}\tan^4\alpha - \frac{R_m^2 - \rho_g^2 - s^2}{\rho_g^2}\tan^2\alpha \right]^{1/2} - 1 \right], \tag{A1.4}$$

the position shown by the dot in figure A1.1(b). Then θ_a is the value of θ_0 calculated for this z; if $\theta_a \leq 0$ then $\alpha_g = 1$, otherwise α_g is found from equation A1.3. (By symmetry, this value is correct for particles moving with either helicity, *i.e.*, of either charge, and in either direction of $\hat{z}$, *i.e.*, going up or coming down the magnetic field line.)

Appendix 2
Calculation of τ_{ss}^{-1} for Equatorial Particles

Let $\lambda_M(L)$ be the latitude of the moon corresponding to L for a given leg of the trajectory in figure 4.1. τ_{ss}^{-1} for equatorially-mirroring particles, as calculated by the method discussed in chapter 4, is identically zero (except at the precise L values where the moon crosses the magnetic equator) because the moon is assumed to absorb the particles at a given L as if the moon were always at $\lambda_M(L)$, and equatorial particles, of course, always mirror below this latitude. Actually, for a dipolar magnetic field the moon absorbs particles at latitudes above $\lambda_M(L)$ (in absolute value) when it is less than one effective radius r_m (see equation 4.7) outward from the L-shell of interest, and below $\lambda_M(L)$ when it is less than r_m inward; the range of latitudes absorbed is also slightly extended by the small latitudinal width of the moon. Thus there can be a finite amount of absorption even of equatorial particles, as the time during which the moon is in a position to absorb is not infinitesimal. Because we can write closed expressions for an equatorial particle's trajectory, we can dispense with some of the approximations in chapter 4 and calculate a better value than zero for τ_{ss}^{-1}.

We use a set of equations due to Stoermer (see, *e.g.*, Rossi & Olbert (1970)): let

$$r_S^2 \equiv \frac{|q|k_0}{p} \tag{A2.1}$$

(the Stoermer radius), where p and q are the momentum and charge of the particle, and

$$\gamma_S \equiv -\frac{r_S}{2LR_N}, \tag{A2.2}$$

which for trapped particles is always less than -1; then the path of a particle in polar coordinates (r, λ_m, ϕ) centered on and aligned with the magnetic dipole $\mathbf{k}_0$ will obey

$$r\cos\lambda_m \frac{d\phi}{ds} = \left[\frac{r_S}{r}\right]^2 \cos\lambda_m + \frac{r_S}{r}\frac{2\gamma_S}{\cos\lambda_m} \equiv h\left[\frac{r}{r_S},\lambda_m\right] \tag{A2.3}$$

and

$$\left[\frac{dr}{ds}\right]^2 + r^2\left[\frac{d\lambda_m}{ds}\right]^2 = 1 - \left[h\left(\frac{r}{r_S},\lambda_m\right)\right]^2, \qquad \text{(A2.4)}$$

where s is the arc length along the trajectory. Equation A2.4 implies that h must be between -1 and 1, defining an allowed region for particles in λ_m and r about the drift shell labeled by L (the locus of $h = 0$ is exactly the drift shell, as is implied by the definition of h in equation A2.3). Setting λ_m to zero, we see that at the magnetic equator these bounds in r are given by

$$r_1 = r_S \cdot \left[\gamma_S + \sqrt{\gamma_S^2 + 1}\right] \qquad \text{(A2.5)}$$

where $h = 1$ and

$$r_2 = r_S \cdot \left[-\gamma_S - \sqrt{\gamma_S^2 - 1}\right]. \qquad \text{(A2.6)}$$

where $h = -1$.

Rossi and Olbert (1970) integrate equations A2.3 and A2.4 to get an exact solution for the polar coordinates r and ϕ of an equatorial particle. Using the transformations

$$\cos 2\psi = h(\frac{r}{r_S}) \equiv h(x) \qquad \text{(A2.7)}$$

and

$$k^2 = \frac{2}{1 + \gamma_S^2}, \qquad \text{(A2.8)}$$

they write the trajectory parametrically as

$$\frac{1}{x} = \sqrt{\gamma_S^2 + \cos 2\psi} - \gamma_S \qquad \text{(A2.9)}$$

and

$$\phi = \frac{\gamma_S}{\sqrt{1 + \gamma_S^2}} F(\psi,k) + \psi + \text{const}, \qquad \text{(A2.10)}$$

where

$$F(\psi,k) = \int_0^{\psi} \frac{d\beta}{\sqrt{1 - k^2 \sin^2\beta}} \tag{A2.11}$$

is Legendre's elliptic integral of the first kind. For $1 \geq h \geq -1$, we have $0 \leq \psi \leq \pi/2$ and $r_1 \leq r \leq r_2$ (as defined in equations A2.5 and A2.6) or $x_1 \leq x \leq x_2$ (dividing by r_S). Letting ψ run from 0 to $\pi/2$ traces the outbound half of one cyclotron gyration, say from point d to point c in figure A2.1; the other half is symmetrical in ϕ about the longitude ϕ_d of point d.

To calculate τ_{ss}^{-1} for equatorial particles, we still need a few approximations. For each of the two crossings of the magnetic equator by the moon, we assume L is constant (good since these are near the minimum L values, where dL/dt is small) and that the moon's $d\phi/dt$ is negligible relative to the particle drift velocity ω_d (good by a factor of at least 100 for the particles of interest). Also, we assume that the moon is small relative to the particle's gyroradius (good by a factor of at least 10). Finally, we use an effective radius for the moon: at a given instant the intersection of the moon with the equatorial plane is a circle, and the time-averaged radius of this circle (normalized to r_S) is

$$dx_{me} = \frac{\pi R_m}{4 r_S}. \tag{A2.12}$$

Then at each L we can calculate γ_S and r_S from equations A2.1 and A2.2, and construct a diagram like figure A2.1, placing the moon in turn at the positions of each of its two equatorial crossings at $L_{m1} = 4.4642$ and $L_{m2} = 4.8140$, *i.e.*, at

$$x_{mi} = L_{mi} \frac{R_N}{r_S} = -\frac{1}{2\gamma_S} \frac{L_{mi}}{L} \tag{A2.13}$$

for $i = 1, 2$. The solid and dashed curves define trajectories for particles that just graze the moon at points a and a'; all particles between these two curves will be absorbed in one gyroperiod. We can calculate the gyroperiod exactly by integrating $dt = ds/v$ along the trajectory, but for $\gamma_S < -1.69$ the value differs by less than one percent from

$$\tau_g = \frac{\phi_b - \phi_c}{\omega_d} = \frac{2}{\omega_d} \left| \frac{\gamma_S}{\sqrt{1+\gamma_S^2}} F(\frac{\pi}{2},k) + \frac{\pi}{2} \right|, \tag{A2.14}$$

for ω_d calculated in the guiding center approximation (as equation 3.10), and all particles in

Figure A2.1

Geometry for modeling absorption of equatorial particles; arcs labeled by x and h are of circles concentric with the dipole, and magnetic longitude ϕ increases in the direction from point c to point b. (Example has $\gamma_S = -1.5$.)

Figure A2.1

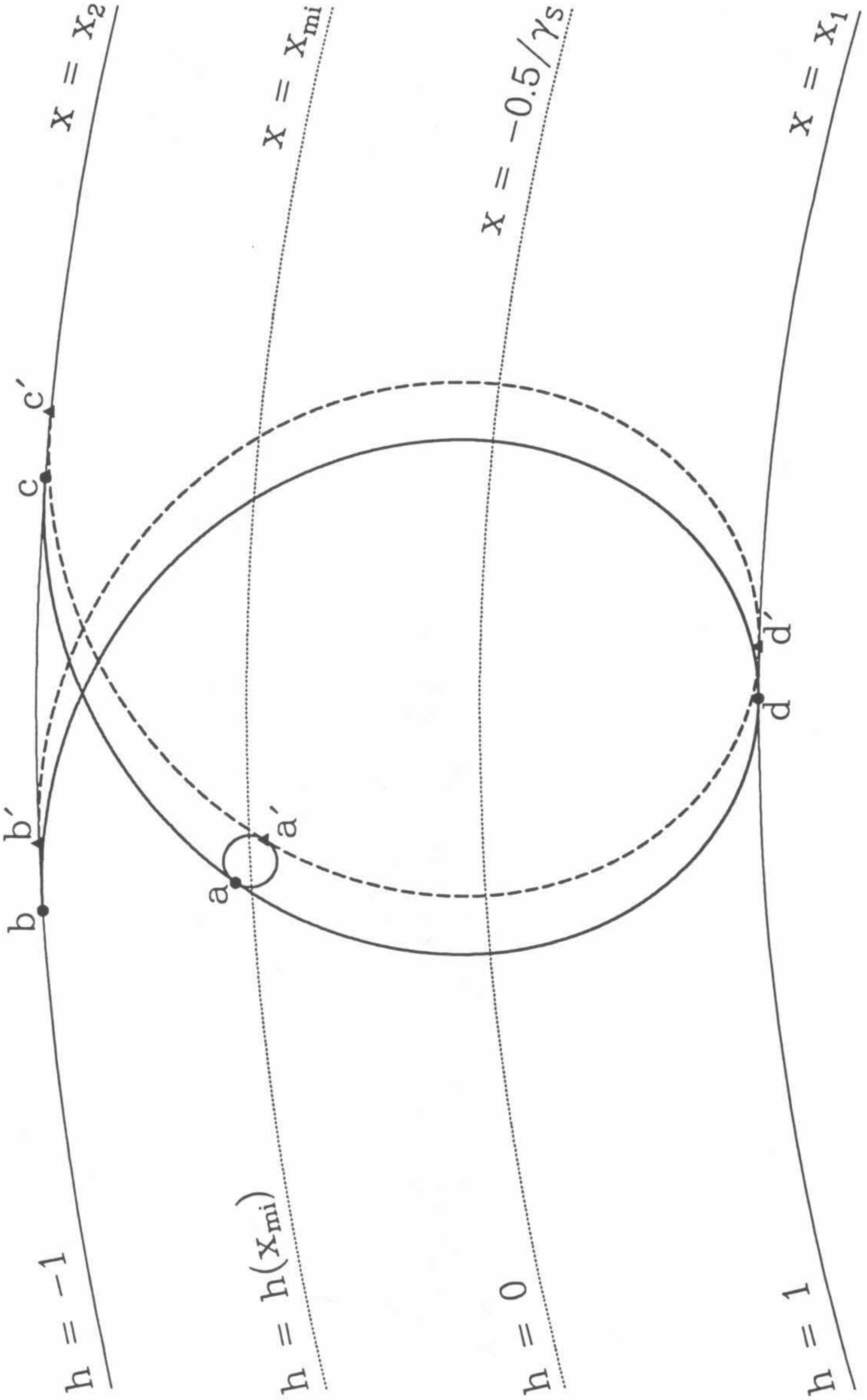

this work have $\gamma_S < -1.75$. The ratio, for the record, is

$$\frac{\tau_g}{\tau_{g\ \mathrm{exact}}} = \frac{-3l}{2\gamma_S r_S (\phi_b - \phi_c)}, \tag{A2.15}$$

where $\phi_b - \phi_c$ is given in equation A2.14 and l is the path length along the curve from point d to point c, given by

$$\frac{l}{r_S} = \frac{1}{r_S}\int_d^c ds = \int_{x_1}^{x_2} \frac{dx}{\sqrt{1-h^2}}$$

$$= \int_{x_1}^{x_2} \frac{x^2 dx}{\sqrt{(x-x_1)(x-x_2)(x-2\gamma_S+x_1)(x+2\gamma_S+x_2)}}. \tag{A2.16}$$

Then in time τ_g, the moon will absorb a fraction

$$f_A = \frac{\phi_d - \phi_{d'}}{2\pi} \tag{A2.17}$$

of the particles at that L; however, if the drift rate is very slow, some of these particles will already have been absorbed in the previous gyroperiod, and only those particles newly drifted into that region will be absorbed, so we use

$$f_A = \frac{\phi_b - \phi_c}{2\pi} = \frac{\omega_d \tau_g}{2\pi} \tag{A2.18}$$

if it is smaller than the value derived from equation A2.17. The absorption takes place only during a fraction

$$f_E = \frac{2R_m}{LR_N \left| \frac{d\lambda_m}{dt} \right| T_m} \tag{A2.19}$$

of one moon synodic period T_m, where $d\lambda_m/dt$ is the moon's angular velocity in magnetic latitude; then, averaging over a synodic period, the particle absorption probability per unit time is

$$\tau_{ss}^{-1} = \frac{f_A f_E}{\tau_g}. \tag{A2.20}$$

All we need now is to calculate $\phi_d - \phi_{d'}$ for equation A2.17.

In figure A2.1, we can use the definition of h in equation A2.3 and the assumption that dx_{me} is small relative to $x_2 - x_1$ to write

$$x_a = x_{mi} - dx_{me}\, h(x_{mi}) \tag{A2.21}$$

$$x_{a'} = x_{mi} + dx_{me}\, h(x_{mi}) \tag{A2.22}$$

and

$$\phi_a - \phi_{a'} = 2\sqrt{1 - h^2(x_{mi})}\frac{dx_{me}}{x_{mi}}, \tag{A2.23}$$

where x_a is the value of x at point a, *etc.* If x_a and $x_{a'}$ are both within the band from x_1 to x_2, we can solve equation A2.9 for ψ_a and $\psi_{a'}$, given equations A2.21 and A2.22. Then we use equation A2.10 to get

$$\phi_a - \phi_d = \frac{\gamma_S}{\sqrt{1+\gamma_S^2}}F(\psi_a, k) + \psi_a \tag{A2.24}$$

and

$$\phi_{a'} - \phi_{d'} = \frac{\gamma_S}{\sqrt{1+\gamma_S^2}}F(\psi_{a'}, k) + \psi_{a'}, \tag{A2.25}$$

and finally we combine equations A2.23 through A2.25 to get a value for $\phi_d - \phi_{d'}$ to put into equation A2.17 for f_A, which is the last quantity needed to find τ_{ss}^{-1} from equation A2.20.

For large gyroradii, the L regions swept during the two equator crossings overlap; in the overlap region we add the values of τ_{ss}^{-1}. Figure A2.2 plots τ_{ss}^{-1} for three values of M in the range of interest, showing the width of the swept regions increasing with M. By requiring that x_a and $x_{a'}$ both be within the region from x_1 to x_2, *i.e.*, that the moon be entirely within the gyrocircle, we ignore partial sweeping in $R_m/R_N = 0.016$ units of L on each edge of each swept zone. The substitution of equation A2.18 for equation A2.19 is only operative within a comparable width in L for the lowest of the Ms shown, cutting the heights of the peaks at the edges of the swept zones by up to a third.

Figure A2.2

Inverse satellite sweeping lifetimes due to 1989N1 for equatorial particles with (a) $M = 10^{3.6}$ MeV/G, (b) $M = 10^{4.0}$ MeV/G, and (c) $M = 10^{4.4}$ MeV/G.

Figure A2.2

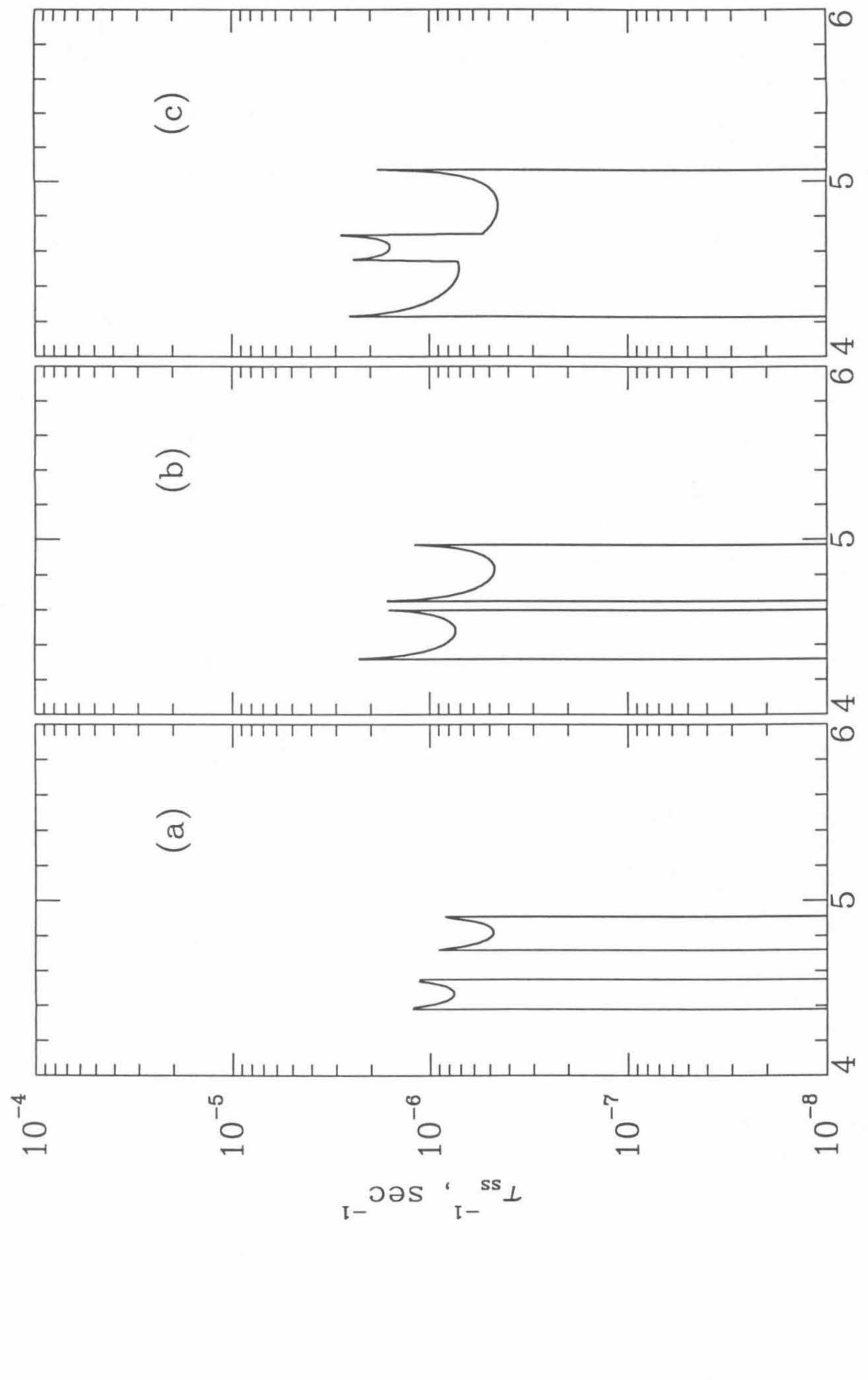

Appendix 3
Sensitivity of Models to Fit Parameters

3.1. Statistical Errors

In a fitting process that attempts to reproduce observations by varying a set of parameters of a model, one can usually obtain "error bars" on the parameters that give the best fit to the data by taking σ_k^2 for parameter p_k to be the kth diagonal element of the inverse of the curvature matrix:

$$\sigma_k^2 = \left[\alpha^{-1}\right]_{kk} \tag{A3.1}$$

for

$$\alpha_{ij} = \frac{1}{2}\frac{\partial^2 \chi^2}{\partial p_i \partial p_j}; \tag{A3.2}$$

then changing the model by σ_k either way from the best-fit value of p_k should increase χ^2 by approximately one (Bevington 1969). This can be interpreted as stating that, for a large ensemble of observers making the same set of measurements, with observed values (here, numbers of counts) distributed around the true value (expected number of counts) according to an appropriate distribution function (Poisson), and each fitting a model to his own set of measurements, at least 68% of the observers would derive a value for p_k within σ_k of the true value (Gehrels 1986).

However, this definition of the "one-sigma confidence limits" on the parameters assumes that one has a model which fits the data well enough that the biggest deviations from the observations will be due to statistical fluctuations in the observations themselves; if this is the case, then the value of χ^2 should be close to the expected value $N - n$, where there are N data points and n fit parameters. This is not the case for the models presented in this thesis; $N = 210$ for the subset of the observations selected for fitting, and $n = 3$ or 7 respectively for models with radial diffusion only or radial and pitch angle diffusion, but the values of χ_P^2 (from equation 5.3) calculated for the two best-fit models are 753 and 1057 respectively. Clearly systematic effects dominate, as can be seen by a glance at figures 5.3 and 5.7: the deviations of the observed data points from the model points are not randomly up or down, but rather in certain regions the model systematically passes either above or below the observations. Several attempts were made to find a way to assign a value to systematic errors and include them in calculating a revised χ^2 from which more realistic errors on the parameters could be derived, such as adding an estimated systematic error in quadrature with a Gaussian approximation of the statistical errors; these led to very different "best fits" in some cases, as the structure of the observations in areas where the models in chapter 5 are actually able to do a good job of matching them was smeared out by the added errors to the point that the fit was equally bad everywhere. Thus in this appendix the observations are compared with several models differing in one parameter at a time from the best-fit models of chapter 5 by showing these models as an envelope around the nominal one, and thus showing which parameters' values are most tightly constrained by which subset of the observations. This presentation of alternative models allows one to distinguish between constraints that reflect qualitative features of the data, such as the lack of a sharp pitch-angle anisotropy in the vicinity of the roll maneuver, and ones that simply amount to making the best of a bad fit. This distinction is the reason that the model with pitch-angle diffusion is claimed to be an improvement over the one without, despite its higher value of χ_P^2.

3.2. Radial-Diffusion Models

Figures A3.1 show the dependence of the radial-diffusion model on the normalization of D_{LL}, for one of the five energy bins (the others are qualitatively similar), and figures A3.2 show the dependence on the exponent of D_{LL} versus L. Generally, the models differ most at low Ls, where the differing values of D_{LL} resulting from different normalizations and L-dependences for it lead to large differences in the sharpness of the downturns in phase-space density with decreasing L; since the LET C data set samples the lowest Ls, it is most strongly affected, and therefore it most strongly constrains the fit. Unfortunately, as noted in

Figure A3.1

Fluxes in the 2.1-2.9 MeV energy bin, for radial-diffusion models differing in $D_{LL}(L=8)$; models are plotted as lines, points with error bars are observations. Each point, of model or observation, is normalized by the value at the same point of the model of figures 5.3 and 5.4; the models plotted have $D_{LL}(L=8)$ that is 1/10, 1/5, 1/3, 1/2, 1, 2, 3, 5, and 10 times that of the nominal model (1.7×10^{-8} sec^{-1}), in order from the dashed line to the dotted one. The subfigures are (a) LET C inbound; (b) LET C outbound; (c) LET D inbound; and (d) LET D outbound, as in figures 5.3, 5.7, and 5.9.

Figure A3.2

Fluxes in the 2.1-2.9 MeV energy bin, for radial-diffusion models differing in the exponent of D_{LL} versus L, plotted as in figures A3.1. For $D_{LL} \propto L^{\beta}$, the models plotted have $\beta = 3$, 5, 8, 10, 12, 15, and 17, in order from the dashed line to the dotted one.

Figure A3.3

LET C outbound fluxes for four energy bins, for the radial-diffusion models of figure A3.2. The subfigures are (a) 1.9-2.1 MeV, (b) 2.1-2.9 MeV, (c) 3.2-3.7 MeV, and (d) 3.7-4.3 MeV.

Figure A3.1

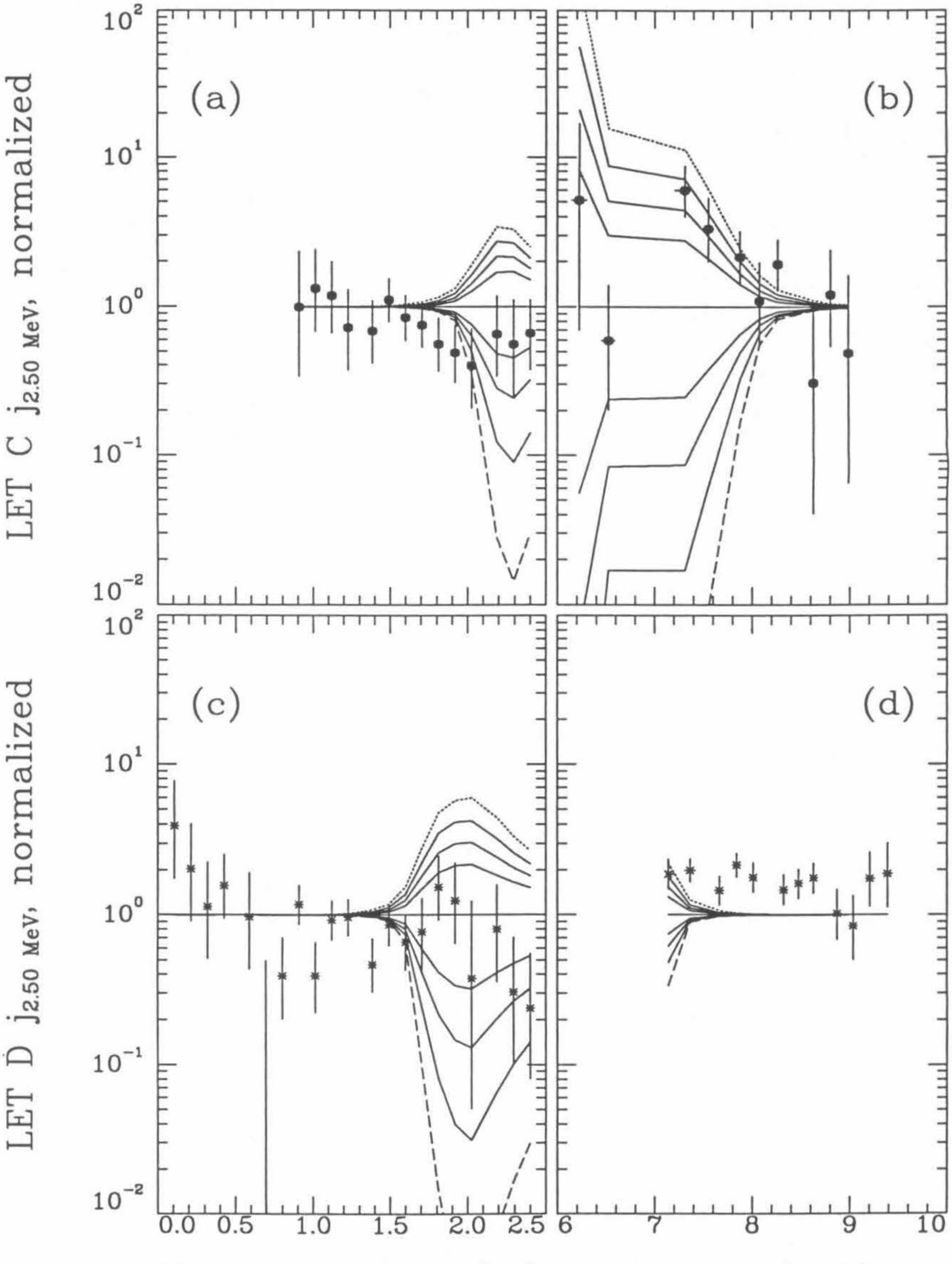
LET C $j_{2.50\ \mathrm{MeV}}$, normalized
LET D $j_{2.50\ \mathrm{MeV}}$, normalized
(a)
(b)
(c)
(d)
10^2
10^1
10^0
10^{-1}
10^{-2}
0.0
0.0
0.5
1.0
1.5
2.0
2.5
6
7
8
9
10
Hr. of day 237 (in)
I8E1 L (out)

Figure A3.2

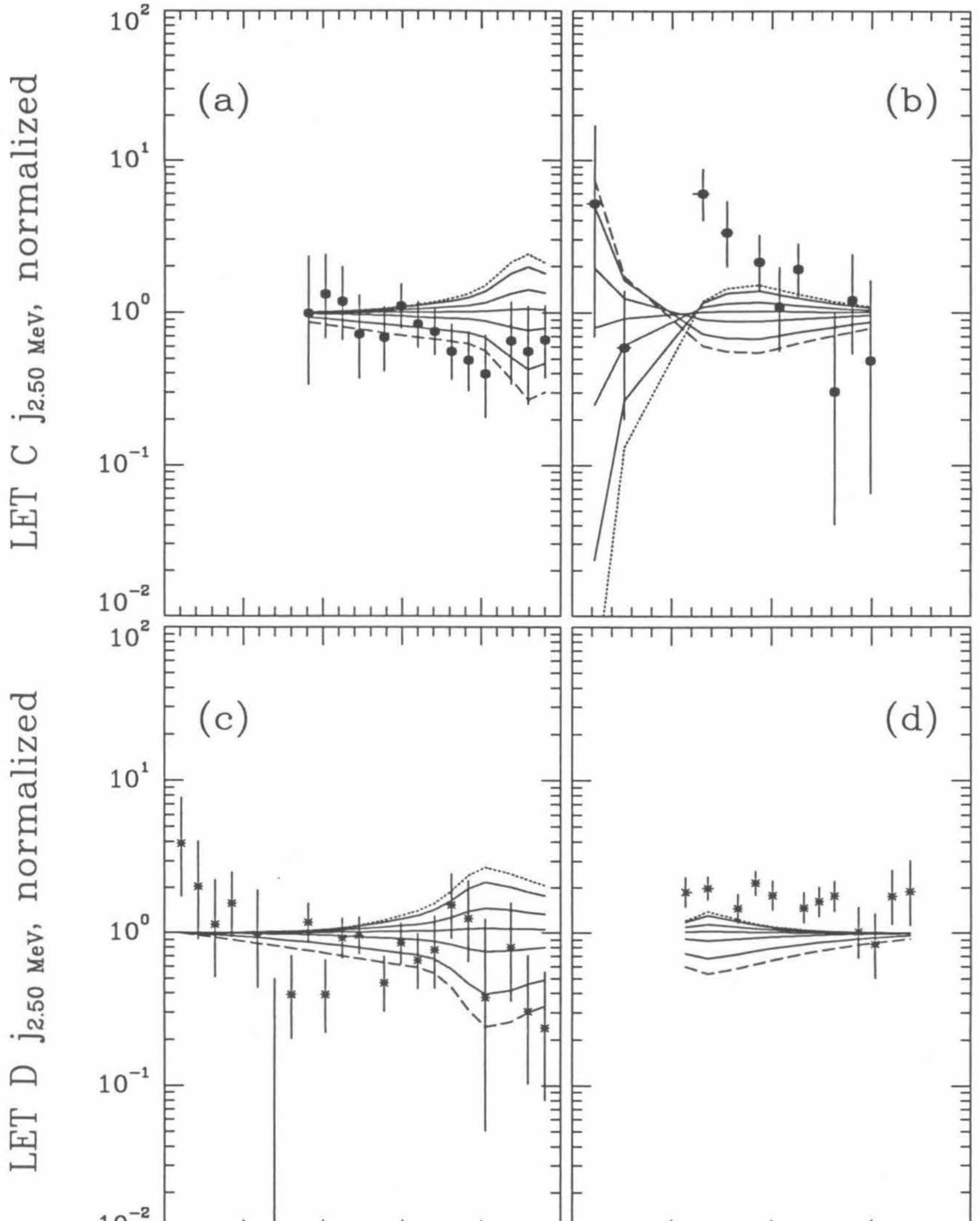
LET C $j_{2.50\ \mathrm{MeV}}$, normalized
LET D $j_{2.50\ \mathrm{MeV}}$, normalized
(a)
(b)
(c)
(d)
10^2
10^1
10^0
10^{-1}
10^{-2}
0.0
0.5
1.0
1.5
2.0
2.5
6
7
8
9
10
Hr. of day 237 (in)
I8E1 L (out)

Figure A3.3

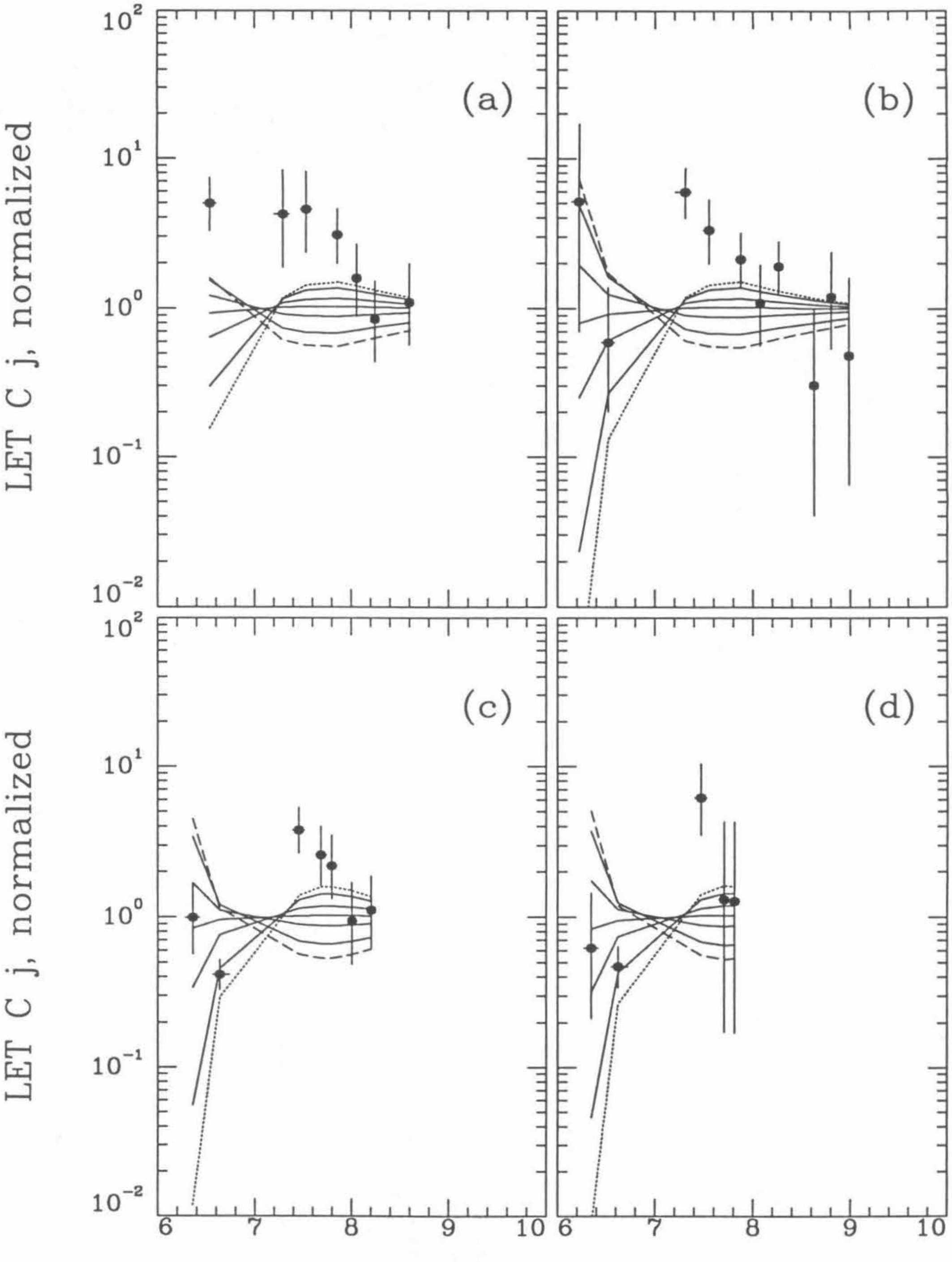
LET C j, normalized
LET C j, normalized
I8E1 L (out)
I8E1 L (out)
(a)
(b)
(c)
(d)
10^2
10^1
10^0
10^{-1}
10^{-2}
6
7
8
9
10

chapter 5, this is the subset of the observations worst fit by the model; the observations also have some of the worst statistics. From figure A3.1(b) it might appear that a substantial increase in the normalization of D_{LL}, as represented by the dotted line, would improve the fit at all but one of the points in this figure; looking at the LET C outbound observations in other energy bins, however, as presented in figures A3.3, we can see that this is just due to the small number of counts in the lowest-L point in the 2.1-2.9 MeV energy bin. The models presented in figures A3.3 are the same as those in figures A3.2, which differ from the nominal model in the exponent of the power-law dependence of D_{LL} on L; from them we can see that the model is not sensitive enough to this parameter that the observations constrain its value very tightly. As noted above, it is difficult to quote an error margin on parameters in the absence of a good overall fit; let us take as our criterion that a value of a parameter is consistent with the observations if a model that uses the revised value no more than doubles the size of the logarithmic residual of the worst-fit points in the region of the model sensitive to that parameter. That is, renormalizing figures like A3.1 to A3.3 so that the model with the revised parameter is the straight line at 10^0 results in an envelope around the observed points that is no more than twice the size (on the logarithmic scale, in the most sensitive region) of one that encloses them in a figure normalized to the nominal model. With this criterion, figure A3.1 shows that models varying the normalization of D_{LL} up or down a factor of about 3 remain consistent with the observations. Figures A3.2 and A3.3, however, show that a wide range of exponents result in models consistent with the observations, perhaps from 5 to 15. In neither case does varying these parameters allow the model to reproduce the lack of a jump in the observed flux across the roll maneuver; this is the motivation for introduction of pitch-angle diffusion in §5.2.

Figures A3.4 show the dependence of the model on n, the exponent in the pitch-angle distribution at $L = 10$. This parameter is constrained by sections of the observations, notably the early inbound data and the more distant LET D outbound data, that sample the flat parts at high L of the phase-space density curves of figure 5.4(a) and that are thus little affected in the model by the changes above in D_{LL}. Conversely, this parameter is therefore fairly well-constrained by the observations, which are fit by the nominal model better in these areas than in the subset that constrains D_{LL} above, and we can conclude that the pitch-angle distribution really is nearly isotropic near $L = 10$, as in that model; using the criterion for consistency described above, n should be between about 0 and 1.2.

3.3. Combined Radial- and Pitch-Angle-Diffusion Models

The dependence of the model of §5.2, with pitch-angle diffusion added to radial diffusion, on the two parameters of D_{LL} is shown in figures A3.5, A3.6, and A3.7, which show roughly the same range of models as figures A3.1, A3.2, and A3.3 respectively. (The models with very low D_{LL} that drop off the bottom of the scale in figure A3.5(c) are an artifact of the calculation, which cannot reproduce extreme pitch-angle anisotropies at high values of x, as detailed in appendix 4.) The dependence of this model on these parameters is very similar to that of the model with radial diffusion only; the lack of an observed jump in flux across the roll maneuver at $L \approx 7$ in the LET C outbound data is better reproduced here than in that model, of course, since pitch-angle diffusion is allowed, but the range of parameters consistent with the data is most sensitive to the lowest-L points rather than to the jump or absence thereof, and thus the parameters are comparably constrained: normalization of D_{LL} is correct within about a factor of 3, and the exponent of its L-dependence is probably between 5 and 15.

The dependence on the pitch-angle parameter n, shown in figure A3.8, is also similar to that of the previous model, except for an increased sensitivity at L less than about 8 in the outbound data due to the cancellation of different amounts of pitch-angle anisotropy in models with different n at $L = 10$, once pitch-angle diffusion cuts in. The nominal model does not produce much difference in the simulated fluxes relative to the radial-diffusion-only model, in the regions most sensitive to n; thus by the criterion above we can again say that n at the boundary should be between about 0 and 1.2.

Because equation 5.9 is linear in f, the dependence of the models on the normalization of the phase-space density at the $L = 10$ boundary is trivial; this leaves the three parameters involved in pitch-angle diffusion: the normalization of D_{xx}, and the location L_0 and width ΔL of its onset. Figures A3.9, A3.10, and A3.11 show the dependence of the model on these parameters. Only the LET C outbound model fluxes across the roll maneuver show much sensitivity to the normalization of D_{xx}, but they constrain it rather tightly: too much or

Figure A3.4

Fluxes in the 2.1-2.9 MeV energy bin, for radial-diffusion models differing in the pitch-angle exponent n of equation 5.2, plotted as in figures A3.1. The models plotted have $n = 0$, 1/4, 1/2, 1, 2, 3, and 4 times that of the nominal model (0.44), in order from the dashed line to the dotted one.

Figure A3.4

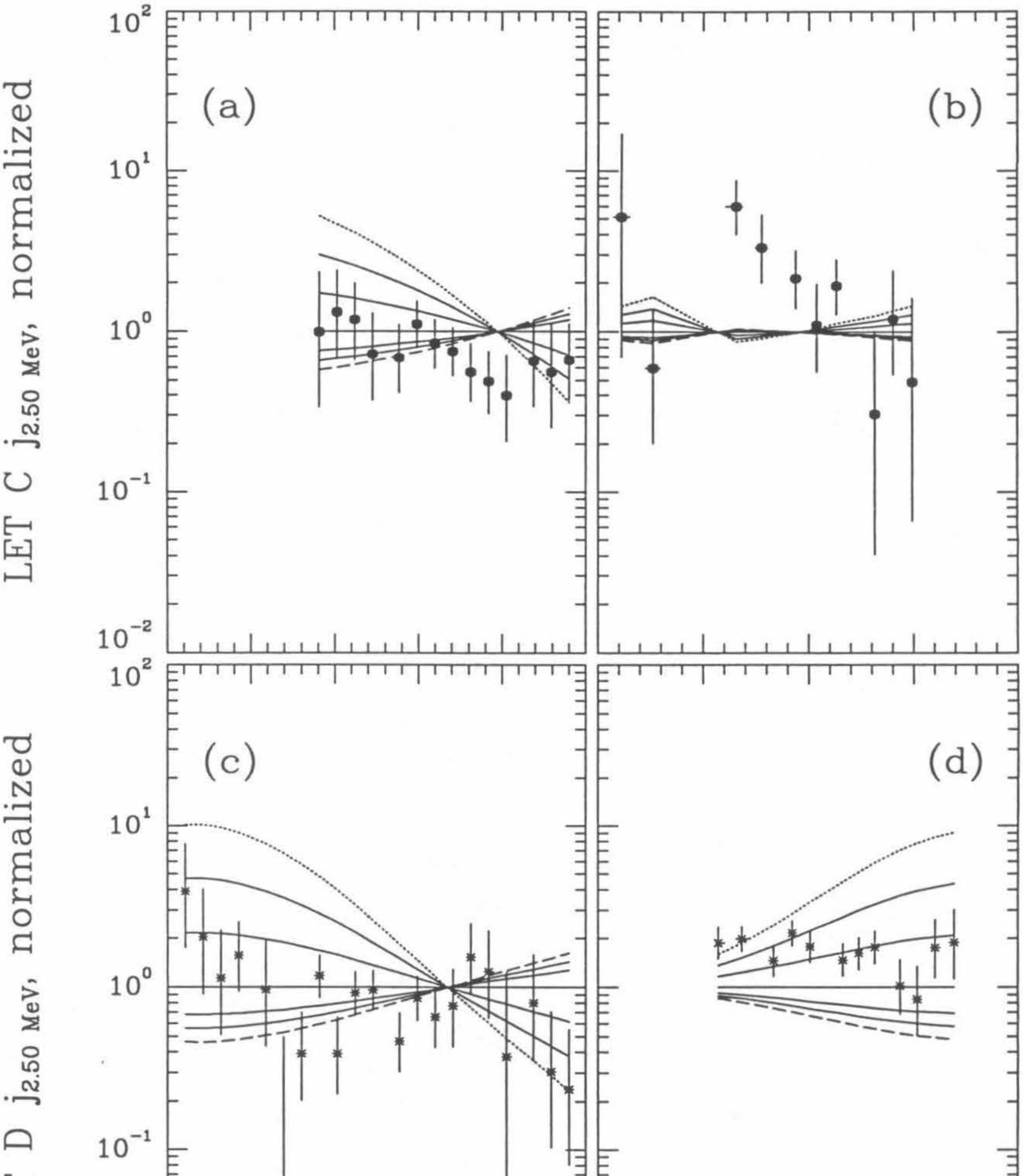
LET C $j_{2.50\ \mathrm{MeV}}$, normalized
LET D $j_{2.50\ \mathrm{MeV}}$, normalized
(a)
(b)
(c)
(d)
10^2
10^1
10^0
10^{-1}
10^{-2}
0.0 0.0 0.5 1.0 1.5 2.0 2.5
6 7 8 9 10
Hr. of day 237 (in)
I8E1 L (out)

Figure A3.5

Fluxes in the 2.1-2.9 MeV energy bin, for models with combined radial and pitch-angle diffusion differing in $D_{LL}(L=8)$, plotted as in figures A3.1 but normalized relative to the model of figures 5.6 and 5.7. The models plotted have $D_{LL}(L=8)$ that is 1/10, 1/5, 1/3, 1/2, 1, 2, 3, 5, and 10 times that of the nominal model (1.2×10^{-8} sec^{-1}), in order from the dashed line to the dotted one.

Figure A3.6

Fluxes in the 2.1-2.9 MeV energy bin, for combined-diffusion models differing in the exponent of D_{LL} versus L, plotted as in figures A3.5. For $D_{LL} \propto L^{\beta}$, the models plotted have $\beta = 3, 5, 8, 10, 12, 15$, and 17, in order from the dashed line to the dotted one.

Figure A3.7

LET C outbound fluxes for four energy bins, for the combined-diffusion models of figure A3.6. The subfigures are (a) 1.9-2.1 MeV, (b) 2.1-2.9 MeV, (c) 3.2-3.7 MeV, and (d) 3.7-4.3 MeV.

Figure A3.5

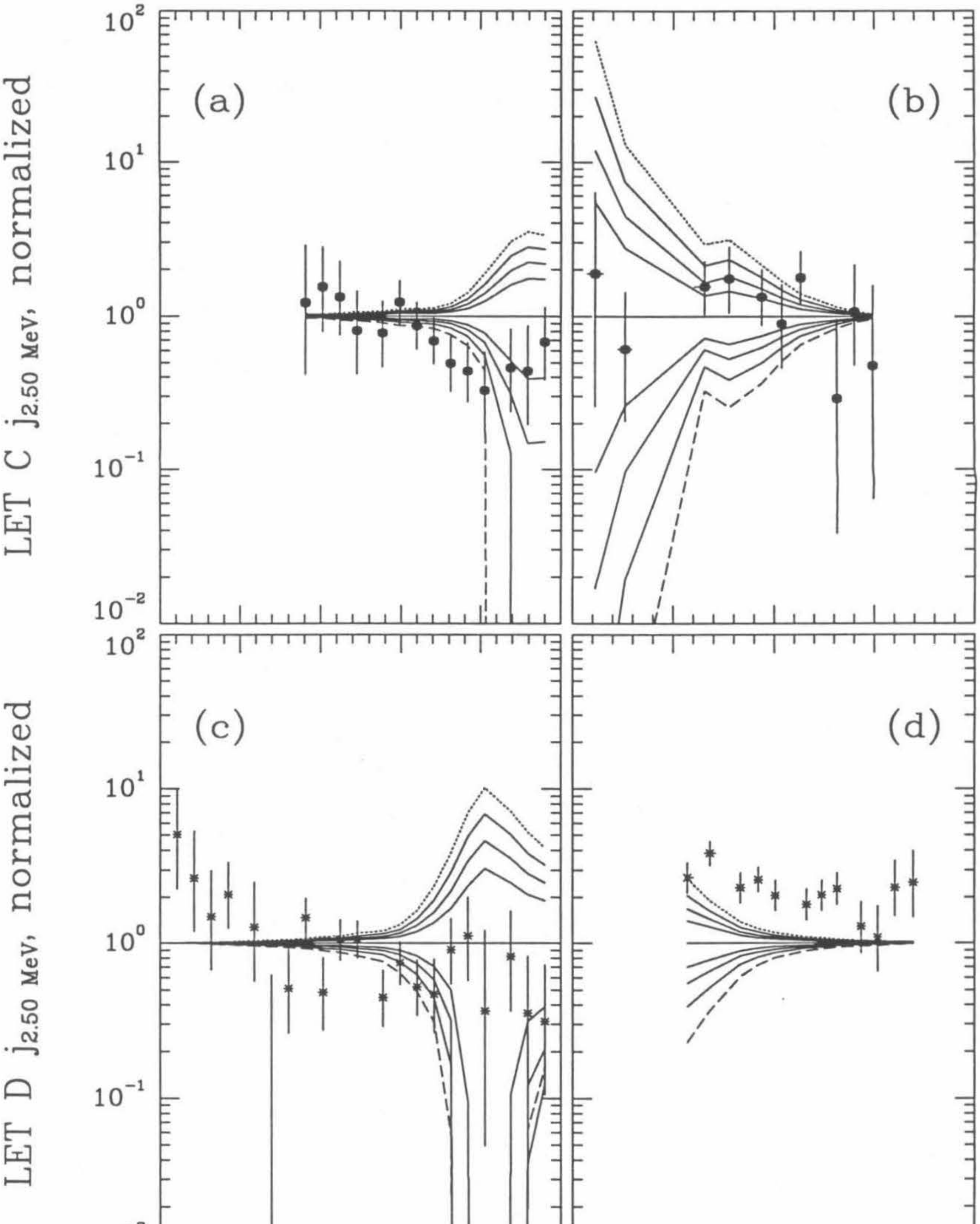
LET C $j_{2.50\ \mathrm{MeV}}$, normalized
LET D $j_{2.50\ \mathrm{MeV}}$, normalized
(a)
(b)
(c)
(d)
10^{2}
10^{1}
10^{0}
10^{-1}
10^{-2}
0.0
0.5
1.0
1.5
2.0
2.5
6
7
8
9
10
Hr. of day 237 (in)
I8E1 L (out)

Figure A3.6

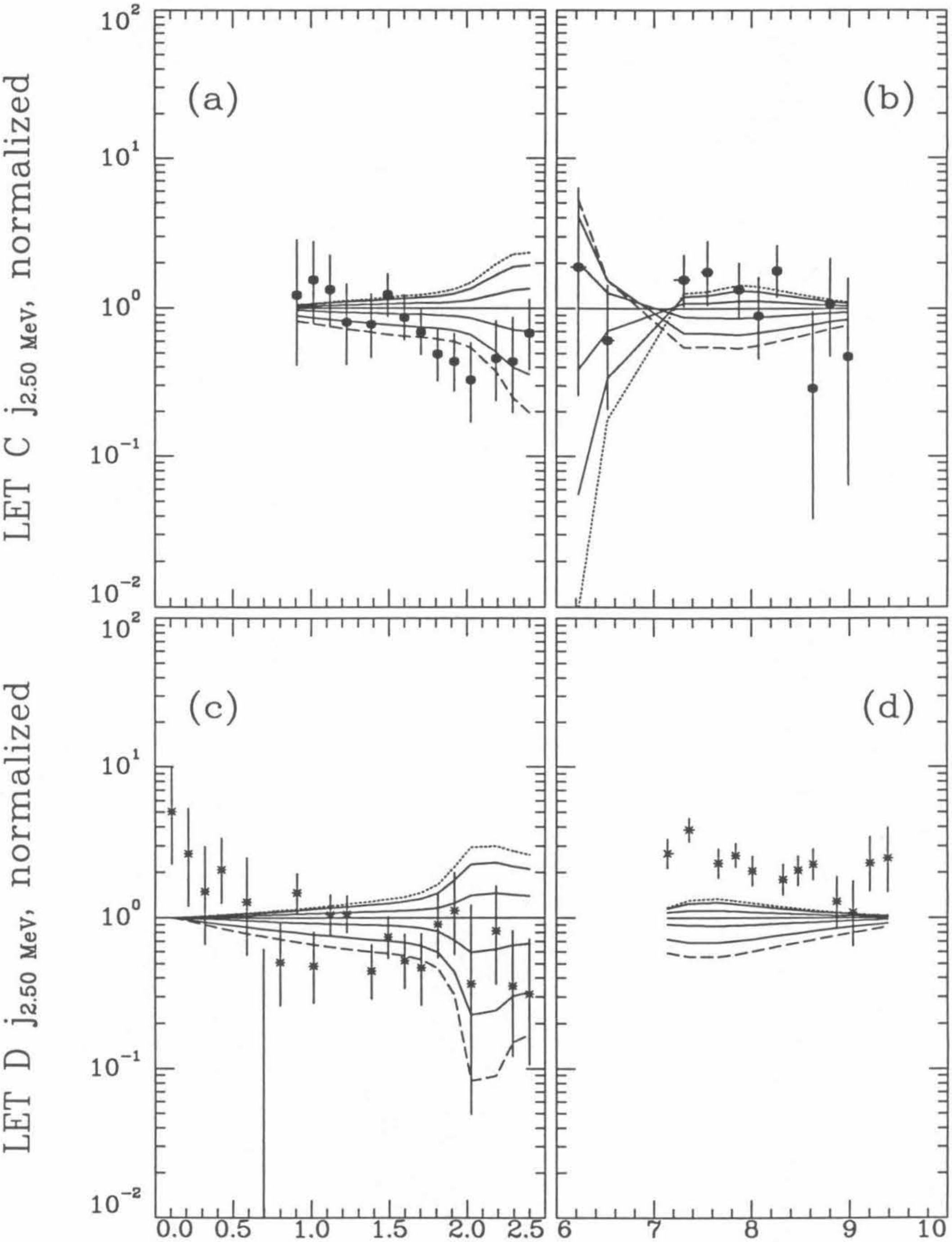
(a)
(b)
(c)
(d)
LET C $j_{2.50\ \mathrm{MeV}}$, normalized
LET D $j_{2.50\ \mathrm{MeV}}$, normalized
10^{2}
10^{1}
10^{0}
10^{-1}
10^{-2}
0.0
0.5
1.0
1.5
2.0
2.5
6
7
8
9
10
Hr. of day 237 (in)
I8E1 L (out)

Figure A3.7

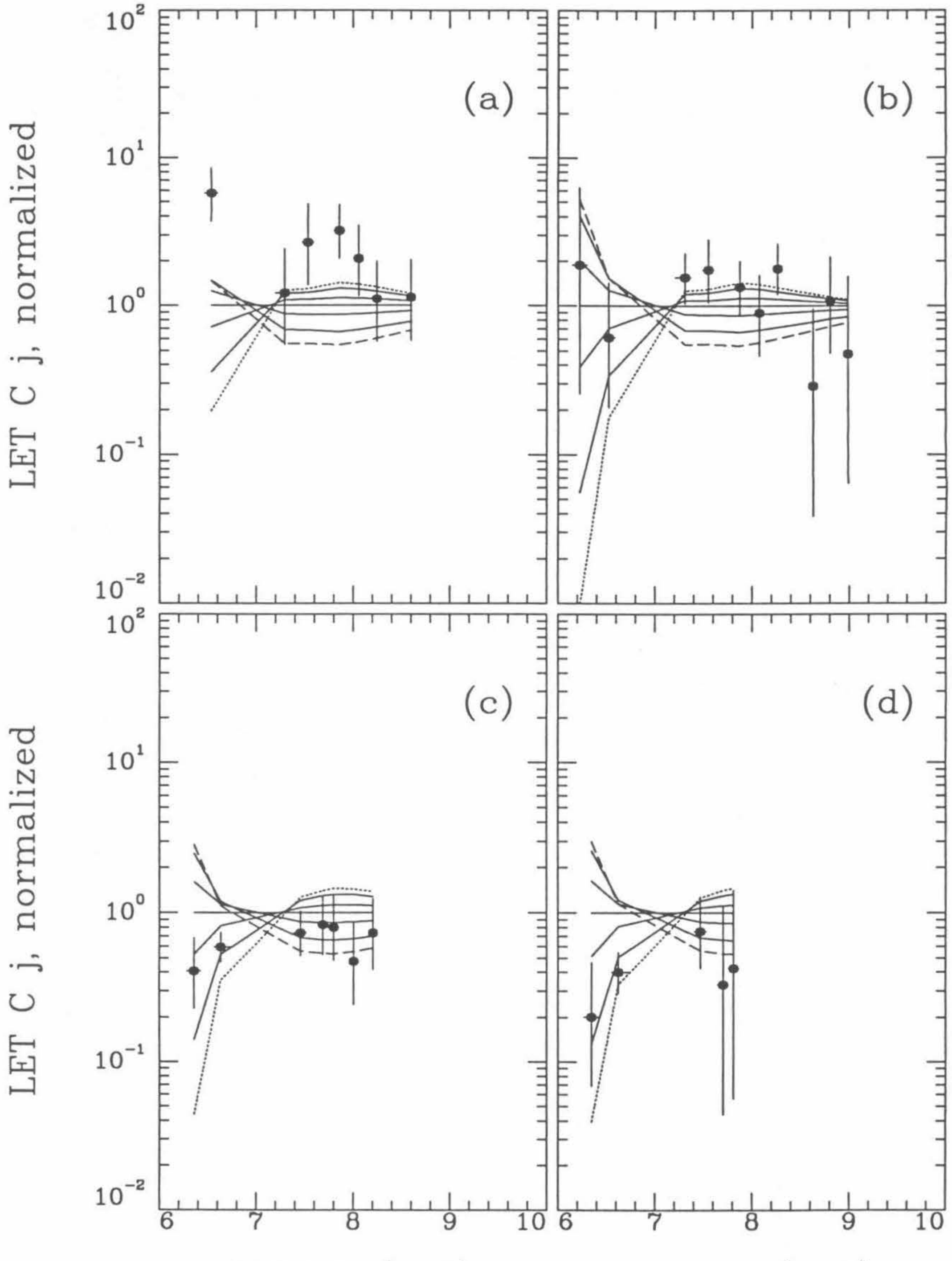
(a)
(b)
(c)
(d)
LET C j, normalized
LET C j, normalized
10^2
10^1
10^0
10^{-1}
10^{-2}
6
7
8
9
10
I8E1 L (out)
I8E1 L (out)

Figure A3.8

Fluxes in the 2.1-2.9 MeV energy bin, for combined-diffusion models differing in the pitch-angle exponent n of equation 5.2, plotted as in figures A3.5. The models plotted have n = 0, 1/4, 1/2, 1, 2, 2 1/2, and 3 times that of the nominal model (0.63), in order from the dashed line to the dotted one.

Figure A3.8

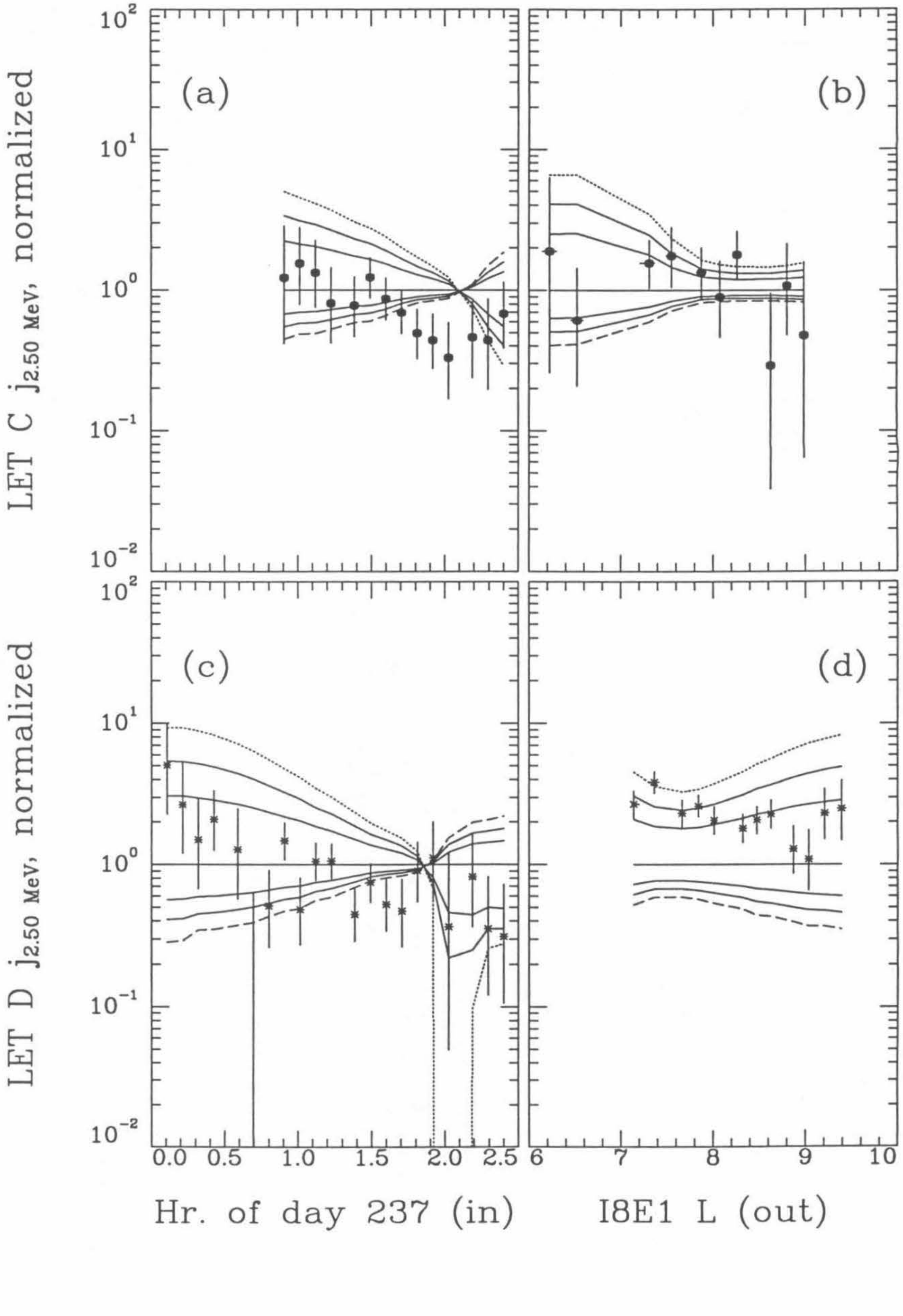
LET C $j_{2.50\ \mathrm{MeV}}$, normalized
LET D $j_{2.50\ \mathrm{MeV}}$, normalized
(a)
(b)
(c)
(d)
10^2
10^1
10^0
10^{-1}
10^{-2}
0.0
0.5
1.0
1.5
2.0
2.5
6
7
8
9
10
Hr. of day 237 (in)
I8E1 L (out)

Figure A3.9

Fluxes in the 2.1-2.9 MeV energy bin, for combined-diffusion models differing in D_{xx}, plotted as in figures A3.5. The models plotted have D_{xx} = 1/10, 1/5, 1/3, 1/2, 1, 2, 3, 5, and 10 times that of the nominal model (1.2×10^{-9} sec^{-1}), in order from the dashed line to the dotted one.

Figure A3.10

Fluxes in the 2.1-2.9 MeV energy bin, for combined-diffusion models differing in location of pitch-angle diffusion turn-on L_0, plotted as in figures A3.5. The models plotted have L_0 = 6.0, 6.4, 6.8, 7.2, and 7.6, in order from the dashed line to the dotted one.

Figure A3.11

Fluxes in the 2.1-2.9 MeV energy bin, for combined-diffusion models differing in width of pitch-angle diffusion turn-on ΔL, plotted as in figures A3.5. The models plotted have ΔL = 1/3, 1/2, 1, 2, and 3 times that of the nominal model, in order from the dashed line to the dotted one.

Figure A3.9

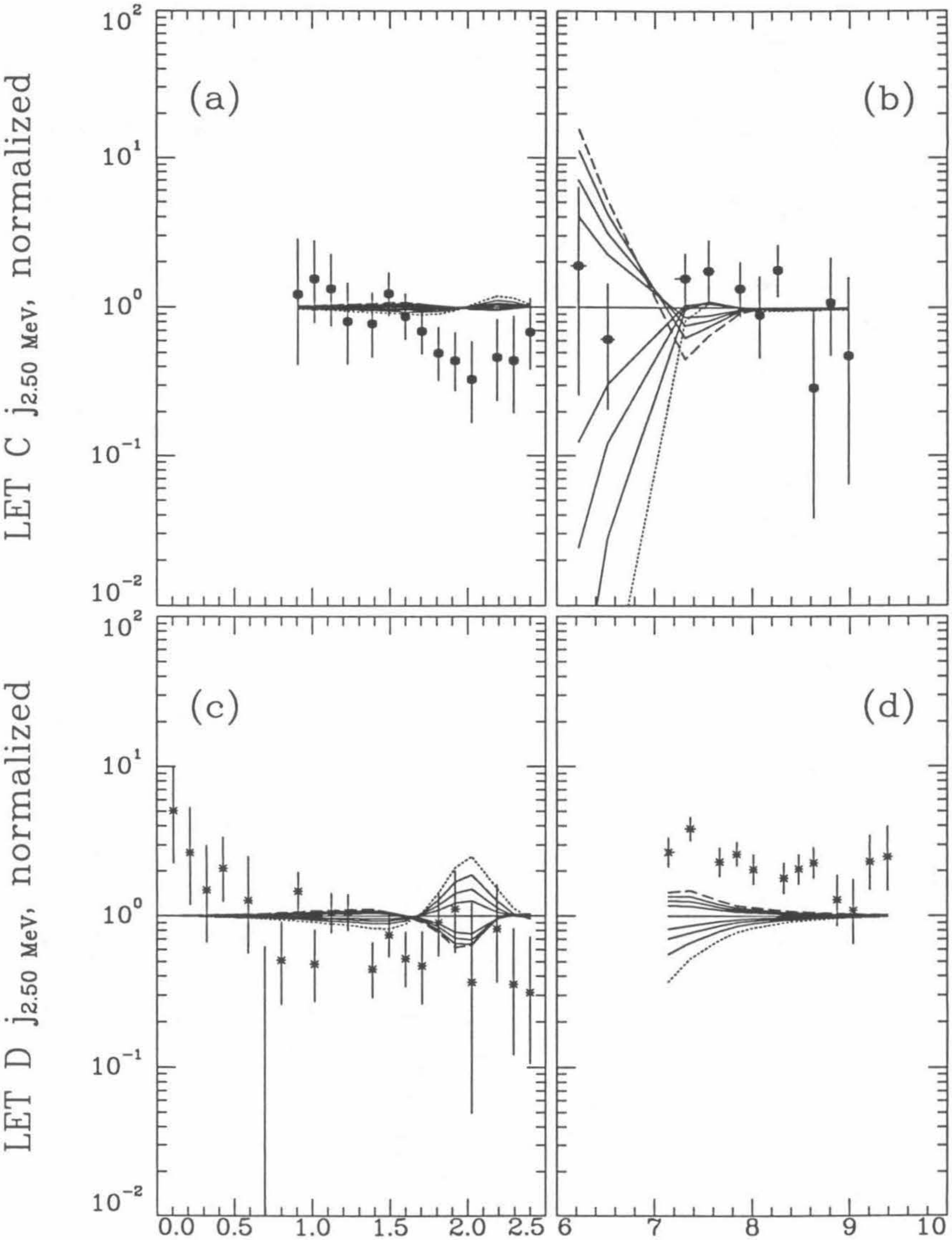
LET C $j_{2.50\ \mathrm{MeV}}$, normalized
LET D $j_{2.50\ \mathrm{MeV}}$, normalized
(a)
(b)
(c)
(d)
10^{2}
10^{1}
10^{0}
10^{-1}
10^{-2}
0.0
0.0
0.5
1.0
1.5
2.0
2.5
6
7
8
9
10
Hr. of day 237 (in)
I8E1 L (out)

Figure A3.10

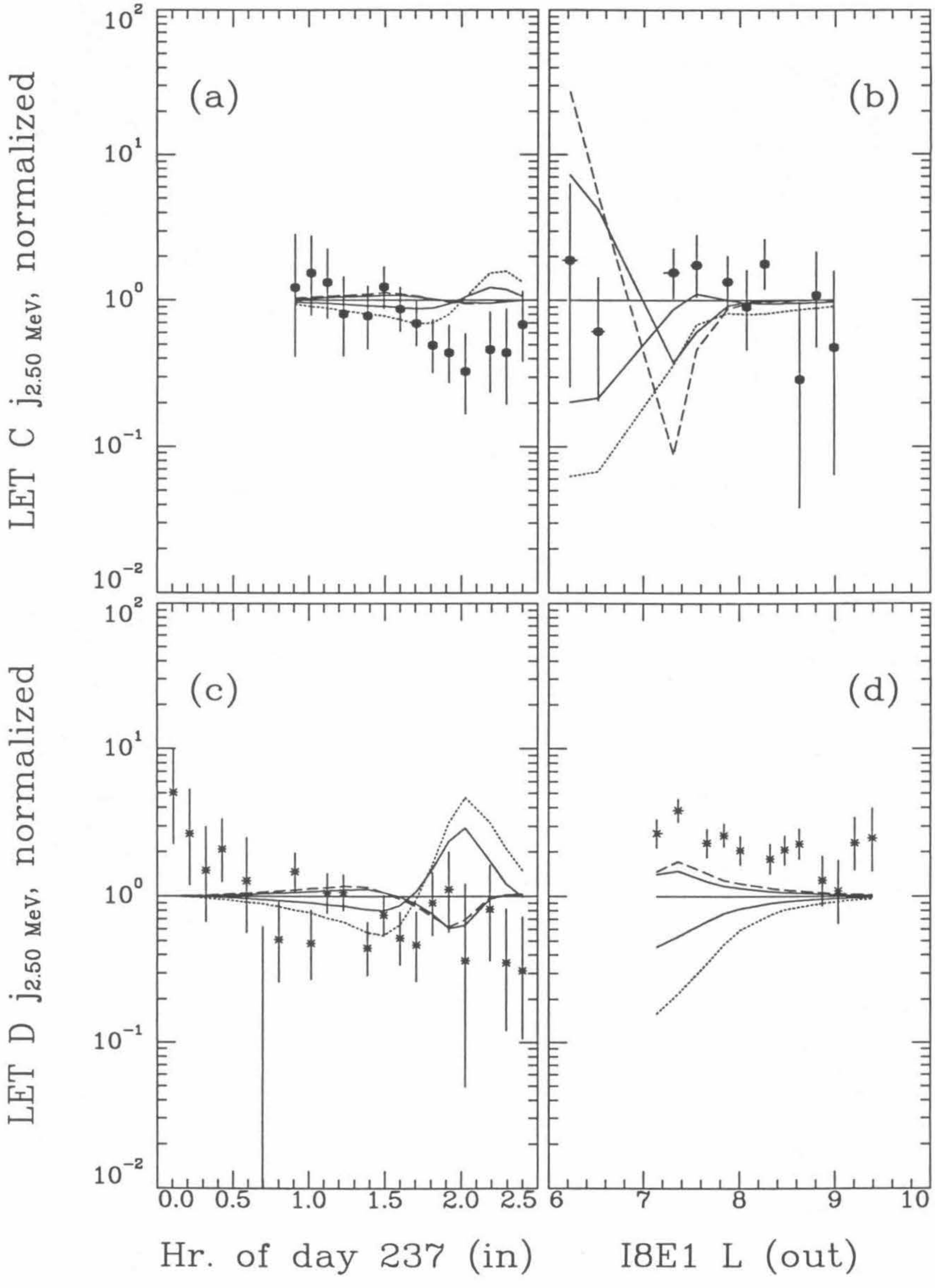
LET C $j_{2.50\ \mathrm{MeV}}$, normalized
LET D $j_{2.50\ \mathrm{MeV}}$, normalized
(a)
(b)
(c)
(d)
10^2
10^1
10^0
10^{-1}
10^{-2}
0.0
0.0
0.5
1.0
1.5
2.0
2.5
6
7
8
9
10
Hr. of day 237 (in)
I8E1 L (out)

Figure A3.11

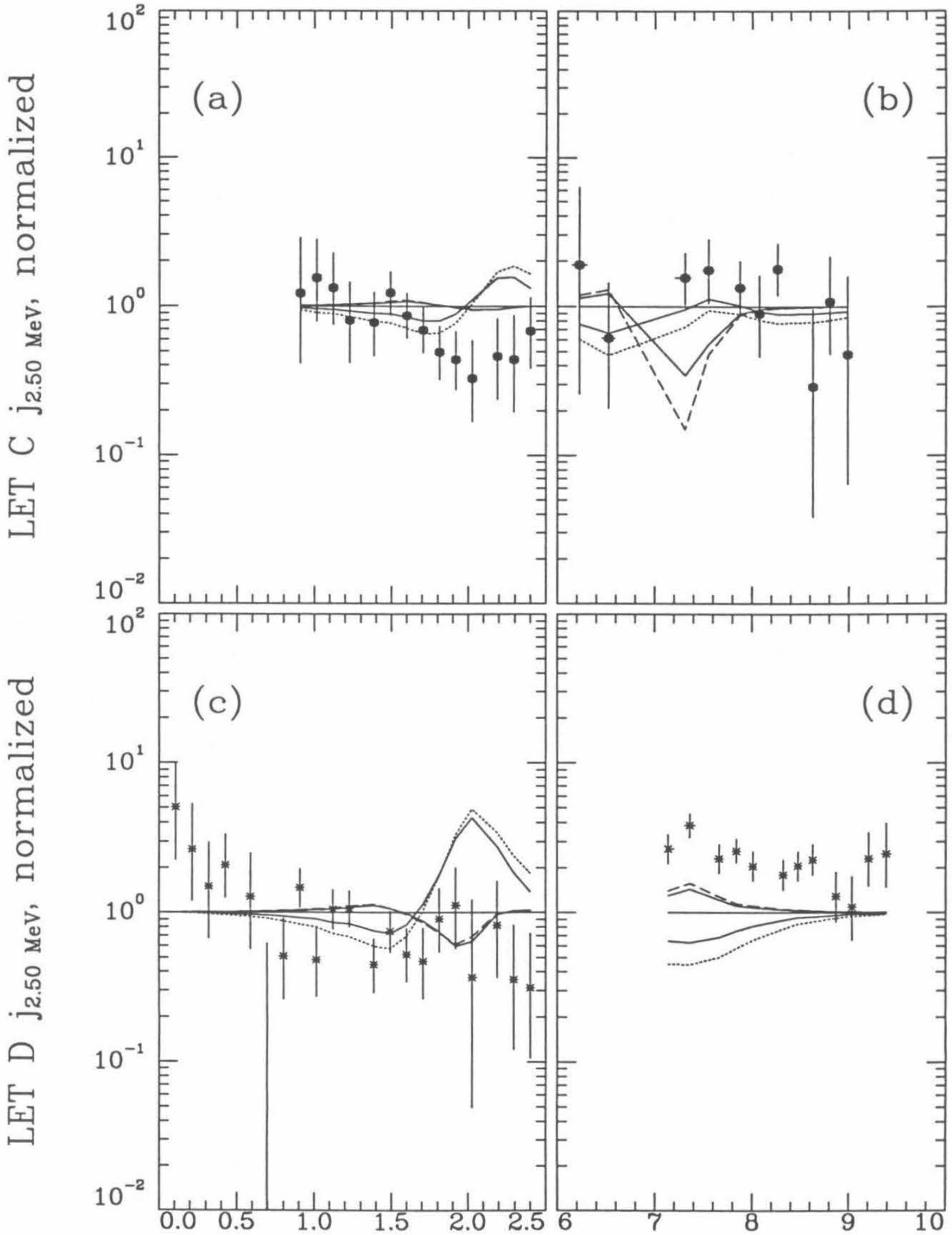
LET C $j_{2.50\ \mathrm{MeV}}$, normalized
LET D $j_{2.50\ \mathrm{MeV}}$, normalized
(a)
(b)
(c)
(d)
10^2
10^1
10^0
10^{-1}
10^{-2}
0.0 0.0 0.5 1.0 1.5 2.0 2.5
6 7 8 9 10
Hr. of day 237 (in)
I8E1 L (out)

too little pitch-angle diffusion results in very different pitch-angle distributions and also in different amounts of loss at all pitch angles due to more- or less-efficient coupling to higher pitch angles where satellite absorption takes place. By the criterion above, the normalization of D_{xx} is, like that of D_{LL}, correct within about a factor of 3. The other two parameters, however, have effects in the model on all the observed regions, and in a coupled manner: a larger (or smaller) ΔL at fixed L_0 has an effect similar to a higher (or lower) L_0 in extending (or diminishing) the region where pitch-angle diffusion is effective. If it begins too far in, the resulting model retains the extreme pitch-angle anisotropy of the radial-diffusion-only model inward past the roll maneuver, resulting in a jump in the simulated LET C outbound fluxes there, while if it begins too far out the form of the pitch-angle distribution sampled by the later inbound observations is smoothed too much, as in the model of figures 5.8 and 5.9. Thus, despite the rather suspicious proximity in L of the onset of pitch-angle diffusion and the roll maneuver, it appears that the observations do in fact constrain the location and abruptness of that onset to be close to those in the model of §5.2. L_0 is probably correct to within about ± 0.4 units in L; since the range of ΔL consistent with the observations according to our criterion is smaller than or comparable to this uncertainty, it is not possible to separate it from L_0, and all we can say is that the turn-on of pitch-angle diffusion is abrupt on the scale of the uncertainty in L_0.

Appendix 4

Limitations of the Pitch-Angle Eigenfunction Method

To solve equation 5.9 exactly by means of the eigenfunction method of equation 5.16 would involve an infinite number of terms in the series of equation 5.15, even ignoring the approximations leading to equation 5.10; the choice made in this work was to truncate the series after the twentieth term. To see what the consequences of this are, first we look at the degree to which a 20-term series can approximate an arbitrary pitch-angle distribution. Figures A4.1 show partial sums up to twenty terms of the series for a $\sin^{2n}\theta = (1 - x^2)^n$ pitch angle distribution, as was assumed at the boundary at $L = 10$, for n from 0 to 4 and for $x = 0.90$ and $x = 0.97$; this latter is as high as we need in order to simulate our observations. Two trends immediately apparent are that more terms are needed for accuracy at a higher x, and that more are usually needed for a more anisotropic pitch-angle distribution. Twenty terms seems to be good enough for these ns and x; we note in figure 5.4(a) that the pitch-angle distribution becomes much more anisotropic than in this figure at low Ls, but by introducing pitch-angle diffusion we are expecting to reduce this anisotropy in order to reproduce better the observations at the spacecraft roll, so the models for which this method is intended should not be so extreme. That this method *is* insufficient for the anisotropies of the radial-diffusion model is apparent in figures A4.2, where equation 5.16 is solved for D_{LL} as in that model and for $\lambda_i \equiv 0$: the phase-space density is no longer even positive definite in the solution. Nonetheless, where the anisotropy is not too extreme the solution is at least qualitatively similar to those of figures 5.4 and 5.5; the apparent smoothing of the phase-space density contours in figure A4.2(b) where those of figures 5.4(b) and 5.5(b) break sharply can be attributed to the loss of "high-frequency" terms due to the truncation of the series of equation 5.15.

Figures A4.3 show a further approximation implicit in our solutions of equation 5.16. τ_{ij}^{-1} as defined in equation 5.17 is an integral, which was done numerically at a grid spacing

Figure A4.1

Partial sums of the series implied by equation 5.19, which should approach $\sin^{2n}\theta \equiv (1 - x^2)^n$ at each x. $x = 0.90$ in figure A4.1(a), and $x = 0.97$ in figure A4.1(b); curves are partial sums of the series

$$\sum_{i=1}^{\infty} a_i g_i(x)$$

for $n = 0$ to $n = 4$ (from top to bottom) in steps of ½ and points at right margin are exact values.

Figure A4.1

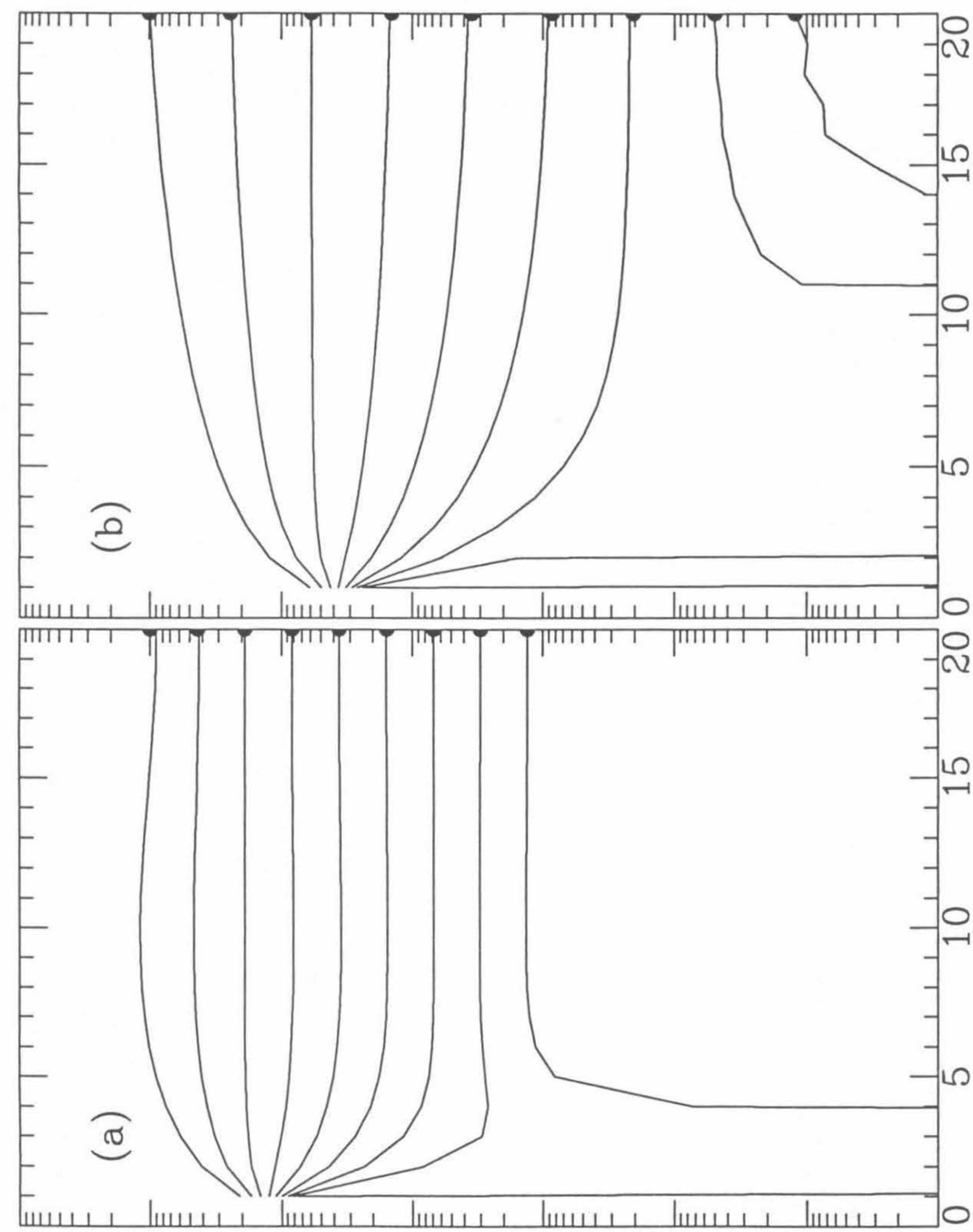
(a)
(b)
number of $g_i(x)$'s
number of $g_i(x)$'s
0
5
10
15
20
10^1
10^0
10^{-1}
10^{-2}
10^{-3}
10^{-4}
10^{-5}
10^{-6}
partial sums of $\sin^{2n}\theta$, n = 0 to 4 by 0.5's

Figure A4.2

Proton phase-space densities plotted as in figures 5.6 and 5.8 for the model (with radial diffusion only) of figures 5.3, 5.4, and 5.5, but calculated using equation 5.16 (with $\lambda_i \equiv 0$). Figure A4.2(a) presents traces at $\zeta = 10^4$ MeV/G and the same xs as before; figure A4.2(b) presents a contour plot, but with curves only from $\log_{10} f = -12$ to -14 by steps of ½ (in units of $(\mathrm{cmMeV/c})^{-3}$) from upper right to lower left, since as seen in figure A4.2(a) the model produces garbage below the lowest of these levels.

Figure A4.2

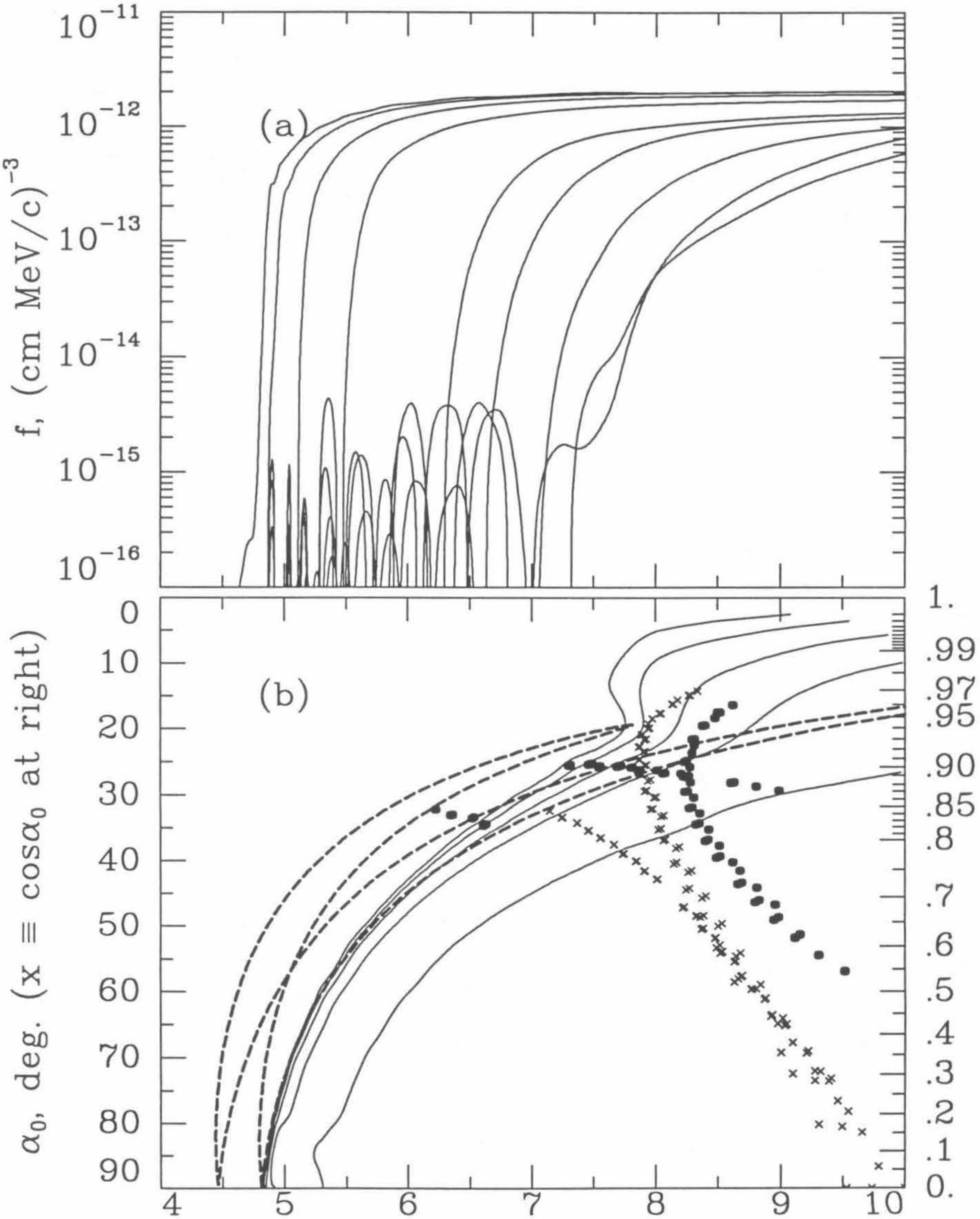
(a)
f, (cm MeV/c)$^{-3}$
10^{-11}
10^{-12}
10^{-13}
10^{-14}
10^{-15}
10^{-16}
(b)
α_0, deg. (x ≡ cosα_0 at right)
0
10
20
30
40
50
60
70
80
90
1.
.99
.97
.95
.90
.85
.8
.7
.6
.5
.4
.3
.2
.1
0.
4
5
6
7
8
9
10
L (ζ = 10^4 MeV/G)

Figure A4.3

Inverse absorption lifetime matrix elements τ_{ij}^{-1}; lighter, more jagged line is as calculated, heavier line is smoothed as described in the text. τ_{88}^{-1} is the nonnegative-definite pair of curves, τ_{48}^{-1} is the other. Figure A4.3(a) is plotted on a linear scale, and figure A4.3(b) is plotted on a logarithmic scale; $\zeta = 10^4$ MeV/G for both.

Figure A4.3

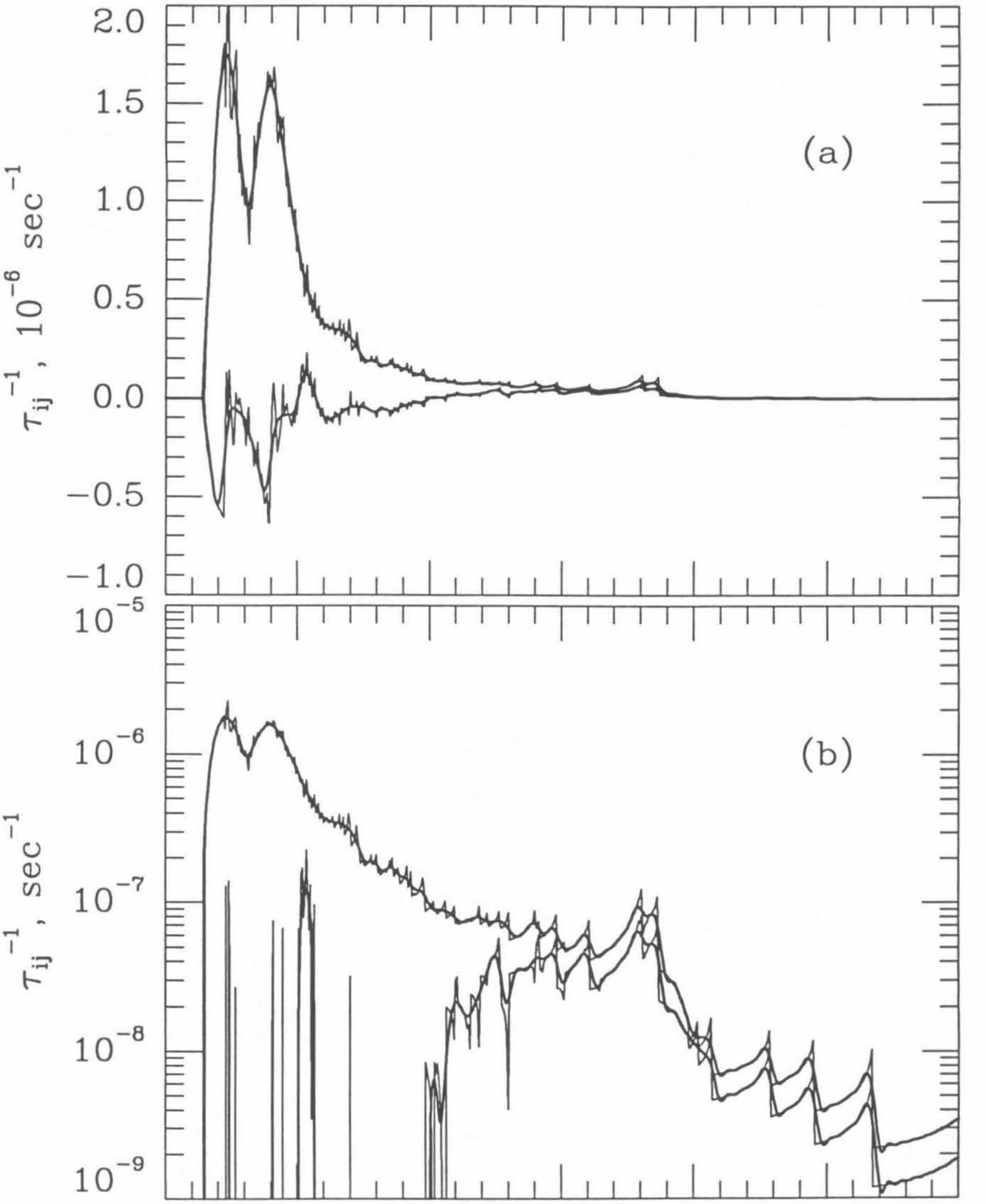
2.0
1.5
1.0
0.5
0.0
−0.5
−1.0
(a)
τ_{ij}^{-1}, 10^{-6} sec^{-1}
10^{-5}
10^{-6}
10^{-7}
10^{-8}
10^{-9}
(b)
τ_{ij}^{-1}, sec^{-1}
4
5
6
7
8
9
10
L (ζ = 10^4 MeV/G)

of 0.02 in x; the results of this calculation for $\zeta = 10^4$ MeV/G, $j = 8$, and $i = 4$ and 8 are shown as the jagged lines in these figures. The jaggedness is caused by the sharp cutoffs in $\tau_{ss}^{-1}(x)$ at the high-L end of each leg of the moon's trajectory, when it passes above the mirror latitude of the particles in question. These cutoffs are closely-enough spaced in L for the lower xs that it was felt safe to approximate the (smooth) integral by applying a low-pass fast Fourier transform filter (SMOOFT, from Press *et al.* (1988)) with a cutoff at a wavelength of 0.2 units of L, as shown in these figures by the heavy smooth curve. (The algorithm used to solve the differential equation had had some difficulty with sharply and rapidly varying components of the equation, so it was thought necessary to smooth τ_{ij}^{-1}.) At higher xs, however, the endpoints of absorption become farther apart in L, and smoothing is not likely to give a much better approximation to the actual integral; for example, the spikes at $L \approx 8.1$ and 8.6 in figure A4.3(b) are due to the the cutoffs on two legs of the moon's trajectory for $x = 0.92$, and those at $L \approx 8.9$ and 9.3 are due to cutoffs for $x = 0.94$, and they are not cleaned up very much by the FFT smoothing. However, the phase-space density profiles in this region of L are pretty flat for the models considered, and the absolute value of the inverse lifetime τ_{ij}^{-1} is much reduced, so it should make little difference to the models calculated.

A test of this is shown in figures A4.4 and A4.5, where τ_{ss}^{-1} is regenerated from τ_{ij}^{-1} for $\zeta = 10^4$ MeV/G and three different xs; figure A4.4 is from the set represented by the jagged lines in figures A4.3, while figure A4.5 is from the smoothed. The heavy solid line in these figures is τ_{ss}^{-1} as calculated directly; the lighter lines are regenerated as follows: let b_j be the set of coefficients that reproduce a function that is identically unity for x from 0 to 1, *i.e.*, for all x

$$1 \equiv \sum_j b_j g_j(x), \tag{A4.1}$$

which by the orthonormalization shown in equation 5.12 implies that

$$b_j = \int_0^1 x\, dx\, g_j(x). \tag{A4.2}$$

Then we seek the set of coefficients a_i such that

Figure A4.4

Inverse lifetimes τ_{ss}^{-1} for $\zeta = 10^4$ MeV/G, and (a) $x = 0.20$, (b) $x = 0.60$, and (c) $x = 0.95$. Heavy solid line is calculated directly as in chapter 4; lighter line is regenerated from the matrix of τ_{ij}^{-1} as in equations A4.4, with dotted segments being negative (logarithm of $-\tau_{ss}^{-1}$ is plotted). τ_{ij}^{-1} here is as originally calculated, and shown in figures A4.3 as the lighter jagged lines.

Figure A4.5

Inverse lifetimes τ_{ss}^{-1} as in figures A4.4, but with regenerated τ_{ss}^{-1} calculated from the smoothed version of τ_{ij}^{-1} shown in figures A4.3 as heavy smooth lines.

Figure A4.4

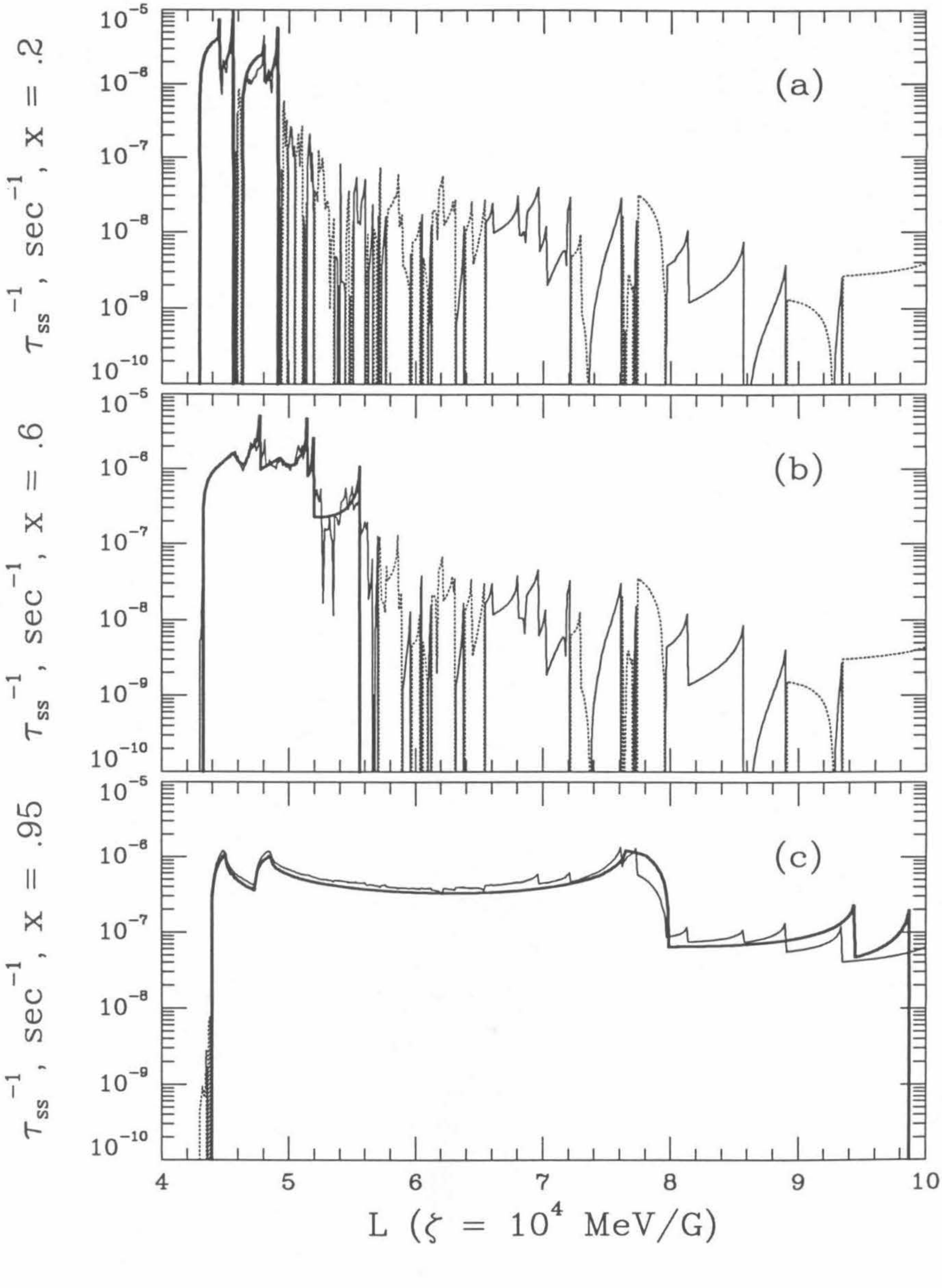
(a)
(b)
(c)
τ_{ss}^{-1} , sec^{-1} , X = .2
τ_{ss}^{-1} , sec^{-1} , X = .6
τ_{ss}^{-1} , sec^{-1} , X = .95
10^{-5}
10^{-6}
10^{-7}
10^{-8}
10^{-9}
10^{-10}
4
5
6
7
8
9
10
L (ζ = 10^4 MeV/G)

Figure A4.5

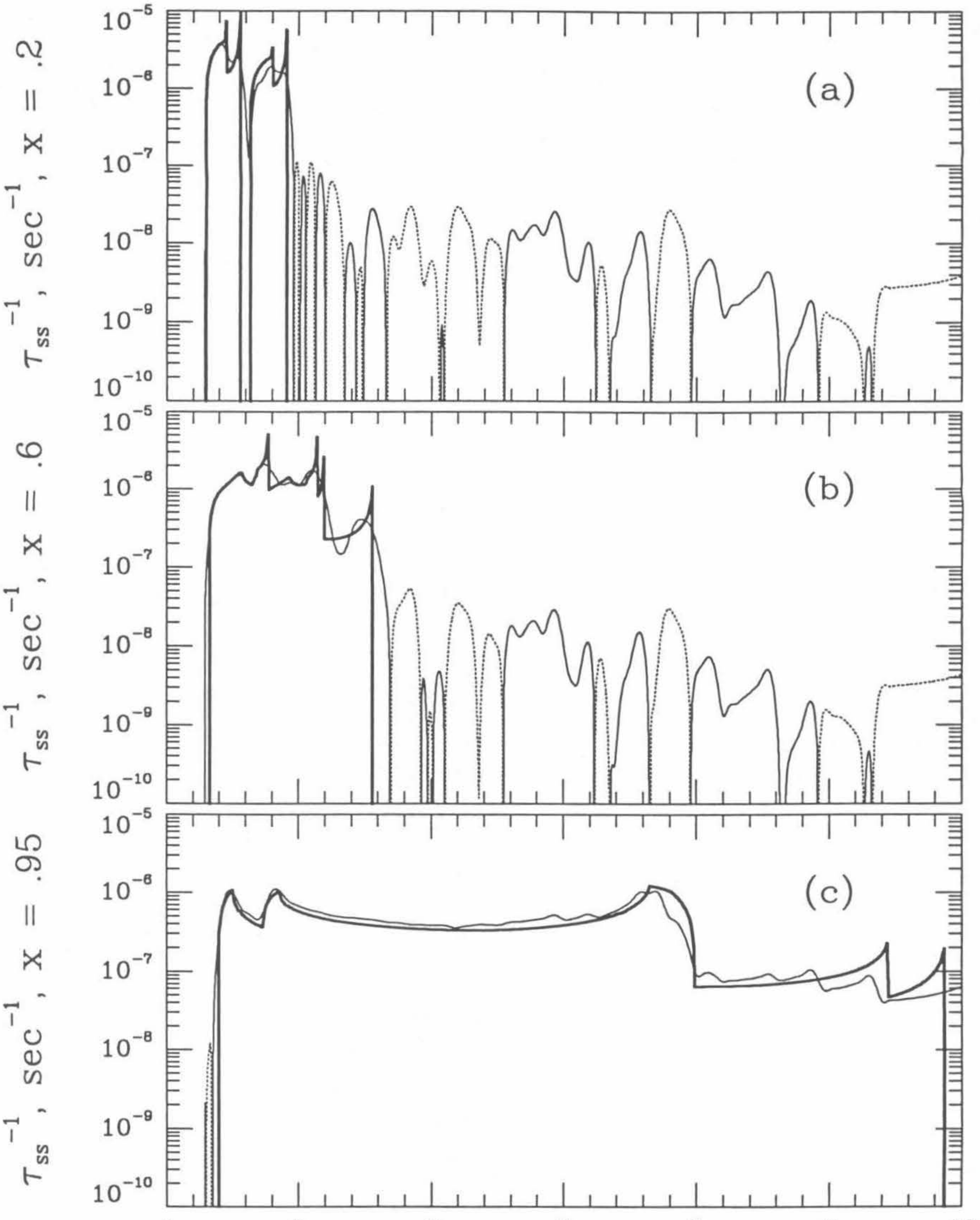
10^{-5}
10^{-6}
10^{-7}
10^{-8}
10^{-9}
10^{-10}
τ_{ss}^{-1}, sec^{-1}, X = .2
(a)
τ_{ss}^{-1}, sec^{-1}, X = .6
(b)
τ_{ss}^{-1}, sec^{-1}, X = .95
(c)
4
5
6
7
8
9
10
L (ζ = 10^4 MeV/G)

$$\tau_{ss}^{-1}(x) = \sum_i a_i g_i(x). \tag{A4.3}$$

Using the definition in equation 5.17,

$$\sum_j b_j \tau_{ij}^{-1} = \sum_j b_j \int_0^1 x \, dx \, g_i(x) g_j(x) \tau_{ss}^{-1}(x); \tag{A4.4(a)}$$

using equation A4.3,

$$\sum_j b_j \tau_{ij}^{-1} = \sum_j b_j \int_0^1 x \, dx \, g_i(x) g_j(x) \sum_k a_k g_k(x); \tag{A4.4(b)}$$

rearranging integrations and summations,

$$\sum_j b_j \tau_{ij}^{-1} = \sum_k a_k \int_0^1 x \, dx \, g_i(x) g_k(x) \sum_j b_j g_j(x); \tag{A4.4(c)}$$

using equation A4.1,

$$\sum_j b_j \tau_{ij}^{-1} = \sum_k a_k \int_0^1 x \, dx \, g_i(x) g_k(x); \tag{A4.4(d)}$$

and using equation 5.12,

$$\sum_j b_j \tau_{ij}^{-1} = \sum_k a_k \delta_{ik} = a_i, \tag{A4.4(e)}$$

so we can put this into equation A4.3 and recover $\tau_{ss}^{-1}(x)$ from τ_{ij}^{-1}. Overall magnitudes are about right for the regenerated τ_{ss}^{-1}s, and the absolute value drops by at least an order of magnitude where each directly-calculated τ_{ss}^{-1} vanishes, sometimes going negative (dotted lines); the details of the peaks and valleys of the direct τ_{ss}^{-1}s are reproduced at a resolution comparable to that of the matrix τ_{ij}^{-1}. It could be expected, then, that the calculated model for the eigenvalue method would resemble that of a direct solution with correct τ_{ss}^{-1}s at about this same level.

Figures A4.6, A4.7, and A4.8 show a comparison for the same ζ and xs as in figures A4.4 and A4.5 of the different contributions to equation 5.9; we may rewrite that equation as

$$\sum_i g_i(x) L^{\frac{5}{2}} \frac{\partial}{\partial L}\left[L^{-\frac{5}{2}} D_{LL} \frac{\partial a_i}{\partial L}\right] - \sum_j a_j(L)\lambda_j g_j(x) - \tau_{ss}^{-1} \sum_k a_k(L) g_k(x) = 0 \tag{A4.5}$$

at each ζ, x, and L. Dividing by $-f$ as calculated from equation 5.15 using a_i from a model solution, we may express this equation as a sum of inverse lifetimes, each corresponding to one term of the equation; if we use the directly-calculated value of τ_{ss}^{-1} for the third term, the left-hand side of this equation will not necessarily add up to zero, so we express the right-hand side error as an inverse lifetime τ_{err}^{-1} as well: for

$$\tau_L^{-1} = -\frac{1}{f}\sum_i g_i(x) L^{\frac{5}{2}} \frac{\partial}{\partial L}\left[L^{-\frac{5}{2}} D_{LL} \frac{\partial a_i(L)}{\partial L}\right] \tag{A4.6(a)}$$

and

$$\tau_{pa}^{-1} = \frac{1}{f}\sum_j a_j(L)\lambda_j g_j(x), \tag{A4.6(b)}$$

we have

$$\tau_L^{-1} + \tau_{pa}^{-1} + \tau_{ss}^{-1} = \tau_{err}^{-1}. \tag{A4.7}$$

τ_L^{-1} and τ_{pa}^{-1} are positive when there are net losses of particles to other Ls and pitch angles, respectively, and negative when there is a net influx; τ_{ss}^{-1} is always nonnegative. Figures A4.6, A4.7, and A4.8 begin at $L = 5$ because inward from there f is reduced enough that dividing by it produces numerical errors. Looking at these figures in turn, which are calculated for the nominal combined-diffusion model of figures 5.6 and 5.7, we note that the behavior is qualitatively as expected: at low x there is a net loss to higher xs via pitch-angle diffusion (where it is in operation), which must be made up through inflow from other Ls; at a higher x where satellite absorption extends to $L \approx 5.6$, there is inflow both from other Ls and from other xs to make up loss to the satellite, and outside there the situation is as for the lower x; and for the highest x, where satellite absorption is present throughout the range of L, the inflow via both diffusion mechanisms is present almost everywhere. In all three cases the error is typically an order of magnitude or more down from the dominant contribution to the left-hand side of equation A4.7, though this gets worse as x increases. Thus we can expect that the errors in the phase-space densities calculated using the eigenfunction method will be down a comparable amount relative to the calculated values; certainly, as seen from figures 5.7, the systematic errors resulting from a too-simple model will be larger than these.

Figure A4.6

Inverse-lifetime representations of the components of equation 5.9 as in equation A4.7, for $\zeta = 10^4$ MeV/G and $x = 0.20$, and the model of figures 5.6 and 5.7: (a) pitch-angle diffusion, (b) radial diffusion, and (c) error.

Figure A4.7

Inverse-lifetime representations of the components of equation 5.9 as in figure A4.6, for $\zeta = 10^4$ MeV/G and $x = 0.60$.

Figure A4.8

Inverse-lifetime representations of the components of equation 5.9 as in figure A4.6, for $\zeta = 10^4$ MeV/G and $x = 0.95$.

Figure A4.6

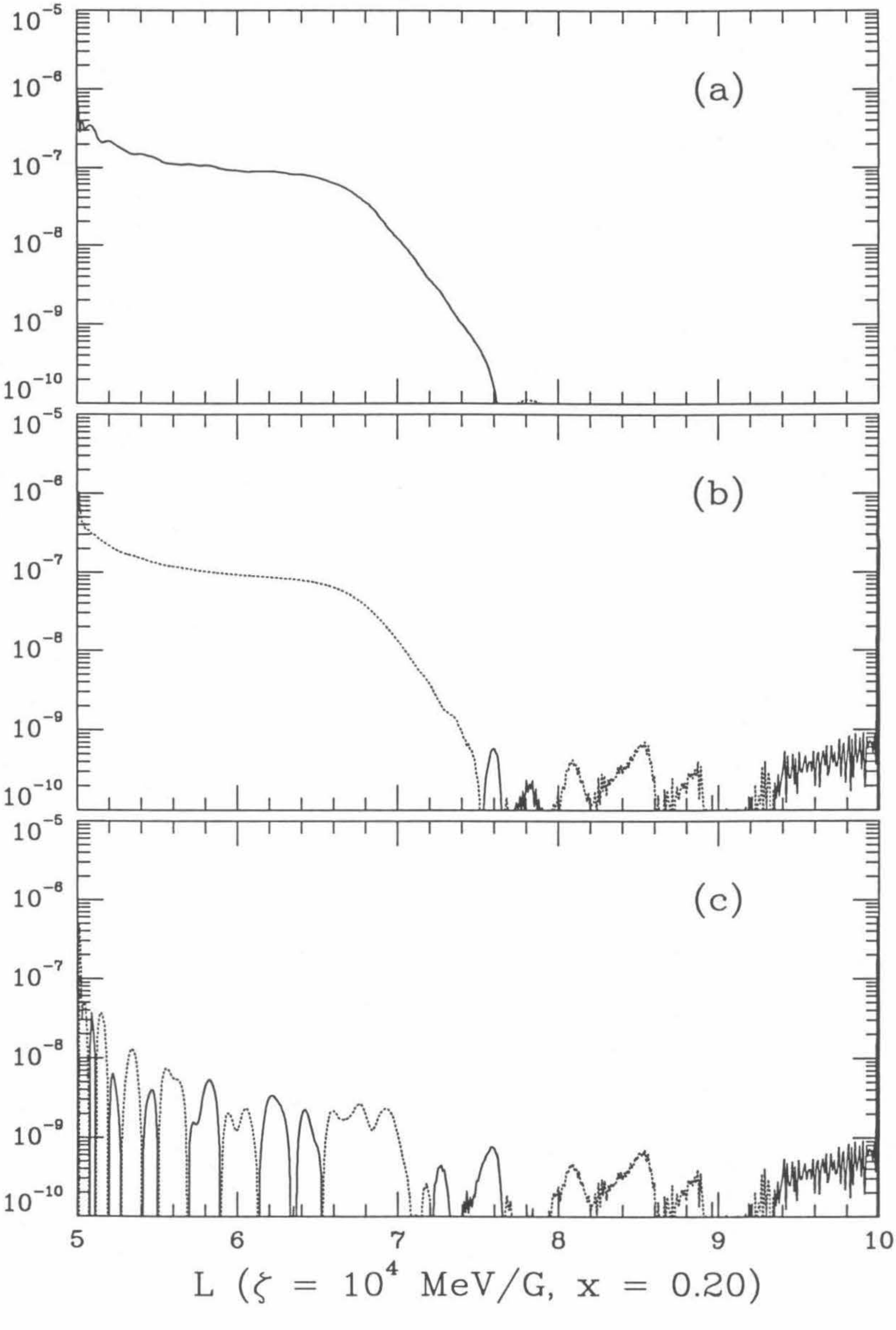
10^{-5}
10^{-6}
10^{-7}
10^{-8}
10^{-9}
10^{-10}
τ_{pa}^{-1} , sec^{-1}
(a)
τ_{L}^{-1} , sec^{-1}
(b)
τ_{err}^{-1} , sec^{-1}
(c)
5
6
7
8
9
10
L (ζ = 10^4 MeV/G, x = 0.20)

Figure A4.7

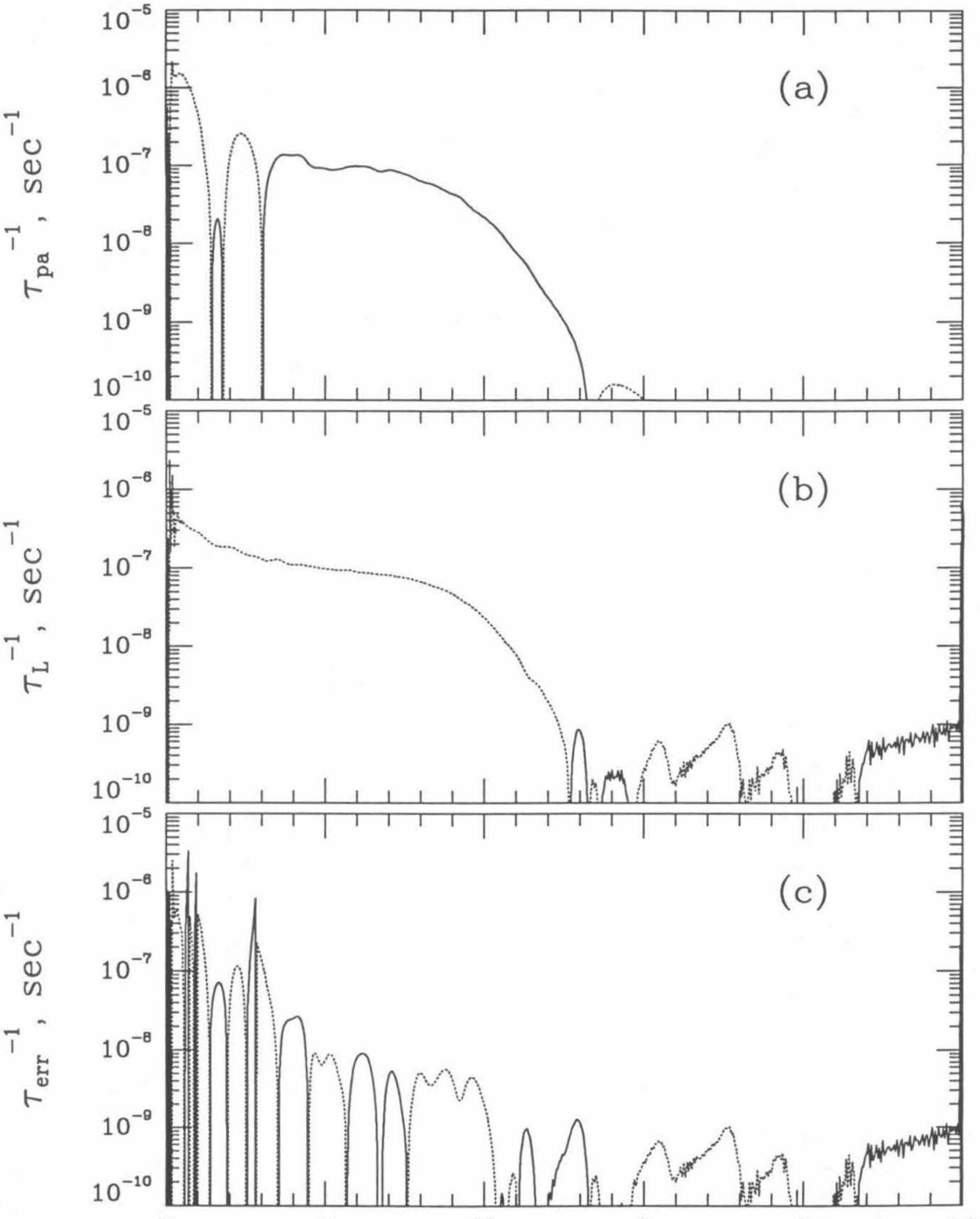
(a)
(b)
(c)
τ_{pa}^{-1} , sec^{-1}
τ_{L}^{-1} , sec^{-1}
τ_{err}^{-1} , sec^{-1}
10^{-5}
10^{-6}
10^{-7}
10^{-8}
10^{-9}
10^{-10}
5
6
7
8
9
10
L (ζ = 10^4 MeV/G, x = 0.60)

Figure A4.8

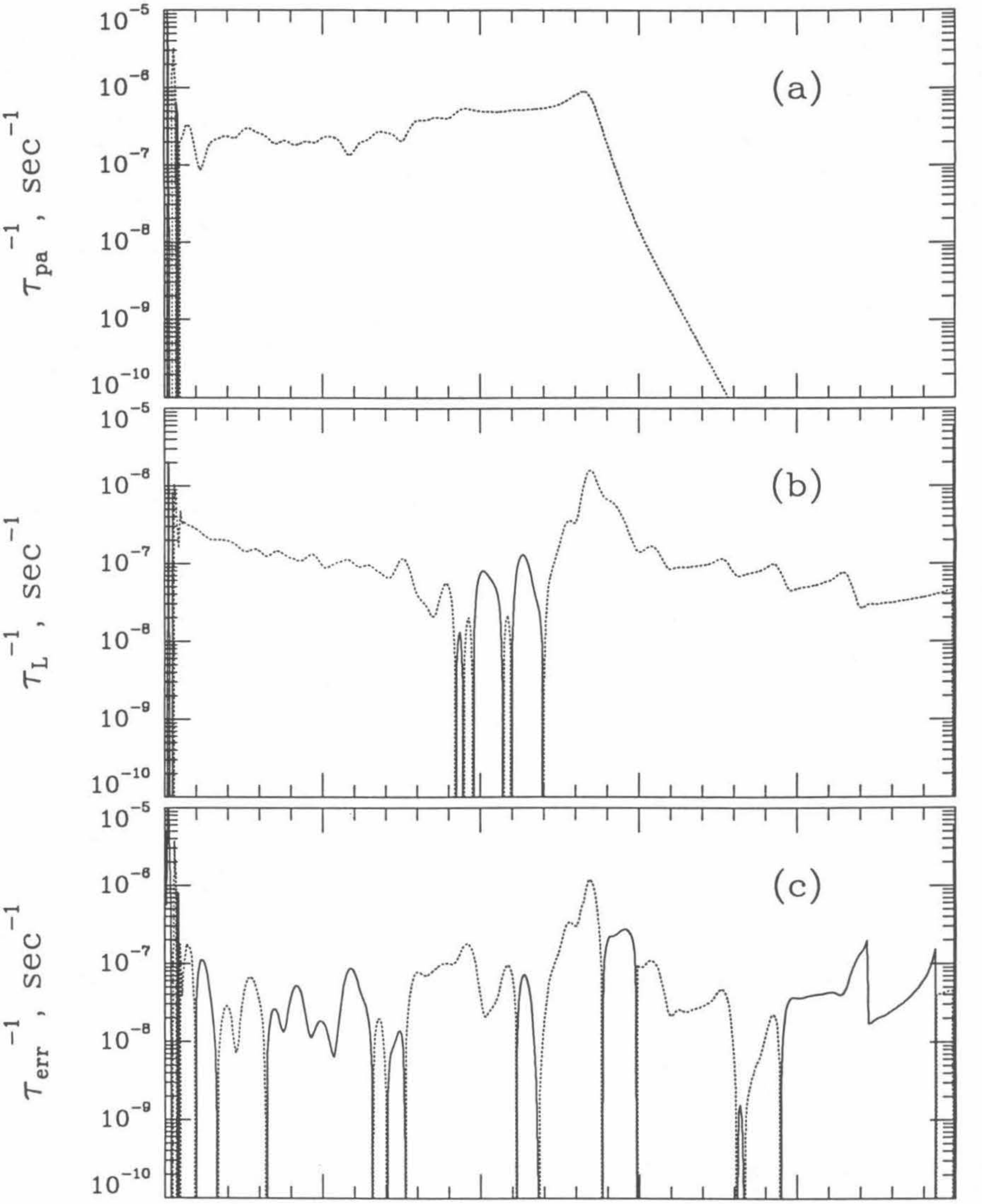
(a)
(b)
(c)
τ_{pa}^{-1} , sec^{-1}
τ_{L}^{-1} , sec^{-1}
τ_{err}^{-1} , sec^{-1}
10^{-5}
10^{-6}
10^{-7}
10^{-8}
10^{-9}
10^{-10}
5
6
7
8
9
10
L (ζ = 10^4 MeV/G, x = 0.95)

References

Abramowitz, M., and I. A. Stegun, *Handbook of Mathematical Functions* (National Bureau of Standards: Washington, D.C., 1964)

Armstrong, T. P., M. T. Paonessa, E. V. Bell II, and S. M. Krimigis, *Journal of Geophysical Research*, **88**, 8893 (1983)

Baker, S., and R. D. Cousins, *Nuclear Instruments and Methods in Physics Research*, **221**, 437 (1984)

Bevington, P. R., *Data Reduction and Error Analysis for the Physical Sciences* (McGraw-Hill: New York, NY, 1969)

Brice, N., and T. R. McDonough, *Icarus*, **18**, 206 (1973)

Bridge, H. S., J. W. Belcher, A. J. Lazarus, J. D. Sullivan, R. L. McNutt, F. Bagenal, J. D. Scudder, E. C. Sittler, G. L. Siscoe, V. M. Vasyliunas, C. K. Goertz, and C. M. Yeates, *Science*, **204**, 987 (1979)

Bridge, H. S., J. W. Belcher, A. J. Lazarus, S. Olbert, J. D. Sullivan, F. Bagenal, P. R. Gazis, R. E. Hartle, K. W. Ogilvie, J. D. Scudder, E. C. Sittler, A. Eviatar, G. L. Siscoe, C. K. Goertz, and V. M. Vasyliunas, *Science*, **212**, 217 (1981)

Broadfoot, A. L., M. J. S. Belton, P. Z. Takacs, B. R. Sandel, D. E. Shemansky, J. B. Holberg, J. M. Ajello, S. K. Atreya, T. M. Donahue, H. W. Moos, J. L. Bertaux, J. E. Blamont, D. F. Strobel, J. C. McConnell, A. Dalgarno, R. Goody, and M. B. McElroy, *Science*, **204**, 979 (1979)

Broadfoot, A. L., B. R. Sandel, D. E. Shemansky, J. B. Holberg, G. R. Smith, D. F. Strobel, J. C. McConnell, S. Kumar, D. M. Hunten, S. K. Atreya, T. M. Donahue, H. W. Moos, J. L. Bertaux, J. E. Blamont, R. B. Pomphrey, and S. Linick, *Science*, **212**, 206 (1981)

Chenette, D. L., and E. C. Stone, *Journal of Geophysical Research*, **88**, 8755 (1983)

Cheng, A. F., C. G. Maclennan, B. H. Mauk, S. M. Krimigis, and L. J. Lanzerotti, *Icarus*, **99**, 420 (1992)

Connerney, J. E. P., M. H. Acuna, and N. F. Ness, *Journal of Geophysical Research*, **96**, Supplement, 19023 (1991)

Cook, W. R., Ph.D. Thesis, California Institute of Technology (1981)

Cooper, J. F., *Geophysical Research Letters*, **17**, 1665 (1990)

Cuzzi, J. N., and J. A. Burns, *Icarus*, **74**, 284 (1988)

Dearnaley, G., and D. C. Northrop, *Semiconductor Counters for Nuclear Radiations*, second edition (E. & F. N. Spon: London, 1966)

Fälthammar, C.-G., in *Earth's Particles and Fields*, ed. B. M. McCormack, p. 157 (Reinhold: New York, NY, 1968)

Fillius, W., W.-H. Ip, and C. E. McIlwain, *Science*, **207**, 425 (1980)

Gehrels, N., *Space Radiation Laboratory Internal Report #80* (1981)

Gehrels, N., *Astrophysical Journal*, **303**, 336 (1986)

Goldstein, H., *Classical Mechanics* (Addison-Wesley: Reading, MA, 1950)

Gurnett, D. A., W. S. Kurth, R. L. Poynter, L. J. Granroth, I. H. Cairns, W. M. Macek, S. L. Moses, F. V. Coroniti, C. F. Kennel, and D. D. Barbosa, *Science*, **246**, 1494 (1989)

Haerendel, G., in *Earth's Particles and Fields*, ed. B. M. McCormack, p. 171 (Reinhold: New York, NY, 1968)

Hood, L. L., *Journal of Geophysical Research*, **88**, 808 (1983)

Hood, L. L., *Journal of Geophysical Research*, **94**, 15077 (1989)

Kennel, C. F., and H. E. Petschek, *Journal of Geophysical Research*, **71**, 1 (1966)

Krimigis, S. M., T. P. Armstrong, W. I. Axford, C. O. Bostrom, C. Y. Fan, G. Gloeckler, L. J. Lanzerotti, E. P. Keath, R. D. Zwickl, J. F. Carbary, and D. C. Hamilton, *Science*, **204**, 998 (1979)

Krimigis, S. M., J. F. Carbary, E. P. Keath, C. O. Bostrom, W. I. Axford, G. Gloeckler, L. J. Lanzerotti, and T. P. Armstrong, *Journal of Geophysical Research*, **86**, 8227 (1981)

Krimigis, S. M., J. F. Carbary, E. P. Keath, T. P. Armstrong, L. J. Lanzerotti, and G. Gloeckler, *Journal of Geophysical Research*, **88**, 8871 (1983)

Krimigis, S. M., T. P. Armstrong, W. I. Axford, A. F. Cheng, G. Gloeckler, D. C. Hamilton, E. P. Keath, L. J. Lanzerotti, and B. H. Mauk, *Science*, **233**, 97 (1986)

Krimigis, S. M., T. P. Armstrong, W. I. Axford, C. O. Bostrom, A. F. Cheng, G. Gloeckler, D. C. Hamilton, E. P. Keath, L. J. Lanzerotti, B. H. Mauk, and J. A. Van Allen, *Science*, **246**, 1483 (1989)

Krimigis, S. M., B. H. Mauk, A. F. Cheng, E. P. Keath, M. Kane, T. P. Armstrong, G. Gloeckler, and L. J. Lanzerotti, *Geophysical Research Letters*, **17**, 1685 (1990)

Lanzerotti, L. J., and S. M. Krimigis, *Physics Today*, November 1985, p. 24 (1985)

Lupton, J. E., and E. C. Stone, *Nuclear Instruments and Methods*, **98**, 189 (1972)

Mauk, B. H., E. P. Keath, M. Kane, S. M. Krimigis, A. F. Cheng, M. H. Acuna, T. P. Armstrong, and N. F. Ness, *Journal of Geophysical Research*, **96**, Supplement, 19061 (1991)

McIlwain, C. E., *Journal of Geophysical Research*, **66**, 3681 (1961)

McIlwain, C. E., *Space Science Reviews*, **5**, 585 (1966)

Ness, N. F., private communication (1990)

Ness, N. F., M. H. Acuna, K. W. Behannon, L. F. Burlaga, J. E. P. Connerney, R. P. Lepping, and F. M Neubauer, *Science*, **233**, 85 (1986)

Ness, N. F., M. H. Acuna, L. F. Burlaga, J. E. P. Connerney, R. P. Lepping, and F. M Neubauer, *Science*, **246**, 1473 (1989)

Paonessa, M., and A. F. Cheng, *Journal of Geophysical Research*, **90**, 3428 (1985)

Paonessa, M., and A. F. Cheng, *Journal of Geophysical Research*, **92**, 1160 (1987)

Paranicas, C. P., and A. F. Cheng, *Journal of Geophysical Research*, **96**, Supplement, 19123 (1991)

Press, W. H., B. P. Flannery, S. A. Teukolsky, and W. T. Vetterling, *Numerical Recipes in C* (Cambridge University Press: Cambridge, 1988)

Richardson, J. D., J. W. Belcher, M. Zhang, and R. L. McNutt, Jr., *Journal of Geophysical Research*, **96**, Supplement, 18,993 (1991)

Roederer, J. G., *Dynamics of Geomagnetically Trapped Radiation* (Springer: New York, NY, 1970)

Rossi, B., and S. Olbert, *Introduction to the Physics of Space* (McGraw-Hill: New York, NY, 1970)

Sandel, B. R., D. E. Shemansky, A. L. Broadfoot, J. B. Holberg, G. R. Smith, J. C. McConnell, D. F. Strobel, S. K. Atreya, T. M. Donahue, H. W. Moos, D. M. Hunten, R. B. Pomphrey, and S. Linick, *Science*, **215**, 548 (1982)

Schardt, A. W., and F. B. McDonald, *Journal of Geophysical Research*, **88**, 8923 (1983)

Schulz, M., and G. T. Davidson, *Journal of Geophysical Research*, **93**, 59 (1988)

Schulz, M., and L. J. Lanzerotti, *Particle Diffusion in the Radiation Belts* (Springer: New York, NY, 1974)

Selesnick, R. S., private communication (1990)

Selesnick, R. S., private communication (1991)

Selesnick, R. S., *Journal of Geophysical Research*, **97**, 10857 (1992a)

Selesnick, R. S., poster P1.15 at the Ninth Magnetospheres of the Outer Planets Symposium (1992b)

Selesnick, R. S., and E. C. Stone, *Journal of Geophysical Research*, **96**, 5651 (1991a)

Selesnick, R. S., and E. C. Stone, *Journal of Geophysical Research*, **96**, Supplement, 19137 (1991b)

Simpson, J. A., T. S. Bastian, D. L. Chenette, G. A. Lentz, R. B. McKibben, K. R. Pyle, and A. J. Tuzzolino, *Science*, **207**, 411 (1980)

Siscoe, G. L., and D. Summers, *Journal of Geophysical Research*, **86**, 8471 (1981)

Stilwell, D. E., W. D. Davis, R. M. Joyce, F. B. McDonald, J. H. Trainor, W. E. Althouse, A. C. Cummings, T. L. Garrard, E. C. Stone, and R. E. Vogt, *IEEE Transactions on Nuclear Science*, **NS-26**, 513 (1979)

Stone, E. C., *Journal of Geophysical Research*, **68**, 4157 (1963)

Stone, E. C., J. F. Cooper, A. C. Cummings, F. B. McDonald, J. H. Trainor, N. Lal, R. McGuire, and D. L. Chenette, *Science*, **233**, 93 (1986)

Stone, E. C., and E. D. Miner, *Science*, **246**, 1417 (1989)

Stone, E. C., R. E. Vogt, F. B. McDonald, B. J. Teegarden, J. H. Trainor, J. R. Jokipii, and W. R. Webber, *Space Science Reviews*, **21**, 355 (1977)

Sullivan, J. D., *Nuclear Instruments and Methods*, **95**, 5 (1971)

Thorne, R. M., in *Physics of the Jovian Magnetosphere*, ed. A. J. Dessler, p. 454 (Cambridge University Press: NY, 1983)

Van Allen, J. A., M. F. Thomsen, B. A. Randall, R. L. Rairden, and C. L. Grosskreutz, *Science*, **207**, 415 (1980)

Vogt, R. E., W. R. Cook, A. C. Cummings, T. L. Garrard, N. Gehrels, E. C. Stone, J. H. Trainor, A. W. Schardt, T. Conlon, N. Lal, and F. B. McDonald, *Science*, **204**, 1003 (1979)

Vogt, R. E., D. L. Chenette, A. C. Cummings, T. L. Garrard, E. C. Stone, A. W. Schardt, J. H. Trainor, N. Lal, and F. B. McDonald, *Science*, **212**, 231 (1981)

Walt, M., in *Particles and Fields in the Magnetosphere*, ed. B. M. McCormack, p. 410 (D. Reidel: Dordrecht, Holland, 1970)